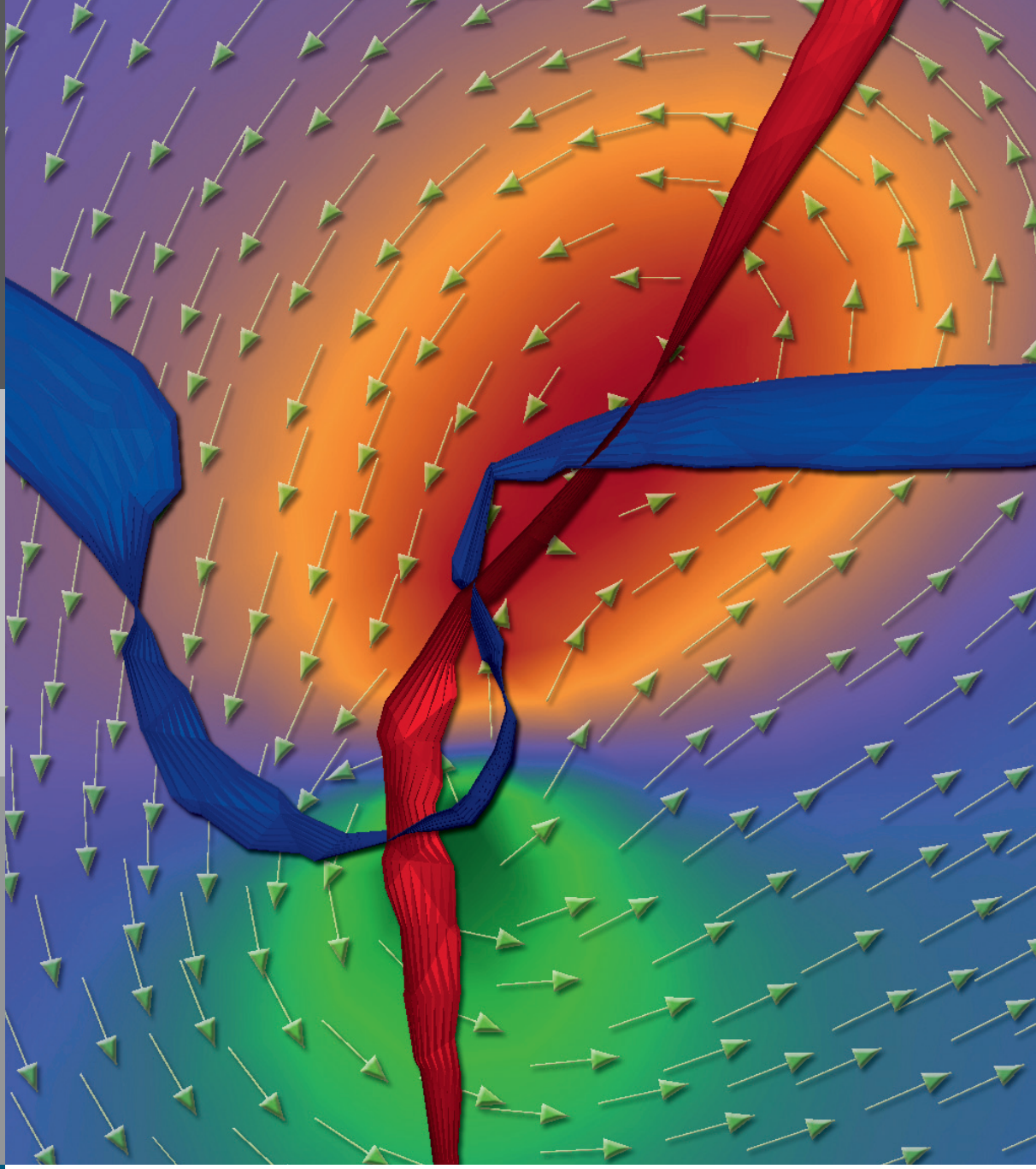

# Ultrafast vortex core dynamics investigated by finite-element micromagnetic simulations

Sebastian Gliga

Mitglied der Helmholtz-Gemeinschaft

JÜLICH
FORSCHUNGSZENTRUM

Schriften des Forschungszentrums Jülich
Reihe Energie & Umwelt / Energy & Environment Band / Volume 79

Forschungszentrum Jülich GmbH
Institute of Solid State Research (IFF)

# Ultrafast vortex core dynamics investigated by finite-element micromagnetic simulations

Sebastian Gliga

Schriften des Forschungszentrums Jülich
Reihe Energie & Umwelt / Energy & Environment Band / Volume 79

ISSN 1866-1793 ISBN 978-3-89336-660-6

Bibliographic information published by the Deutsche Nationalbibliothek.
The Deutsche Nationalbibliothek lists this publication in the Deutsche Nationalbibliografie; detailed bibliographic data are available in the Internet at http://dnb.d-nb.de.

| | |
|---|---|
| Publisher and Distributor: | Forschungszentrum Jülich GmbH<br>Zentralbibliothek<br>52425 Jülich<br>Phone +49 (0) 24 61 61-53 68 · Fax +49 (0) 24 61 61-61 03<br>e-mail: zb-publikation@fz-juelich.de<br>Internet: http://www.fz-juelich.de/zb |
| Cover Design: | Grafische Medien, Forschungszentrum Jülich GmbH |
| Printer: | Grafische Medien, Forschungszentrum Jülich GmbH |
| Copyright: | Forschungszentrum Jülich 2010 |

Schriften des Forschungszentrums Jülich
Reihe Energie & Umwelt / Energy & Environment Band / Volume 79

D 464 (Diss., Duisburg, Univ., 2009)

ISSN 1866-1793
ISBN 978-3-89336-660-6

The complete volume ist freely available on the Internet on the Jülicher Open Access Server (JUWEL) at http://www.fz-juelich.de/zb/juwel

## Abstract

The investigations carried out in this thesis concern the ultrafast dynamics of a fundamental micromagnetic configuration: the vortex. Over the past decade, a detailed understanding of the dynamic and static properties of such magnetic nanostructures has been achieved as a result of close interplay between experiments, theory and numeric simulations. Here, micromagnetic simulations were performed based on the finite-element method.

The vortex structure arises in laterally-confined ferromagnets, in particular in thin-film elements, and is characterized by an in-plane curling of the magnetic moments around a very stable and narrow core. In the present study, a novel process in micromagnetism was found: the ultrafast reversal of the vortex core. The possibility of easily switching the core orientation by means of short in-plane field pulses is surprising in view of the very high stability of the core. Moreover, the simulations presented here showed that this reversal process unfolds on a time scale of only a few tens of picoseconds, which leads to the prediction of the fastest and most complex micromagnetic reversal process known to date. Indeed, the vortex core is not merely switched: it is destroyed and recreated in the immediate vicinity with an opposite direction. This is mediated by a rapid sequence of vortex-antivortex pair creation and annihilation subprocesses and results in a sudden burst-like emission of spin waves.

Equally fascinating is the ultrafast dynamics of an isolated magnetic antivortex, the topological counterpart of the vortex. The simulations performed here showed that the static complementarity between vortices and antivortices is equally reflected in their ultrafast dynamics, which leads to the reversal of the antivortex core.

A promising means for the control of the magnetization on the nanoscale consists in exploiting the spin-transfer torque effect. The study of the current-induced dynamics of vortices showed that the core reversal can be triggered via two distinct routes. The first is the resonant excitation by means of weak in-plane alternating currents. In this case, the reversal occurs rather slowly, after several nanoseconds. The simulations demonstrated a second route, namely, that short unipolar electrical excitations applied in the plane of the sample can equally lead to the reversal of the core within only a few hundreds of picoseconds. Despite this difference in switching times, the simulations showed that the micromagnetic details of the reversal are the same in both routes.

By comparing these two switching paths, the origin of the core switch, *i.e.* the physical parameter responsible for the reversal, was identified. The analysis demonstrated the existence of an energy barrier, which corresponds to the energy required to create a new vortex-antivortex pair. In the simulations, such pairs were spontaneously produced once a specific local energy density was reached. This finding predicts that vortex-antivortex pairs can be created by applying a strong, localized magnetic field.

## Zusammenfassung

Die Untersuchungen in dieser Dissertation betreffen die ultraschnelle Dynamik einer grundlegenden mikromagnetischen Konfiguration: den Wirbel. Durch die enge Zusammenarbeit von Experiment, Theorie und numerischen Simulationen konnte im letzten Jahrzehnt ein detailliertes Verständnis der dynamischen und statischen Eigenschaften solcher magnetischen Nanostrukturen erreicht werden. In dieser Arbeit werden mikromagnetische Simulationen mit der Finiten-Elemente-Methode durchgeführt.

Die Wirbelstruktur bildet sich in lateral eingeschränkten Ferromagneten aus, insbesondere Dünnschichtelementen, und ist durch eine ebene, kreisförmige Anordnung der magnetischen Momente um einen sehr stabilen und schmalen Kern charakterisiert. In der vorliegenden Untersuchung wurde ein neuartiger mikromagnetischer Prozess entdeckt: die ultraschnelle Umkehrung des Wirbelkerns. Die Möglichkeit, die Ausrichtung der Kernmagnetisierung durch kurze ebenen-parallele Feldpulse auf einfache Weise umzuschalten ist in Anbetracht der hohen Stabilität des Vortexkerns sehr überraschend. Die durchgeführten Simulationen zeigen, dass dieser Schaltprozess auf einer Zeitskala von nur wenigen zehn Pikosekunden stattfindet, und sagen daher den schnellsten und zugleich komplexesten bisher bekannten mikromagnetischen Schaltprozess voraus. Tatsächlich wird der Wirbel nicht einfach umgeschaltet, sondern aufgelöst und in unmittelbarer Nähe mit entgegengesetzter Kernmagnetisierung wiederhergestellt. Dies geschieht durch schnellablaufende Teilprozesse, bei denen Wirbel- und Antiwirbel-Paare entstehen und vernichtet werden. Dieser Prozess ist mit einer plötzlichen explosionsartigen Aussendung von Spinwellen verbunden.

Ebenso faszinierend ist die ultraschnelle Dynamik eines einzelnen magnetischen Anti-Wirbels, dem topologischen Gegenstück zum Wirbel. Es wird gezeigt, dass sich die statische Komplementarität zwischen Wirbel und Antiwirbel auch in ihrer ultraschnellen Dynamik widerspiegelt, nämlich im Schalten des Antiwirbelkerns.

Eine vielversprechende Methode, mit der die Magnetisierung auf der Nanoskala kontrolliert werden kann, besteht in der Verwendung des sogenannten Spin-Transfer-Torque-Effekts. Durch Untersuchungen zur strominduzierten Dynamik magnetischer Wirbel wurde festgestellt, dass das Schalten des Kerns auf zwei verschiedenen Wege bewirkt werden kann: In einem Fall wird der Wirbel durch einen schwachen Wechselstrom resonant angeregt. In diesem Fall tritt der Schaltprozess relativ langsam ein, nach einigen Nanosekunden. Die Simulationen zeigten einen zweiten Weg – kurze, unipolare elektrische Anregungen parallel zur Probenebene können ebenso ein Schalten des Kerns innerhalb von nur weniger Hundert Pikosekunden bewirken. Trotz dieser Unterschiede in den Schaltzeiten zeigten die Simulationen, dass die mikromagnetischen Details der Schaltprozesse in beiden Fällen gleich sind. Durch einen Vergleich dieser beiden Wege zum Schalten von Wirbelkernen konnten die relevanten physikalischen Parameter bestimmt werden, die das Schalten des Kerns bewirken. Die Analyse zeigte, dass eine Energiebarriere überwunden werden muss, die der für die Bildung eines Wirbel/Antiwirbel-Paars benötigten Energie entspricht. Es stellt sich heraus,

dass solche Paare spontan entstehen, sobald eine bestimmte lokale Energiedichte erreicht wird. Dies eröffnet die Möglichkeit, neue Wirbel/Antiwirbel-Paare durch ein starkes, lokalisiertes magnetisches Feld zu erzeugen.

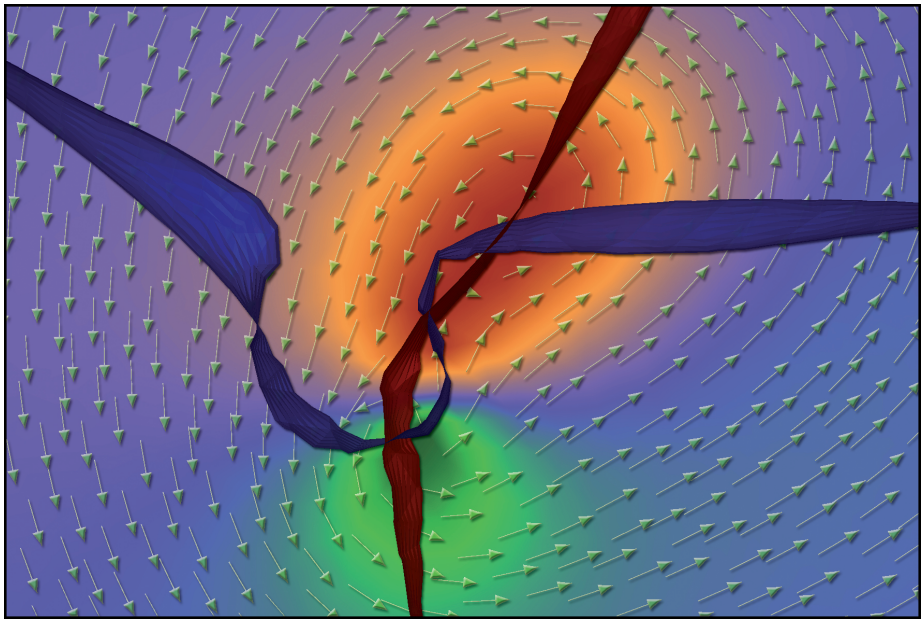

Vortex core reversal mediated by the production of a vortex-antivortex pair.

Schalten eines Wirbelkerns durch die Entstehung eines Wirbel/Antiwirbel-Paares.

# Contents

# 1 Introduction

The ability to study and manipulate the magnetic properties of matter on increasingly smaller scales is a defining feature of modern magnetism. The research leading to such advances has largely been stimulated by the rapid progress accomplished in information technology and the need for high-density non-volatile storage media ever since IBM introduced the first hard disk drive with the RAMAC project in the 1950s. Scientific curiosity is, however, at the origin of most advances in our understanding of magnetism. In this context, one of the striking examples of the impact of fundamental research is the discovery of giant magnetoresistance (GMR) [1, 2], for which the 2007 Nobel Prize was awarded to Grünberg and Fert. The discovery that the resistance of layered magnetic thin films separated by a non-magnetic layer strongly depends on the relative orientation of the magnetization in each layer quickly evolved from an exciting physical phenomenon into an application [3, 4] that changed the dynamics of the information technology sector.

As with GMR, modern applications of magnetic materials mostly involve thin films and laterally confined nanoscale structures. The direct observation of their unique magnetic properties has been pushed forward over the past decades by the development of imaging techniques with high spatial and temporal resolution [5]. For example, the exploitation of soft x-ray magnetodichroic phenomena using circularly polarized light (XMCD) [6, 7] allows the observation of dynamic phenomena on time scales below one hundred picoseconds with a spatial resolution down to tens of nanometers. In this technique, the imaged contrast is produced by the relative orientation between the local magnetization and the light helicity vector. Another important tool for the investigation of magnetization dynamics is Kerr microscopy [8], which measures the change in polarization of light reflected from the surface of a magnetic sample, due to its interaction with the magnetization. In addition to such wide field acquisition techniques, scanning probe techniques like Magnetic Force Microscopy (MFM) [9, 10] or Scanning Electron Microscopy with Polarization Analysis (SEMPA) [11, 12] allow the investigation of magnetic structures with a resolution ranging from a few tens of nanometers to a few nanometers. Magnetism on the atomic scale can be accessed experimentally by means of spin-polarized scanning tunneling microscopy (SP-STM) [13, 14]. In parallel to experimental techniques, the

development of powerful computer simulation tools and algorithms achieving predictive power has revealed further insights into the static and dynamic properties of nanomagnets.

The resulting interaction between experiments and simulations has led to the prediction and measurement of novel static magnetic configurations and unexpected dynamic properties in nanosystems due to lateral confinement and sharp interfaces. The properties of these systems are largely different from those of bulk magnets. A remarkable structure arising from magnetic confinement is the vortex. In ferromagnetic materials with finite geometries, the magnetization tends to form domain patterns, which close the magnetic flux [8]. In the center of such flux-closure structures, there is often a region of only a few nanometers in size forming a magnetic vortex, where the magnetization circulates around a core. At the core, in order to avoid a singularity of the exchange energy density, the magnetization lifts out of the plane. While this structure was predicted over forty years ago [15], it has only recently been confirmed experimentally using MFM [16], by exploiting the dipolar interaction between the vortex core and a sharp ferromagnetic tip. The use of SP-STM, which measures the spin-dependent tunneling current between a magnetic tip and the sample through a vacuum gap, has allowed to precisely determine the structure and dimensions of the core [17].

The aim of this thesis is to explore fundamental aspects of the magnetization dynamics of vortices, in particular their response to *ultrafast* excitations triggered by external fields and spin-polarized currents. The presented results are based on numeric simulations performed within the framework of micromagnetic theory. The theory describes the static and dynamic properties of the magnetization in mesoscopic and nanoscale laterally-confined ferromagnets[1].

Generally, the *fast* dynamics of magnetic structures such as domain walls and vortices can be obtained from micromagnetism by integrating the equation of motion of the magnetization, the Landau-Lifshitz-Gilbert equation. In most cases this is a tedious task that requires solving coupled differential equations, which are non-linear and non-local. A great simplification in this direction was achieved by Thiele [19], who reduced the problem to determining the expression of the forces acting on the magnetic structure. These results were later applied to vortices by Huber [20], leading to the analytic description of their dynamics. The first experimental observation of the dynamics of vortices made use of the Cotton-Mouton magneto-optical effect and allowed to determine the resonance frequency associated with the motion of domain walls coupled to a vortex [21]. These measurements established that the lowest excitation mode of the vortex is its rotation about the equilibrium position, also known as the *gyrotropic mode*. This was later also measured using time-resolved Kerr microscopy [22]. While the lateral resolution did not allow the direct imaging of the vortex motion, it provided further evidence for the gyrotropic motion. Finally, the motion of the vortex was imaged in response to short field pulses, a few hundreds of

[1] In terms of magnetic switching, we define as *ultrafast* time scales which are between a few and one hundred picoseconds. Faster excitations on the subpicosecond scale are possible [18]; these are however not described by micromagnetic theory.

picoseconds long, using XPEEM [23]. These experiments determined that the gyrotropic motion typically unfolds on the nanosecond timescale and that it is surprisingly the vortex core, which in spite of its small size governs this motion.

Despite their remarkable properties, vortices have largely been avoided in magnetic materials. Indeed, most applications of magnetism in reduced lateral dimensions involve the reversal of the magnetization. The magnetic switching in granular thin film media found in hard drives, or the reversal of the magnetization orientation in nanomagnets, which are part of various MRAM architectures or in proposed patterned storage media, therefore require reliable and fast operation. In this context, the nucleation of vortices constitutes an undesirable feature because it is not easily reproducible. The nanomagnets acting as data storage units are thus generally engineered through their shape and size to exhibit single-domain behavior, thereby avoiding the vortex state which would otherwise naturally form. However, even in such cases, the reversal can be inhomogeneous [24] and strongly dependent on edge imperfections, proceeding from nucleation sites and possibly involving the formation and propagation of vortices. Only Arrott's hysteron [25] provided a nucleation-free concept that used a vortex to drive the reversal of the magnetization in an MRAM memory cell at low switching fields [26].

This point of view of vortices has however dramatically changed over the past few years. Experiments performed by Van Waeyenberge *et al.* [27] using scanning x-ray transmission microscopy (XTM) on vortex dynamics excited at resonance have demonstrated that the vortex core could easily be reversed using bursts of a low in-plane alternating field, which was used to excite the gyrotropic motion. The strength of these bursts was of the order of one mT. This result is remarkable in view of the very high stability of the core [28], which is due to the exchange field. It was indeed found experimentally that about 300 mT are required to "crush" the core structure [29]. The experiment in Ref. [27] thus established a means of easily and dynamically switching between two stable core configurations which could also be promising for technological applications.

In the present work, the mechanism leading to the vortex core reversal is studied in detail. We find that this reversal is mediated by a series of complex subprocesses unfolding within only a few tens of picoseconds. In addition, the switching mechanism appears to be independent of the excitation type (which can be resonant or non-resonant). These results lead to the prediction of the fastest, yet most complicated, field-induced reversal mechanism known to date. It is indeed faster than precessional switching [30, 31], which allows the uniform reversal of the magnetization within a few hundreds of picoseconds.

The presented simulations are performed within the framework of micromagnetism. This is a continuum theory in which the magnetization is represented by a directional vector field of constant magnitude. Locally, the magnetization vector is an average over hundreds to thousands of atomic magnetic moments. The micromagnetic description uses quantum mechanical results such as the values of the gyromagnetic ratio and the Bohr magneton and constitutes a bridge between the atomistic description of magnetism (Heisenberg model) and domain theory. The foundations of micromagnetism were laid by Landau and

Lifshitz [32] and notably by Brown [33] who coined the term in the sixties, because it describes microscopic magnetic structures such as domain walls and vortices. These structures are determined from the competition between the exchange and magnetostatic interactions as well as various anisotropies.

Micromagnetic simulations are presently the best tool for investigating the ultrafast dynamic behavior of the magnetization on the nanoscale. Indeed, while an analytic description of the magnetization dynamics is often possible, it usually comes at the cost of a number of simplifying assumptions. For example, the results derived by Thiele mentioned earlier apply to rigid magnetic systems at equilibrium. In this framework, the description of ultrafast phenomena is intractable. In addition, simulations allow to study quantities which cannot easily be expressed analytically or accessed experimentally, such as the internal energy of complex three-dimensional systems [34] or their dynamics [35], and offer the possibility to systematically study the role of different parameters, which can be turned on or off. Simulations are thus complementary to theory and experiments and have become an indispensable tool for the fundamental understanding of magnetization dynamics as well as for the interpretation of experimental observations. In certain fields, this complementarity has evolved to the point where simulations have become an integral part of the experiments. For example, modeling of the experimental apparatus is an essential part of the measurement process in transmission electron microscopy. This allows to reach resolutions of the order of the picometer [36]. Recently, Vansteenkiste *et al.* [37] combined experimental data with simulated time-resolved XTM measurements to establish that the core of a gyrating vortex does not behave like a rigid structure, but is strongly distorted. This distortion occurs on a length scale of 10-20 nanometers, below the lateral resolution of the measurement technique. In scanning probe microscopy, reconstruction algorithms can compensate for tip-induced distortions and allow image simulation [38, 39]. Such advances are the result of tremendous increases in the performance and reliability of numeric algorithms, which have in effect allowed simulations to evolve into a distinct field of investigation. Simulations consequently do not only allow the understanding of, but also the *prediction* of complex phenomena and novel effects, thereby motivating experimental investigations.

In this thesis, the predictions made for the ultrafast dynamics of magnetic vortices are based on micromagnetic simulations using a fully three-dimensional finite-element algorithm. The finite-element method (FEM) allows an effective treatment of magnetization processes in samples with arbitrary shapes and smooth boundaries. At present, only a few FEM-based algorithms exist in micromagnetics. The algorithm used in this thesis [40] is a powerful simulation tool for micromagnetic problems [41, 34, 42]: it is flexible [43], fully parallelized and uses hierarchical matrix compression, which allows the computation of problems consisting of millions of discretization nodes using workstations. In the absence of matrix compression, solving such problems would typically require a supercomputer. It is thus possible to compute the dynamics of samples tens of micrometers large with a resolution of only a few nanometers, allowing for a multiscale approach.

This thesis is organized as follows. **Chapter 2** introduces micromagnetic theory and its scope. We describe the different energy contributions entering the computation of the effective field driving the magnetization dynamics. The static structure of magnetic vortices is also discussed, along with their associated topological indices. Details of the finite-element method used for the dynamic calculations are described in **chapter 3**. **Chapter 4** presents the analytic expression for the dynamics of magnetic vortices. We include a derivation of the Thiele equation and its application to the particular case of the vortex. In addition, we discuss fundamental features of vortex dynamics first described by simulations such as the strong distortion of the moving vortex core [44, 45] and vortex-antivortex annihilation [46].

**Chapters 5** to **9** detail our contributions to the study of vortex dynamics. The micromagnetic investigation of the vortex core reversal in response to ultrafast in-plane field pulses is presented in **chapter 5**. We show that this reversal process unfolds within a few tens of picoseconds and is mediated by a series of dramatic subprocesses resulting in the annihilation of the original vortex and the creation of a new one. This leads to predict the fastest field-induced magnetization reversal mechanism known to date [47, 48]. We show that this mechanism involves not only the production of a new vortex, but also of an antivortex. Consequently, in **chapter 6**, we investigate the ultrafast response of *anti*vortices [49, 50] to in-plane field pulses.

In addition to magnetic fields, the use of spin-polarized currents represents a promising means of manipulating the magnetization on the nanoscale. At the origin of the GMR effect is the fact that an electric current becomes spin-polarized in a ferromagnet. Slonczewski and Berger [51, 52] subsequently predicted the inverse phenomenon, namely that the spin polarization of the conduction electrons can influence the magnetization state of the ferromagnet. In this context, the dynamic behavior of domain walls under the influence of in-plane spin-polarized currents has been intensively studied both theoretically and experimentally for example in Refs. [53, 54, 55, 56]. In **chapter 7**, we investigate the influence of in-plane spin-polarized currents on the dynamics of vortices. In contrast to experimental observations which have established that the core can be excited [45] and reversed [57] through resonant excitation with alternating currents, we demonstrate that the core can also be reversed in a controlled manner by means of short and strong single current pulses [58].

The existence of different pathways for reversing the vortex core requires a fundamental quantity, which determines the reversal. While it has recently been suggested that the switching is controlled by the velocity of the core [57, 59], experiments [37] have found discrepancies between the measured and predicted values of this velocity. In **chapter 8**, we adopt a different approach by considering the energy of the vortex. We show that the core reversal occurs once a well-defined energy threshold is reached. This threshold corresponds to the energy necessary for the production of a vortex-antivortex pair. In contrast to the velocity interpretation, our approach allows a full description of the reversal process.

In **chapter 9**, we prove the validity of our approach by demonstrating that

vortex-antivortex pairs can be produced in a controlled manner in a ferromagnet by locally increasing the energy density above the determined threshold. We show how our approach introduces a new possibility for switching the core without exciting the vortex and may allow to simplify the experimental measurement of this ultrafast reversal process.

# 2

# Fundamental aspects of micromagnetism

The microscopic structure of ferromagnets is typically characterized by magnetic domains: regions of uniform magnetization up to hundreds of microns wide. The existence of domains with different magnetic orientations which minimize the total stray field was postulated by Weiss [60, 61] and their existence confirmed by Bitter [62, 63], who used fine magnetic powder to image the domain patterns. The powder concentrates at domain boundaries due to the high stray field gradient present in those regions, revealing the extent and arrangement of the domains. Later, Bloch [64] provided a theoretical analysis of the 'walls' that form in the regions connecting different domains. Landau and Lifshitz then showed that the magnetic structure of these walls can be obtained analytically by minimizing the total energy of the system [32]. Micromagnetic theory [33, 65] was formulated by Brown and consists in a more general approach than the one adopted by Landau and Lifshitz. Indeed, it allows not only to calculate the structure of domain walls but also predicts their existence.

Micromagnetism therefore predicts and describes fundamental magnetization structures, which typically only span a few tens to hundreds of nanometers. The domain wall described above is one of these structures. Two main types of walls are distinguished based on the plane of rotation of the magnetization. In practice however, combinations of these types are observed, giving rise to new structures. This is for example the case of cross-tie walls. It was indeed the theoretical analysis of cross-ties that led to predict the existence of another fundamental structure: the vortex [15]. Magnetic singularities, or Bloch points, form yet another fundamental configuration predicted by micromagnetic theory [66]. These equally arise in the dynamic processes investigated in this thesis.

The *dynamic* behavior of the magnetization was described by Landau and Lifshitz [32]. Gilbert [67, 68] later derived an equivalent description using a different formulation for the damping. The resulting Landau-Lifshitz-Gilbert equation describes the time evolution of the magnetization, including dynamic effects such as spin waves, normal oscillatory modes of the magnetization or magnetization reversal processes. Micromagnetic theory is thus today an in-

valuable tool for the investigation of the structure and dynamic behavior of nanoscale systems. In this chapter, we present fundamental aspects of micromagnetic theory, focusing on the static structure of the vortex. We also describe the general structure of domain walls, in particular the cross-tie wall, due to its historic importance. In addition, we present the Landau-Lifshitz-Gilbert equation as well as its extension for spin-polarized currents.

## 2.1 Energy terms

In micromagnetism, the magnetization, *i.e* the density of magnetic moments, is represented by a continuous vector field $\boldsymbol{M}(\boldsymbol{x})$. Each vector has a constant length $M = M_s$, where $M_s$ is the saturation magnetization of the material, and only its direction is allowed to vary. Very often, the reduced magnetization is used, defined as $\boldsymbol{m} = \boldsymbol{M}/M_s$. The micromagnetic problem thus consists in determining the direction of $\boldsymbol{m}(\boldsymbol{x})$ at each point $\boldsymbol{x}$. For static configurations this can be achieved through the minimization of the free energy of the system. The most important contributions to the free energy are described in this section. The entropy contribution is neglected in this thesis, which constitutes a good approximation at temperatures far below the Curie point.

### 2.1.1 Exchange energy

In quantum mechanics, the exchange interaction between neighboring atomic spins giving rise to ferromagnetism results from the exclusion principle. This reduces the electrostatic potential between unpaired $3d$ electrons in neighboring atoms whose spins are aligned parallel to each other. In micromagnetism, the exchange interaction is derived from the Heisenberg Hamiltonian with classical vectors replacing the spin operators [32]. Assuming only small deviations in the angle between neighboring magnetization vectors, the exchange energy density in the continuum limit is of the form

$$e_{\text{exc}} = A\left[(\boldsymbol{\nabla} m_x)^2 + (\boldsymbol{\nabla} m_y)^2 + (\boldsymbol{\nabla} m_z)^2\right], \tag{2.1}$$

where $A$ is the material-dependent exchange constant expressed in J/m. The exchange energy thus vanishes when the magnetization is perfectly aligned while deviations from this alignment are penalized.

The value of the exchange constant can be obtained from ab-initio density functional theory calculations [69]. Experimentally, it can be determined for example from spin-wave resonance measurements, based on the dispersion relation of volume modes [70]. For iron $A = 2.1 \times 10^{-11}$ J/m whereas for Permalloy ($Ni_{80}Fe_{20}$) $A = 1.3 \times 10^{-11}$ J/m.

### 2.1.2 Magnetostatic energy

According to Faraday's law [71], the induction $\boldsymbol{B}$ is related to the magnetic field $\boldsymbol{H}$ in the vacuum by

$$\boldsymbol{B} = \mu_0 \boldsymbol{H}, \tag{2.2}$$

where $\boldsymbol{B}$ is in units of Tesla ($\equiv$Vs/m$^2$), and $\boldsymbol{H}$ is in A/m. Here, $\mu_0$ is the magnetic constant introduced by the SI unit system, also called vacuum permeability, which is fixed at $\mu_0 = 4\pi \times 10^{-7}\ \frac{Vs}{Am}$. Inside a magnetic material, taking into account the magnetization $\boldsymbol{M}$,

$$\boldsymbol{B} = \mu_0(\boldsymbol{H} + \boldsymbol{M}). \tag{2.3}$$

where $\boldsymbol{M}$ is in A/m. Maxwell's equations inside the material then read

$$\begin{aligned} \boldsymbol{\nabla} \cdot \boldsymbol{B} &= 0 && (2.4)\\ \boldsymbol{\nabla} \times \boldsymbol{H}_{\text{ext}} &= \mu_0 \boldsymbol{j} && (2.5)\\ \boldsymbol{\nabla} \times \boldsymbol{H}_{\text{dem}} &= 0. && (2.6) \end{aligned}$$

Two types of fields are distinguished: the applied field $\boldsymbol{H}_{\text{ext}}$ produced by an external current and the internal demagnetizing field $\boldsymbol{H}_{\text{dem}}$.

The general solution to Ampère's law (2.6) inside the ferromagnet is of the form [72]:

$$\boldsymbol{H}_{\text{dem}} = -\boldsymbol{\nabla} U_{\text{dem}}, \tag{2.7}$$

where $U_{\text{dem}}$ is a magnetostatic scalar potential. In conjunction with (2.3) and (2.4), it results that

$$\nabla^2 U_{\text{dem}} = \boldsymbol{\nabla} \cdot \boldsymbol{M}. \tag{2.8}$$

The solution of the Poisson equation (2.8) has the form

$$U_{\text{dem}}(\mathbf{r}) = \frac{1}{4\pi\mu_0} \left[ -\int_{V'} \frac{\boldsymbol{\nabla} \cdot \boldsymbol{M}(\boldsymbol{r}')}{|\boldsymbol{r} - \boldsymbol{r}'|} d^3 r' + \int_{S'} \frac{\boldsymbol{M}(\boldsymbol{r}') \cdot \boldsymbol{n}}{|\boldsymbol{r} - \boldsymbol{r}'|} d^2 r' \right]. \tag{2.9}$$

The first integration is performed over the magnetic volume while the second term is a surface integral. The vector $\boldsymbol{n}$ is normal to the surface, directed outwards.

Equation 2.9 introduces the concept of volume and surface charges as sources of the demagnetizing field, analogous to electrostatics [71]:

$$\begin{aligned} \rho &= -\mu_0(\boldsymbol{\nabla} \cdot \boldsymbol{M}) && \text{volume charge density,} && (2.10a)\\ \sigma &= \mu_0(\boldsymbol{M} \cdot \boldsymbol{n}) && \text{surface charge density.} && (2.10b) \end{aligned}$$

Generally, the magnetostatic field outside the ferromagnet is referred to as the "stray field", whereas the "demagnetizing field" describes the field inside the sample, which opposes the direction of the magnetization.

The energy density term arising from the demagnetizing field is

$$e_{\text{dem}} = -\frac{1}{2}\mu_0(\boldsymbol{H}_{\text{dem}} \cdot \boldsymbol{M}) \tag{2.11}$$

where the factor $\frac{1}{2}$ excludes self-interactions. The total magnetostatic energy $\int e_{\text{dem}} dV$ can also be written in terms of an integration over the entire space [33, 65]:

$$E_{\text{dem}} = \frac{\mu_0}{2} \int_{\text{all space}} \boldsymbol{H}_{\text{dem}}^2 \, dV. \tag{2.12}$$

The above equation highlights two essential properties of the magnetostatic energy:

- The total magnetostatic energy of a ferromagnetic body is always positive;
- The magnetostatic energy can only be minimized by avoiding the formation of magnetic charges.

The second point expresses the fact that the magnetization will tend to align with the boundaries such that $\boldsymbol{M} \cdot \boldsymbol{n} \to 0$ in a way that also minimizes $\boldsymbol{\nabla} \cdot \boldsymbol{M}$ as much as possible. This is known as the "pole avoidance principle" [65].

The consequence of this principle is the formation of closure domain configurations, or vortex states, in magnetic systems above a critical size [73]. We describe magnetic vortices in detail in section 2.2.3.

### 2.1.3 Zeeman energy

The contribution of an external field $\boldsymbol{H}_{\text{ext}}$ (2.5) is accounted for by the Zeeman energy term

$$e_{\text{zee}} = -\mu_0 (\boldsymbol{H}_{\text{ext}} \cdot \boldsymbol{M}), \tag{2.13}$$

which depends on the relative orientation of the external field with respect to the local magnetization. The value of $e_{\text{zee}}$ is thus a minimum when these are parallel and have same orientation.

### 2.1.4 Anisotropy energy

The energy of a ferromagnet also depends on the orientation of the magnetization with respect to directions defined by the crystal structure of the material, which gives rise to preferential directions or *easy axes*. This effect is mainly due to the quenching of $3d$ orbitals resulting from the competition between spin-orbit coupling and the electrostatic potential of the lattice.

The simplest case is that of *uniaxial* anisotropy. The anisotropy energy density can then be expressed as function of the relative orientation of the magnetization and the anisotropy axis $\boldsymbol{k}$. To second order, it reads:

$$e_{\text{ku}} = -K_{\text{u1}} (\boldsymbol{m} \cdot \boldsymbol{k})^2 + K_{\text{u2}} (\boldsymbol{m} \cdot \boldsymbol{k})^4. \tag{2.14}$$

The constants $K_{\text{u1}}$ and $K_{\text{u2}}$ are expressed in $\text{J/m}^3$. While higher order terms can be added, they usually do not play a significant role [8]. Considering the first-order term only, if $K_{\text{u1}} > 0$ the anisotropy is axial, while if $K_{\text{u1}} < 0$, it is planar with an anisotropy plane perpendicular to the easy axis.

For a *cubic* anisotropy, the energy density is defined by

$$e_{\mathrm{kc}} = K_{\mathrm{c1}}(m_x^2 m_y^2 + m_y^2 m_z^2 + m_x^2 m_z^2) + K_{\mathrm{c2}} m_x^2 m_y^2 m_z^2 \tag{2.15}$$

where $m_{x,y,z}$ are the components of $\boldsymbol{m}$ along the cubic axes.

Preferred directions of the magnetization can also be determined due to *shape anisotropy*. This type of anisotropy has in fact a magnetostatic origin: it results from the formation of surface magnetic charges (2.10b) at the ferromagnet's boundary. Analytically, this anisotropy is described by demagnetizing factors for uniformly magnetized bodies [72, 74]. More generally, the term "shape anisotropy" describes the tendency of the magnetization to align parallel with the sample edges or in the plane of thin films in order to avoid the formation of surface charges.

Another anisotropy term describes the behavior of the magnetization at *surfaces*. Originally introduced by Néel [75], it can play an important role in ultrathin magnetic films and generally nanostructures with a high surface-to-volume ratio. In the first order, the energy density is given by

$$e_{\mathrm{srf}} = K_{\mathrm{s}}[1 - (\boldsymbol{m} \cdot \boldsymbol{n})^2]. \tag{2.16}$$

The surface anisotropy coefficient $K_{\mathrm{s}}$ is expressed in $\mathrm{J/m^2}$ and, when it is positive, favors the perpendicular alignment of the magnetization with respect to the surface. The effects described by the surface anisotropy are magnetocrystalline in nature, due to spin-orbit coupling and the presence of uncompensated bonds of the surface atoms. A general anisotropy term can be defined, which takes into account the competition between surface and bulk anisotropies:

$$K = \frac{K_{\mathrm{s}}}{h} + K_{\mathrm{d}} \tag{2.17}$$

where $h$ is the film thickness. $K_{\mathrm{d}}$ denotes the bulk anisotropy, which includes the magnetocrystalline and magnetostatic contributions. In thin films, the magnetostatic anisotropy is given by $\frac{1}{2}\mu_0 M_s^2$, sometimes called shape anisotropy. There thus is a particular thickness at which $K = 0$ and a spin-reorientation transition occurs, from an in-plane to an out-of-plane magnetization orientation, or vice-versa.

Other sources of anisotropy can also arise for example from magnetoelastic interactions which can lead to the deformation of a magnetic body in an external field or to the change in the magnetic configuration following mechanical strains. These are however not considered here.

### 2.1.5 Effective field

From the above, it follows that in the absence of entropy, the the total energy of the system is given by:

$$E_{\mathrm{tot}} = \int_V (e_{\mathrm{exc}} + e_{\mathrm{dem}} + e_{\mathrm{zee}} + e_{\mathrm{an}})\ dV + \int_S e_{\mathrm{srf}}\ dS \tag{2.18}$$

where $e_{\text{an}}$ includes all anisotropy contributions. This energy depends on the spatial distribution of the magnetization and hence, the minimization of $E_{\text{tot}}$ yields the equilibrium magnetic configuration. This minimization is achieved through the variational method introduced by Brown [33],

$$\frac{\delta E_{\text{tot}}}{\delta \boldsymbol{m}} = 0, \tag{2.19}$$

where $\frac{\delta E_{\text{tot}}}{\delta \boldsymbol{m}}$ is the functional derivative of the total energy with respect to the magnetization $\boldsymbol{m}$. This leads to the torque equation [33]:

$$\boldsymbol{m} \times \boldsymbol{H}_{\text{eff}} = 0. \tag{2.20}$$

The equilibrium magnetization configuration is thus achieved when the magnetization $\boldsymbol{m}$ is aligned with an effective field, resulting from the contributions of the exchange, magnetostatic and anisotropy terms and the external field:

$$\boldsymbol{H}_{\text{eff}} = \frac{2A}{\mu_0 M_s}\nabla^2 \boldsymbol{m} + \boldsymbol{H}_{\text{dem}} - \frac{1}{\mu_0 M_s}\frac{\delta e_{\text{an}}}{\delta \boldsymbol{m}} + \boldsymbol{H}_{\text{ext}}. \tag{2.21}$$

More than a single configuration is usually possible and a unique solution exists only for sufficiently small confined systems.

## 2.2 Magnetic structures

### 2.2.1 Characteristic lengths

The continuum description of the magnetization implies that abrupt changes in the magnetization are not allowed: these are smoothened out over a few nanometers by the exchange interaction. This distance defines the exchange length, *i.e.* the smallest distance over which inhomogeneities can occur at equilibrium[1].

In bulk materials or extended films, magnetostatic effects are usually negligible compared to anisotropy effects, such that the exchange and anisotropy energy terms are dominant. Considering for example a first-order uniaxial anisotropy, the competition between the two energy terms (2.1) and (2.14) yields the magnetocrystalline exchange length, also called Bloch wall parameter:

$$l_{\text{K}} = \sqrt{\frac{A}{K_{\text{u}}}}. \tag{2.22}$$

In confined magnets, it is rather the competition between the exchange and demagnetizing (2.11) energy terms which yields the magnetostatic exchange length:

$$l_{\text{exc}} = \sqrt{\frac{2A}{\mu_0 M_s^2}}. \tag{2.23}$$

[1]There are however exceptional cases when large inhomogeneities of the magnetization can occur even on atomic distances. This occurs in the presence of a magnetic singularity, described in section 2.2.4

Depending on the situation, $l_K$ or $l_{\text{exc}}$ defines the smallest relevant micromagnetic scale. In soft magnetic nanoelements where magnetostatic effects are large (*e.g.* shape anisotropy), the exchange length is typically defined by (2.23). In such cases, the magnetostatic exchange length can also determine the magnetization reversal mode [76].

By analogy, another length can be defined to quantify the perturbation induced by an external field:

$$l_{\text{H}} = \sqrt{\frac{2A}{\mu_0 M_s H_{\text{ext}}}}. \tag{2.24}$$

This "exchange length of the external field" [77] quantifies the distance over which it perturbs the orientation of the magnetization.

### 2.2.2 Domains and walls

The continuous transition of the magnetization between oppositely-oriented ferromagnetic domains is ensured by the domain walls [64]. Two main types of transitions are usually distinguished. The first one is the Bloch wall, which consists in the rotation of the magnetization parallel to the wall plane [32] and is schematically represented in Fig. 2.1a. This structure circumvents the formation of volume charges, albeit at the expense of the formation of surface charges. The width of the domain wall is of $\pi l_{\text{K}}$ [78]. It typically occurs in thicker films as well as in bulk materials. In films whose thickness is comparable to the domain wall width, a lower demagnetizing energy is achieved through the in-plane rotation of the magnetization, despite the formation of volume charges [79]. This

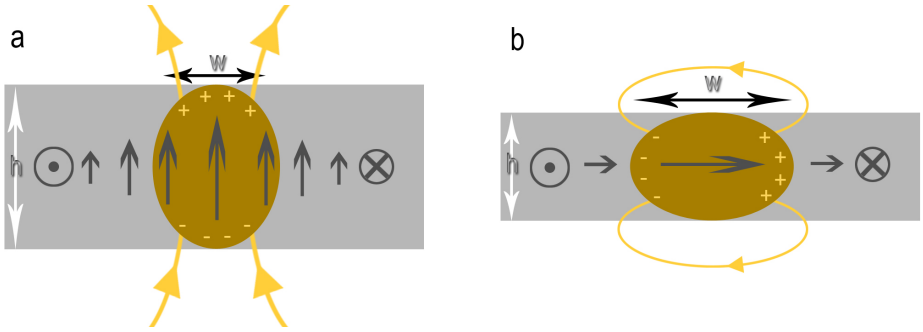


Figure 2.1: Schematic representation of the structure of Bloch and Néel walls. **a**, Bloch wall in a film of thickness $h$. The arrow lengths represent the magnitude of the magnetization component along the thickness. The resulting surface charges and stray field are schematically indicated. **b**, The Néel wall occurs in thinner films and is characterized by the formation of volume charges. Arrow lengths represent the magnetization component along the width of the wall. The stray field gives rise to the *Néel caps* which are typically visible on MFM images.

transition characterizes the Néel-type wall illustrated in Fig. 2.1b, which in the simplest analytic model has a width of $\pi l_{\mathrm{exc}}$. Another type of domain wall can be found in narrow thin magnetic strips. This is the head-to-head domain wall [80], where the magnetization direction in the domains is perpendicular to the domain wall plane, as opposed to the Bloch and Néel walls, where the magnetization is parallel to the wall plane.

Typically, more than a type of transition occurs in ferromagnetic samples of intermediate thickness, giving rise to domain walls with composite structures. One such example is the cross-tie wall [81], shown in Fig. 2.2a in a 40 nm thick Permalloy film. This wall consists of alternating Bloch and Néel-type transitions [82]. The structure of the cross-ties was theoretically studied by Feldtkeller and Thomas [15] who investigated singular regions called "circular" and "cross" Bloch lines. The circular Bloch line is characterized by a circulating in-plane magnetic structure with a perpendicular magnetization in the center. It is also called a vortex, while the cross Bloch line is known as an *anti*vortex.

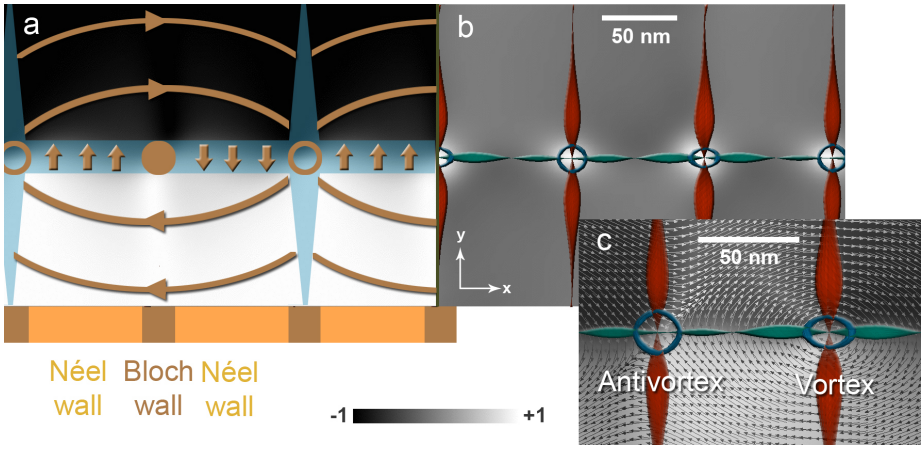


Figure 2.2: Simulated cross-tie wall in a micron-sized Permalloy sample. **a**, The cross-tie is composed of Bloch and Néel-type walls. Brown arrows indicate the circulation of the magnetization in the plane of the sample while full and open circles respectively indicate the succession of circular and cross Bloch lines. The greyscale represents the x component of the magnetization, highlighting the domains. The pale blue regions correspond to the Bitter pattern produced by the volume charges in the cross-tie structure, as observed in [81]. **b**, In a micromagnetic view of the same structure, the succession of vortices and antivortices is highlighted. The green and red "ribbons" represent the isosurfaces along which $m_x = 0$ and $m_y = 0$, respectively. Their intersection marks the location of the core of the structures where $m_z$ is maximal. The blue cylinders represent the surface along which $m_z = 0.7$, giving a measure of the core diameter. Here, the greyscale represents the z component of the magnetization. **c**, Detail of the in-plane magnetization of a vortex and an antivortex.

The cross-tie wall can thus be seen as a succession of vortices and antivortices, as shown in Fig. 2.2b,c where we use an isosurface representation introduced in Ref. [46]. The emphasis on the smallest fundamental magnetization structures reflects the transition from domain theory to the theory of micromagnetism, as suggested in Fig. 2.2b, where the focus is on the vortices and their core, instead of the surrounding domains.

### 2.2.3 Magnetic vortices

Vortices result from the tendency of the magnetization to form flux-closure patterns and are frequently found in confined mesoscopic ferromagnetic bodies. In thin-films, their structure is characterized by the circulation of the in-plane magnetization around a nanometer-sized core. At the center, the magnetization rotates out of the plane as a result of the exchange interaction, forming an extremely stable structure [28]. The simplest example of a vortex structure occurs in cylindrical-shaped samples above the single-domain limit [83, 84], as shown in Fig. 2.3a.

The radius of the vortex core is determined by the competition between the magnetostatic and exchange energies. Formally, it is defined by the slope of the in-plane component of the magnetization at the center of the vortex [8, 15] (as shown in Fig. 2.3c). It takes the same form as the definition of the domain wall

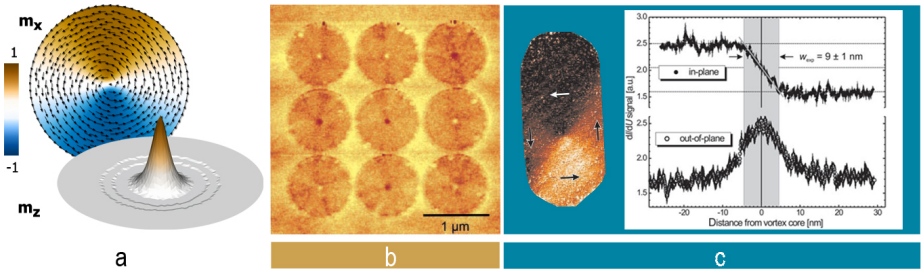


Figure 2.3: **a**, Simulated in-plane and out-of-plane magnetic structures of a vortex in a disk-shaped Permalloy sample 100 nm in radius and 20 nm thick. The arrows indicate the circulation of the in-plane magnetization. The topography of the out-of-plane component of the magnetization ($m_z$) shows the structure of the core. The simulation results are based on the minimization of the total energy of the system. **b**, Experimental observation of the vortex core in 50 nm thick circular micron-sized Permalloy dots using MFM. The dark and light spots at the center of the disks indicate the orientation of the core, where the dark spots are cores oriented towards the viewer. From *T. Shinjo,* et al., *Science 289, 930 (2000).* Reprinted with permission from AAAS. **c**, Measurement of the vortex in-plane and out-of-plane magnetization components in a 10 nm thick Fe nanoisland using SP-STM. From *A. Wachowiak,* et al., *Science 298, 577 (2002).* Reprinted with permission from AAAS.

width [78]:

$$r_{\mathrm{core}} = \left( \left. \frac{d(\sin\varphi)}{dr} \right|_{r=0} \right)^{-1} \tag{2.25}$$

where $\varphi$ is the polar angle of the in-plane magnetization. This radius is of the order of the magnetostatic exchange length of the material in thin films [15], as confirmed by numerous experimental observations, summarized in Ref. [85]. Table 2.1 gives the values of the exchange constant and saturation magnetization, along with the approximate core radius for vortices in different materials.

Following the variational approach in Ref. [86], the core radius is given as a function of film thickness $h$ by:

$$r_{\mathrm{core}} = 0.68\, l_{\mathrm{exc}} \left( \frac{h}{l_{\mathrm{exc}}} \right)^{1/3}. \tag{2.26}$$

The values obtained from this equation are in very good agreement with the results of micromagnetic simulations [41, 84]. We note that in ultrathin films, the core maintains its cylindrical structure throughout the sample thickness. However, in films which are typically thicker than 10–20 nm the core displays variations in thickness. This results in a wider structure in the bulk of the film and a narrower radius at the surfaces which minimizes the formation of surface charges.

Owing to its small dimensions, the vortex core only became experimentally accessible with the development of imaging techniques with high spatial resolution. The first observation was reported by Shinjo *et al.* [16] using MFM, shown in Fig. 2.3b. Quantitative measurements of the core radius performed using spin-polarized STM [17] (Fig 2.3c) and transmission electron microscopy [87, 88, 89] are in good agreement with the analytic and numeric micromagnetic predictions.

Different parameterizations have been suggested to analytically describe the distribution of the magnetization within the core. Feldtkeller and Thomas [15] used an exponential trial function reflecting the decay of the out-of-plane component of the magnetization with increasing radius $r$. Using a variational approach, Usov and Peschany [86] suggested an expression consisting of two parts,

| Material | A [J/m] | $M_s$ [A/m] | $r_{core}$ [nm] |
|---|---|---|---|
| Fe | $2.1 \times 10^{-11}$ | $1.71 \times 10^{6}$ | 3.4 |
| Co | $3.0 \times 10^{-11}$ | $1.40 \times 10^{6}$ | 5.0 |
| Ni | $9.0 \times 10^{-12}$ | $4.90 \times 10^{5}$ | 7.7 |
| Permalloy | $1.3 \times 10^{-11}$ | $7.96 \times 10^{5}$ | 5.7 |

Table 2.1: Approximate vortex core radius in different ferromagnetic materials, based on the magnetostatic exchange length. Contributions from anisotropy terms are typically negligible. Based on Refs. [85, 90].

separating the core with an out-of-plane magnetization from the rest of the vortex where the magnetization lies in the plane. Arrott proposed a parameterization based on hyperbolic functions [91] which are well suited for the description of vector fields, while Hubert and Schäfer introduced a generalized trial function [8]. These parameterizations are given below:

$$\textit{Feldtkeller:} \qquad m_z = e^{-2r^2/\beta^2} \tag{2.27}$$

$$\textit{Hubert \& Schäfer:} \qquad m_z = \sum c_i e^{-2r^2/\beta_i^2}, \qquad \sum c_i = 1 \tag{2.28}$$

$$\textit{Arrott:} \qquad m_z = \operatorname{sech}(r/\lambda) \tag{2.29}$$

$$\textit{Usov:} \qquad m_z = \begin{cases} \sqrt{1 - \left(\dfrac{2\delta r}{\delta^2 + r^2}\right)^2}, & 0 \le r \le r_{\text{core}} \\ 0, & r_{\text{core}} \le r \le R \end{cases} \tag{2.30}$$

where $R$ is the vortex radius. The parameters $\beta, \lambda$ and $\delta$ are determined from the minimization of the total energy and are of the order of the exchange length. The resulting core profile is plotted in Fig 2.4 for each expression, along with the profile predicted by micromagnetic simulations for a Permalloy disk-shaped sample with a radius of 100 nm and 20 nm thickness. The simulations reveal the existence of a circular region around the core where the magnetization points in a direction opposite to the core magnetization [41]. This "dip" in the static magnetization distribution is attributed to the influence of the strong core demagnetizing field [41], estimated to about 440 mT from the simulations performed in this thesis. This dip has also been experimentally observed in

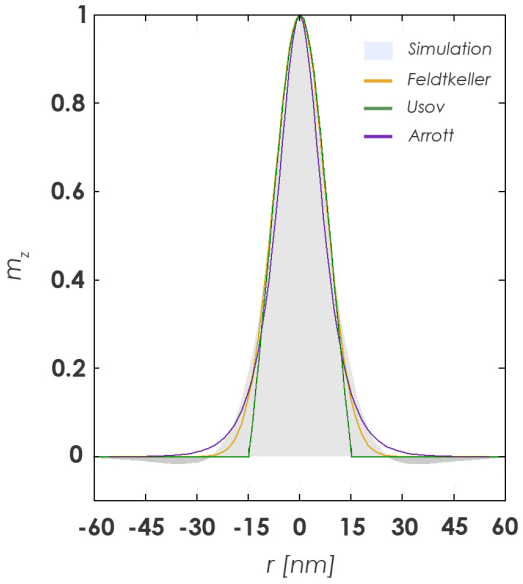


Figure 2.4: Distribution of the out-of-plane component of the vortex core. The different parameterizations described in the text are compared to the core profile obtained from micromagnetic simulations. The calculations and the simulations are for a Permalloy disk of radius 100 nm and thickness 20 nm. The dip in the magnetization in the vicinity of the core is clearly visible in the simulated profile.

Ref. [17] and of the analytic parameterizations, only the one suggested by Hubert and Schäfer can in principle reproduce this subtle feature [8]. While it only represents a small correction to the static shape of the vortex, we show in chapters 4 and 5 that its evolution plays an important role in the ultrafast dynamics of vortices.

In order to describe the intrinsic symmetries of the vortex, topological indices can be defined. Thus, the orientation of the core with respect to the plane of the vortex is described by its *polarization*, which takes the values $p = +1$ or $p = -1$, corresponding to the "up" and "down" states. The *vorticity*[2] $\varphi_0$ quantifies the direction of circulation of the in-plane magnetization, such that $\varphi_0 = +1$ for the counter-clockwise direction. It can be defined as the $z$ component of the vector $\nabla \times \mathbf{m}$. This circulation produces a full turn of the magnetization along the perimeter of the vortex, such that the angle $\varphi$ enclosed by the in-plane magnetization with an arbitrary reference axis is $2\pi$. The number of turns of the magnetization around the core is given by the *winding number*, which is formally defined by the contour integral

$$n = \frac{1}{2\pi} \oint \frac{d\varphi}{dS}\, dS \tag{2.31}$$

around the perimeter $S$ of the vortex. As illustrated in Fig. 2.5a,b, the winding number for a vortex is $n = 1$, while $n = -1$ characterizes the antivortex structure. This provides a topological basis for the stability of vortices and antivortices[3]: if the magnetization winds $n$ times around the perimeter of the structure, it cannot be smoothly changed to another value [92]. Therefore, within a magnetic sample, the total winding number is a topological conservation number [93]. This implies that the formation of a vortex structure within the sample is necessarily accompanied by the formation of an antivortex, unless the vortex nucleates at the sample boundary.

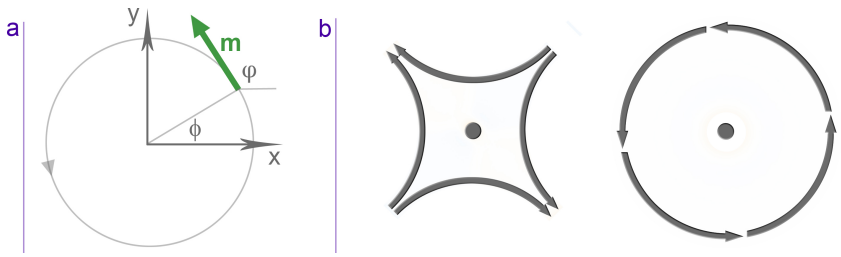


Figure 2.5: Winding number of a vortex and an antivortex. **a**, Schematic illustration of the winding number n. The angle $\alpha$ is enclosed by the magnetization with the x axis. **b**, In-plane structure of an antivortex with n $= -1$, as compared to the vortex structure.

[2] This quantity is also often referred to as *chirality* in the literature.

[3] We show in chapter 6 that an isolated magnetic antivortex is in fact metastable. This is however attributable to magnetostatics.

Antivortices (Fig. 2.5b) equally possess a bistable core ($p = \pm 1$) and their in-plane structure is characterized by regions with strong divergences of the magnetization, leading to the presence of magnetic volume charges. When imaged with MFM, these produce characteristic patterns that allow to distinguish them from vortices, as shown by Shigeto *et al.* [94] who imaged antivortices in cross-ties as well as isolated antivortices.

Following Fig. 2.5, the in-plane distribution of a vortex can be described in terms of the polar angle $\phi$ and the vorticity $\varphi_0$ [95]:

$$\varphi = n\phi + \varphi_0 \frac{\pi}{2}, \tag{2.32}$$

where $n$ is the winding number. The value of $\phi$ can be expressed within the complex plane $x + iy$ as:

$$\phi = \arg(x + iy). \tag{2.33}$$

For antivortices, the magnetization distribution can equally be described using (2.32). While these strictly do not possess a vorticity, a similar quantity can be defined [96], which is useful in describing the dynamic behavior of the structure in response to external fields applied at different angles with respect to the antivortex structure.

We describe in chapter 4 how the winding number and the polarization play a decisive role in the dynamics of vortices and antivortices studied in this thesis. In this context, another topological index can be defined, known as the skyrmion number $q$ [97] (also called Pontryagin index), which for vortices and antivortices is given by [98]:

$$q = \frac{1}{2} np. \tag{2.34}$$

This equally is a topological conservation number and its implications are detailed in section 4.3.2.

### 2.2.4 Bloch points

Another structure of particular interest in micromagnetism is the Bloch point [66]. It forms in magnetic configurations in which the transition between oppositely magnetized regions cannot proceed continuously, leading to a point with vanishing magnetization. While such a singularity cannot be investigated within the framework of micromagnetism, it can be shown that the magnetization is well-behaved on a closed sphere of radius $R$ around the Bloch point and the exchange energy of the structure is given analytically by [99]:

$$E_{\mathrm{exc(BP)}} = 8\pi AR. \tag{2.35}$$

The typical radius $R$ of such a structure in Permalloy for example has been found to be of about 10 nm from micromagnetic simulations [28]. The Bloch point is thus defined by the configuration of the magnetization surrounding it. Topologically, the simplest configuration of the Bloch point assumes the form [100]:

$$\boldsymbol{M} = \pm M_s \hat{\boldsymbol{r}} \tag{2.36}$$

in which the magnetization radially converges or diverges as illustrated in Fig. 2.6a, thereby defining "negative" and "positive" Bloch points. In effect, an infinite number configurations can occur which can be obtained through orthogonal transformations of (2.36). On of them is shown in Fig. 2.6b. The exchange energy (2.35) is the same for all the configurations.

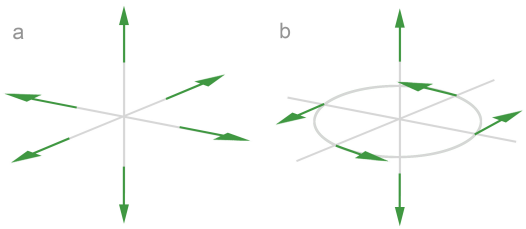


Figure 2.6: Two possible magnetic configurations around a Bloch point. The green arrows represent the orientation of the magnetization. **a**, Diverging structure. **b**, Circulating structure described by a 90° rotation of the configuration shown in **a** about the $z$ axis.

## 2.3 Magnetization dynamics

So far, we have only considered static magnetic structures. We introduce here the Landau-Lifshitz-Gilbert equation, which describes dynamic behavior of the magnetization. Before doing so, we note that the previously discussed structures were obtained on the basis of energy minimization. The static magnetic structure however can also be obtained by determining when the torque exerted by the effective field (2.21) on the magnetization vanishes[4].

### 2.3.1 Landau-Lifshitz-Gilbert equation of motion

We consider a homogenous effective field $\boldsymbol{H}_{\text{eff}}$ exerting a torque $\boldsymbol{\tau}$ on the magnetization $\boldsymbol{M}$:

$$\boldsymbol{\tau} = \frac{d\boldsymbol{L}}{dt} = \boldsymbol{M} \times \boldsymbol{H}_{\text{eff}}, \tag{2.37}$$

where $\boldsymbol{L}$ is the angular momentum associated with the magnetization by

$$\boldsymbol{L} = -\frac{\boldsymbol{M}}{\gamma_0}. \tag{2.38}$$

The proportionality constant is the gyromagnetic ratio, given by $\gamma_0 = \frac{g|e|\mu_0}{2m} = 1.1051g \times 10^5 \ \frac{m}{As}$, where $e$ is the electron charge and $m$ the electron mass. The Landé factor $g$ [101] is 2 when the moment is purely due to the electron spin. In most ferromagnetic materials $g \simeq 2$, indicating that the orbital contribution

[4] For the determination of the ground state of a magnetic sample, the two approaches lead to the same results when the initial configuration is not far from equilibrium. However, for initial configurations, which are far from equilibrium, the dynamic path may differ significantly from the path of direct energy minimization and the dynamic method is then preferable.

to the magnetic moment is negligible [8]. For Fe, $g = 2.1$ in the absence of an external field [102].

The change of the magnetization in time is then related to the torque by

$$\frac{d\boldsymbol{M}}{dt} = -\gamma_0 \boldsymbol{\tau} = -\gamma_0 [\boldsymbol{M} \times \boldsymbol{H}_{\text{eff}}]. \tag{2.39}$$

The magnetization thus precesses about the effective field with a frequency $\omega = \gamma_0 \boldsymbol{H}_{\text{eff}}$, which is of about 17.6 GHz in a one Tesla field.

In addition to this precession, dissipative processes damp the motion of the magnetization. On the atomic scale, these are for example attributable to spin diffusion, spin-orbit coupling, interactions with magnons or phonons or to misaligned atomic spins. To account for these processes within micromagnetic theory, Gilbert [67, 68] introduced a phenomenological damping term, which is subtracted from the effective field:

$$\frac{d\boldsymbol{M}}{dt} = -\gamma_0 \left[ \boldsymbol{M} \times \left( \boldsymbol{H}_{\text{eff}} - \frac{\alpha}{M_s} \frac{d\boldsymbol{M}}{dt} \right) \right]. \tag{2.40}$$

Typically, $\alpha$ is considered constant. The theoretical determination of its exact form is a rather complex problem [103], since it encompasses effects from many different sources.

It can be noted that multiplying the equation above by $\boldsymbol{M}$, the right hand side vanishes, *i.e.* the motion conserves the magnitude of the magnetization $|\boldsymbol{M}| = M_{\text{s}}$:

$$\boldsymbol{M} \frac{d\boldsymbol{M}}{dt} = 0. \tag{2.41}$$

In the form (2.40), the time derivative of the magnetization is present on both sides of the equation. It can however be transformed by replacing $d\boldsymbol{M}/dt$ in the right-hand-side of 2.40 by its own expression, such that

$$\begin{aligned} \frac{d\boldsymbol{M}}{dt} &= -\gamma_0 [\boldsymbol{M} \times \boldsymbol{H}_{\text{eff}}] + \frac{\alpha}{M_s} \left[ \boldsymbol{M} \times \left( -\gamma_0 [\boldsymbol{M} \times \boldsymbol{H}_{\text{eff}}] + \frac{\alpha}{M_s} \left[ \boldsymbol{M} \times \frac{d\boldsymbol{M}}{dt} \right] \right) \right] \\ &= -\gamma_0 [\boldsymbol{M} \times \boldsymbol{H}_{\text{eff}}] - \frac{\alpha\gamma_0}{M_s} \boldsymbol{M} \times [\boldsymbol{M} \times \boldsymbol{H}_{\text{eff}}] + \frac{\alpha^2}{{M_s}^2} \boldsymbol{M} \times \left[ \boldsymbol{M} \times \frac{d\boldsymbol{M}}{dt} \right] \\ &= -\gamma_0 [\boldsymbol{M} \times \boldsymbol{H}_{\text{eff}}] - \frac{\alpha\gamma_0}{M_s} \boldsymbol{M} \times [\boldsymbol{M} \times \boldsymbol{H}_{\text{eff}}] - \alpha^2 \frac{d\boldsymbol{M}}{dt} \end{aligned} \tag{2.42}$$

where the term in $\alpha^2$ was obtained by using (2.41) and the vector identity

$$\boldsymbol{a} \times (\boldsymbol{b} \times \boldsymbol{c}) = (\boldsymbol{a} \cdot \boldsymbol{c})\boldsymbol{b} - (\boldsymbol{a} \cdot \boldsymbol{b})\, \boldsymbol{c}. \tag{2.43}$$

Grouping the terms in $d\boldsymbol{M}/dt$ yields the Landau-Lifshitz-Gilbert (LLG) equation:

$$\frac{d\boldsymbol{M}}{dt} = -\gamma' [\boldsymbol{M} \times \boldsymbol{H}_{\text{eff}}] - \frac{\alpha'}{M_s} \boldsymbol{M} \times [\boldsymbol{M} \times \boldsymbol{H}_{\text{eff}}] \tag{2.44}$$

where $\gamma'$ and $\alpha'$ are defined by:

$$\gamma' = \frac{\gamma_0}{1 + \alpha^2}, \qquad \alpha' = \frac{\alpha\gamma_0}{1 + \alpha^2}. \tag{2.45}$$

It can be noticed that the damping affects both the precessional and the relaxation term, such that the magnitude of the precessional term decreases with increasing damping while the damping term has a maximum for $\alpha = 1$ and exhibits a symmetric behavior on both sides of this maximum. In this context, damping values above $\alpha = 1$ should be considered unphysical. It can be noted that in the limit of infinte damping, $\frac{d\boldsymbol{M}}{dt} \to 0$, as expected [104]. The principal advantage of the LLG form is that it it does not contain any implicit dependence on $\frac{d\boldsymbol{M}}{dt}$ and can hence readily be used for the numeric computation of the magnetization dynamics. For the description of the underlying physics however, the Gilbert form (2.40) is often preferable and the specified values chosen for the damping parameter refer to the Gilbert $\alpha$ throughout the recent litterature.

In analytic problems, it is often convenient to express the Gilbert equation in terms of spherical coordinates $(\theta, \phi)$:

$$\dot{\theta} = -\gamma_0 \, H_{\text{eff},\phi} - \alpha\dot{\phi}\sin\theta \tag{2.46a}$$

$$\dot{\phi}\sin\theta = \gamma_0 \, H_{\text{eff},\theta} + \alpha\dot{\theta} \tag{2.46b}$$

where

$$H_{\text{eff},\phi} = \frac{1}{\mu_0 M_s \sin\theta}\frac{\delta e_{\text{tot}}}{\delta\phi} \tag{2.47a}$$

$$H_{\text{eff},\theta} = \frac{1}{\mu_0 M_s}\frac{\delta e_{\text{tot}}}{\delta\theta} \tag{2.47b}$$

and $e_{\text{tot}}$ is the total energy density. Here, $\theta$ is the polar angle ($\theta = 0$ along the positive $z$ axis) and $\phi$ the azimuth angle in the $xy$ plane, with respect to the $x$ axis.

### 2.3.2 Current-induced dynamics

Classically, moving charges in a ferromagnet induce a magnetic field (Oersted field), which can in turn influence the state of the magnetization. Slonczewski and Berger [51, 52] have predicted that in addition the magnetization can be directly influenced by a spin-polarized electric current. Indeed, as the electrons traverse a magnetic material, they become spin polarized; the spin angular momentum of the conduction electrons is then transferred to the localized magnetization. This spin-transfer torque (STT) mechanism provides a promising new means for the control of the magnetization on the nanoscale.

In this thesis, the effects of spin-polarized currents flowing *in the plane* of the sample are investigated. This particular current geometry is intensively used, in particular in the study of domain wall motion. It has indeed been demonstrated experimentally that under the influence of a sufficiently high spin-polarized current, domain walls can be displaced in the direction of the electron flow, irrespective of the orientation of the domains separating them. This wall displacement has been imaged for example by Yamaguchi *et al.* [54], who have used MFM to measure the position of domain walls in submicron strips following the application of microsecond current pulses. In the same manner, scanning electron microscopy with spin polarization analysis (SEMPA) was used in

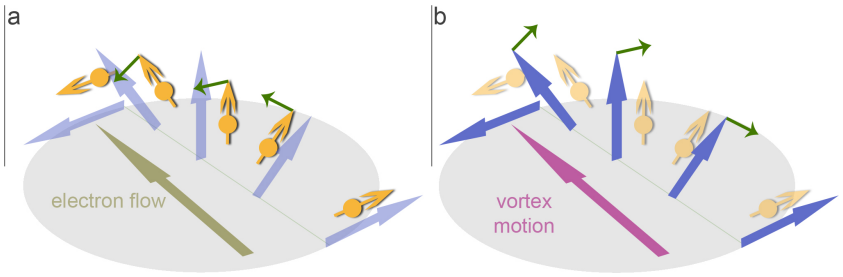


Figure 2.7: Schematic illustration of the adiabatic spin transfer torque effect on a vortex. **a**, The blue arrows represent the orientation of the out of plane magnetization along a cutplane through the vortex core, which has the structure of a Bloch wall. The electron spins are shown in orange and the torque exerted by the magnetization is illustrated by the dark green arrows. **b**, Reaction torque on the magnetization causing the displacement of the vortex.

Refs. [105, 106] to image the displacement of domain walls in nanowires. Time resolved magnetoresistive measurements have been performed in Ref. [107].

The influence of an in-plane current on the dynamics of a magnetization structure such as domain walls [108, 55, 56], can simply be described as follows. As the current flows through a ferromagnet, the local magnetization exerts a torque on the the spins of the conduction electrons, which consequently align with the direction of the magnetization. The spins, in turn, exert a reaction torque on the magnetization, which is proportional to the current density. This torque causes the displacement of the magnetic structure in the direction of the electron flow, as illustrated in Fig. 2.7. Because the dynamics of the electrons is much faster than that of the magnetization, the spins of the conduction electrons generally align with the local magnetization, leading to an adiabatic spin torque. Deviations from this process are also possible, which mainly occur when the electron spins cannot adapt to the local magnetization, for example in narrow inhomogeneous magnetic structures. The origin and exact form of this contribution is currently under debate [108, 109, 110].

To account for the STT effect, two additional terms can be added to the Gilbert equation, which according to Zhang and Li [109], takes the form:

$$\begin{aligned} \frac{d\boldsymbol{M}}{dt} &= -\gamma_0 \left[\boldsymbol{M} \times \boldsymbol{H}_{\text{eff}}\right] - \frac{\alpha}{M_s}\left[\boldsymbol{M} \times \frac{d\boldsymbol{M}}{dt}\right] \\ &\quad -\frac{1}{M_s^2}\, \boldsymbol{M} \times \left[\boldsymbol{M} \times (\boldsymbol{u}\cdot\boldsymbol{\nabla})\boldsymbol{M}\right] \qquad (2.48) \\ &\quad -\frac{\beta}{M_s}\, \mathbf{M} \times (\boldsymbol{u}\cdot\boldsymbol{\nabla})\boldsymbol{M} \qquad (2.49) \end{aligned}$$

The term (2.48) describes the adiabatic spin torque, where $\boldsymbol{u}$ is given by:

$$\boldsymbol{u} = \frac{JPg\mu_B}{2eM_s} \cdot \boldsymbol{j}_{\text{e}}. \qquad (2.50)$$

Here, $J$ is the current density and $\boldsymbol{j}_\mathrm{e}$ is its direction of the electron flow. $P$ is the degree of polarization, $\mu_B$ the Bohr magneton, $g$ the Landé factor and $e$ the electron charge. The expression for $u$ has the units of [m/s], such that it is interpreted as the velocity of the electron spins. The term (2.49) accounts for the non-adiabatic processes and is quantified by the dimensionless parameter $\beta$, also called "degree of non-adiabaticity". Its value has been determined experimentally to be of the order of $\alpha$ for current-induced domain wall motion [107, 111]. Its specific form depends on whether the Gilbert or the LLG form are used [112]. Indeed, if (2.48)and (2.49) are written in the explicit LLG form, the factor $\beta$ is present in both terms [113].

## 2.4 Range of validity of micromagnetic theory

In summary, micromagnetism is a bridge between the quantum mechanical description of magnetism and a macroscopic description involving domains and volume averaged properties of the material. Using micromagnetic theory it is thus possible to describe structures spanning over three orders of magnitude, between the micrometer and the nanometer length scales. It is roughly below one nanometer that concepts such as the magnetization, magnetic charge density or susceptibility start breaking down and atomistic models like the Heisenberg model or quantum mechanical calculations must be used. However, this is only an indicative order of magnitude: whether micromagnetic theory can adequately be used depends on the details of the problem. For example, structures such as monolayers of a ferromagnetic material or atomic chains, even when they extend over a tens of nanometers, cannot be described by micromagnetic theory.

The time scales described by micromagnetic theory extend from a few picoseconds to hundreds of nanoseconds. Indeed using the Landau-Lifshitz-Gilbert equation, processes can only be resolved, which unfold on scales larger than that defined by the gyromagnetic ratio. This amounts to about 5 ps in a one Tesla field. Below this limit, a quantum mechanical description of magnetic processes is necessary, which takes into account phenomena such as spin-lattice, electron-spin or electron-lattice interactions.

In comparison, the ultrafast magnetization dynamics of vortices investigated in this thesis typically occur within tens of picoseconds and their resonant properties unfold on the nanosecond timescale. The lateral extension of the studied vortices are typically of a few of hundred nanometers.

# 3
# Finite-element simulations

Over the past few decades, computer modeling has become an essential and well-established tool – on equal footing with experiments and theory – for the understanding of phenomena in condensed matter physics as well as in a large number of other scientific domains. In magnetism, micromagnetic simulations have significantly contributed to the understanding of static magnetic structures and the dynamics of the magnetization in increasingly complex systems. Until recently, simulations were mostly employed to complement and contribute to the interpretation of experimental data. However, micromagnetic simulations have evolved into an efficient and reliable tool for predicting the behavior of magnetic systems on the nanoscale. In this context, one of the strengths of the simulations lies in the possibility of investigating phenomena, which are beyond the present limits of experimental resolution. In this thesis, they allow accessing the ultrafast dynamics of the nanometric vortex core which unfolds over only a few tens of picoseconds. Presently, the simultaneous access to sufficiently high experimental spatial and temporal resolutions required to image this process still constitutes an experimental challenge. Simulations can equally be used to probe the three-dimensional magnetic configuration in thick samples [34] and its time evolution [35]. In contrast, the experimental observation of static three-dimensional magnetic structures is restricted to only a few experimental techniques, such as X-ray transmission microscopy or Lorentz microscopy. Moreover, simulations provide information on the energy of the studied system, which can explain the occurence of observed static magnetic configurations [42], but is not directly accessible experimentally. In chapter 8, we investigate the core reversal on the basis of the vortex energy, thereby shedding light on the origin of this new micromagnetic process. The rapid evolution of the predictive power of simulations is a result of the development of new theoretical concepts and numeric methods, whose implementation has been made possible by unprecedented increases in computation power.

In order to model micromagnetic problems, continuous systems are discretized into a finite number of elements. Two discretization methods are generally used for solving micromagnetic problems: the finite element and the finite differences method. In the latter, the structure is discretized making use of a rectangular mesh. This regular arrangement of the discretization cells allows

computing the demagnetizing field using the fast Fourier transform method. In the finite-element method (FEM), the problem is discretized into tetrahedral elements and the partial differential equations are reformulated in a so-called weak form [114] in which the unknown and test functions are represented in the basis of linear shape functions (Galerkin method). The problem of solving the partial differential equations is thus effectively converted into solving a large and sparse system of linear equations. While this approach increases the complexity of the algorithm, it allows modeling the boundaries of general sample geometries with high accuracy[1], as illustrated in Fig. 3.1.

We describe in this chapter the formulation of the finite-element micromagnetic algorithm, which was developed by Hertel [40] and used to perform the simulations presented in this thesis. The simulations take as input the material parameters (exchange constant and saturation magnetization), the initial mag-

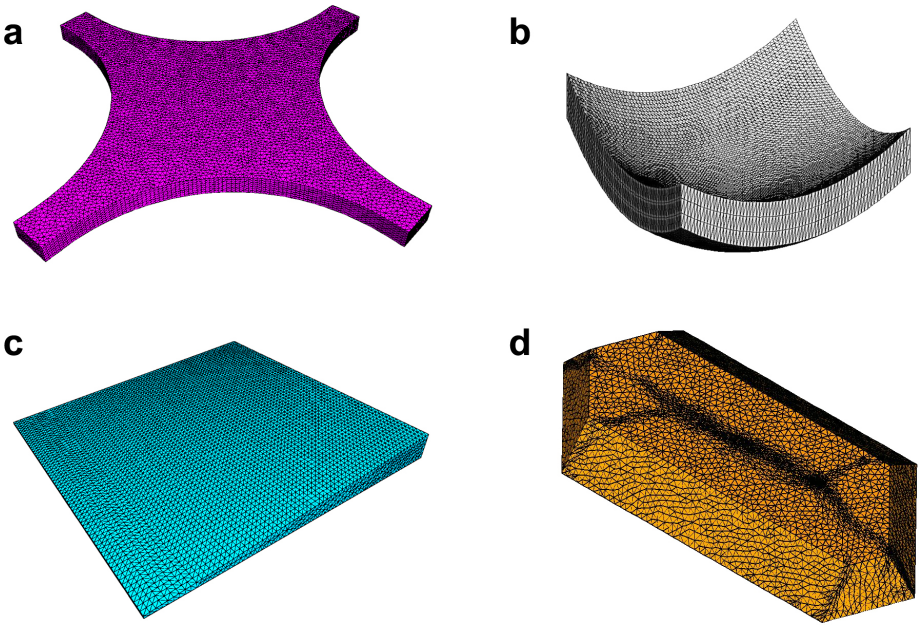


Figure 3.1: Fnite-element meshes for arbitrarily-shaped magnetic nanostructures, illustrating the flexibility of this method. **a**, Sample with curved edges used in chapter 6 to stabilize an isolated antivortex. **b**, Mesh used in Ref. [116] to study the effects of curved surfaces on the magnetic configuration. Figure reprinted with permission from C. Dietrich *at al.*, Phys. Rev. B **77**, 174427 (2008). Copyright (2008) by the American Physical Society. **c**, Non-prismatic sample shapes, such as wedges and the hexagonal nanoisland [34] shown in **d** can be accurately described.

[1]Such geometries would be rather awkward to describe using prismatic elements. The problem of correctly computing the demagnetizing field at the sample boundaries [115] constitutes one of the major drawbacks of the finite differences method in micromagnetics.

netic configuration and external parameters such as applied magnetic fields or electric currents. First, we describe the mesh generation, which results in the subdivision of the magnetic volume into tetrahedral elements of irregular size and shape. The effective field is computed at the vertices of these elements. Second, we detail the computation of the effective fields within the finite-element framework. Third, we describe the time integration of the Landau-Lifshitz-Gilbert equation. Finally, we discuss the influence of a Bloch point on the accuracy of the simulations.

## 3.1 Mesh generation

The first step in the FEM analysis is the definition of the geometry to be simulated and its subdivision into a suitable mesh, which fits the shape of the three-dimensional domain boundaries. The most extensively used scheme for the generation of meshes is the Delaunay triangulation method [117], due to its efficiency and robustness. The method yields unstructured tetrahedral meshes.

The starting point for the mesh generation is the discretization into a set of distinct forming points, which will later become the discretization points [118]. For simplicity, we consider a two-dimensional surface. These points then form a set $P = \{p_i, i = 1, 2, ..., N\}$ on the $\mathbb{R}^2$ plane. A region $V(p_i)$ is defined as the set of points that are closer to $p_i$ than any other point $p_j$:

$$V(p_i) = \{x \in R^2 : ||x - p_i|| \leq ||x - p_j||, i \neq j\} \tag{3.1}$$

where $||...||$ is the Euclidian distance. This is called the Voronoi region [119], and is illustrated in Fig. 3.2a. The points belonging to more than one region form the edges of the regions. As shown in Fig.3.2b, these edges belong to the perpendicular bisectors separating the segment joining the forming points $p_i$ and $p_j$ for contiguous regions $V(p_i)$ and $V(p_j)$.

The Delaunay triangulation of the Voronoi points $P$ consists in connecting the forming points of adjacent Voronoi regions which share a common edge with straight lines. The result is that each Voronoi point is the center of the circumcircle of the Delaunay triangle within which it is located, as shown in Fig. 3.2c. The essential feature of this discretization method is the absence of forming points within any circumcircle. This constitutes the Delaunay criterion used to build the mesh when new points are introduced during the mesh generation. In Fig. 3.2d, for example, an new forming point is inserted, within the circumcircles of three Delaunay triangles. Consequently, the corresponding three Voronoi points are removed along with the triangles as shown in Fig. 3.2e. A new triangulation is then generated based on a newly computed Voronoi diagram.

In practice, the three-dimensional mesh generation starts with the discretization of the edges and surfaces, leading to the computation of the surface elements. Form there, Delaunay triangulation is performed to define the discretization points inside the magnetic volume. The distance between these points is an input parameter, which determines the size of the tetrahedra. As new points

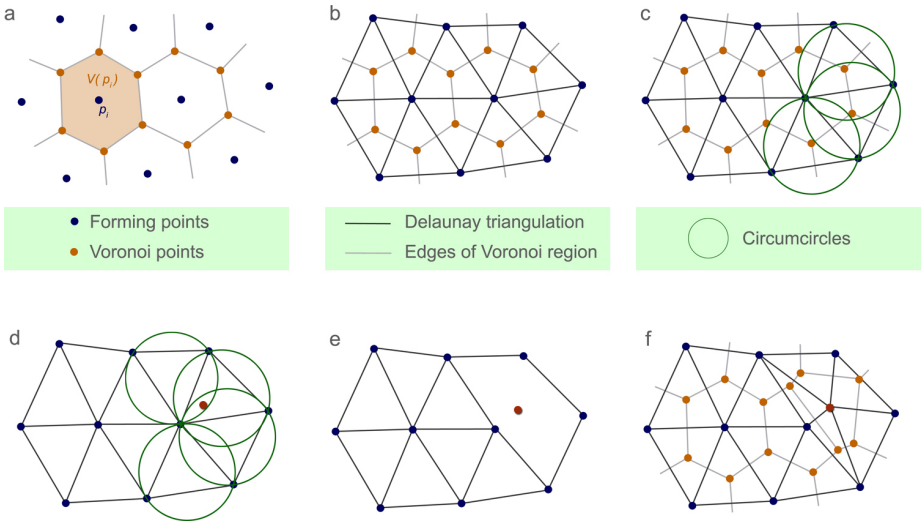


Figure 3.2: Mesh generation using the Delaunay triangulation. **a**, Forming (discretization) points $p_i$ and Voronoi regions $V(p_i)$. The apexes of these regions are called Voronoi points. The Voronoi regions for the forming set P constitute the Voronoi diagram. **b**, Resulting Delaunay triangulation based on the Voronoi diagram. **c**, The Voronoi points are the centers of the circumcircles of the generated triangles. **d**, A forming point is inserted in the mesh, resulting in the removal of the Delaunay triangles, as shown in **e**. A new mesh is constructed following the same principle, as illustrated in **f**.

are added, the Delaunay criterion is checked, allowing to define valid combinations of the contiguous points. The final decomposition of the volume into the tetrahedral mesh must be such that the boundary is represented by the faces of the mesh. Because the construction of the tetrahedra within the volume does not necessarily conform to the faces in the boundary, the surface mesh must be recovered [118].

The meshes used in this thesis are constructed using the TetGen algorithm [120] as implemented in the Gmsh mesh generator [121]. The algorithm uses the Delaunay method generalized to three dimensions.

## 3.2 Finite-element formulation

### 3.2.1 Shape functions

The essence of the finite-element method consists in approximating an unknown function $\boldsymbol{u}(\boldsymbol{x})$ through a piecewise linear approximation $\hat{\boldsymbol{u}}(\boldsymbol{x})$. Each tetrahedral element within the mesh defines a finite element: the discretized values of the unknown function are computed at the vertices (or discretization nodes) $i$ of

each element $e$. Within an element, the approximated function can thus be written as:

$$\begin{aligned} \boldsymbol{u}(\boldsymbol{x}) \simeq \hat{\boldsymbol{u}}(\boldsymbol{x}) &= \sum_{i=1}^{4} \boldsymbol{N}_i^e(\boldsymbol{x})\, \tilde{\boldsymbol{u}}_i^e \\ &= (\boldsymbol{N}_1^e(\boldsymbol{x})\ \boldsymbol{N}_2^e(\boldsymbol{x})\ \boldsymbol{N}_3^e(\boldsymbol{x})\ \boldsymbol{N}_4^e(\boldsymbol{x})) \begin{pmatrix} \tilde{\mathbf{u}}_1^e \\ \tilde{\mathbf{u}}_2^e \\ \tilde{\mathbf{u}}_3^e \\ \tilde{\mathbf{u}}_4^e \end{pmatrix} \\ &= \boldsymbol{N}^e(\boldsymbol{x})\, \tilde{\boldsymbol{u}}^e \end{aligned} \tag{3.2}$$

The row matrix $\boldsymbol{N}^e(\boldsymbol{x})$ is the element shape function matrix. The shape functions $N_i^e$ interpolate the computed function between the nodes of the element. A linear interpolation yields functions of the form:

$$N_i^e(\boldsymbol{x}) = \frac{1}{6V_e}\,(a_i + b_i x + c_i y + d_i z) \tag{3.3}$$

with $\boldsymbol{x}$ the node coordinates and $V_e$ the volume of the tetrahedral element. For each node $i$, the coefficients depend on the shape of the finite element and are normalized such that

$$N_i^e(\boldsymbol{x}_j) = \delta_{ij} = \begin{cases} 1 & \text{if } i = j \\ 0 & \text{if } i \neq j \end{cases} \quad (i, j = 1, ..., 4).$$

Examples of shape functions in one and two dimensions are schematically shown in Fig. 3.3.

For a tetrahedron with apexes $i = 1$ to 4,

$$6V_e = \det \begin{pmatrix} 1 & x_1 & y_1 & z_1 \\ 1 & x_2 & y_2 & z_2 \\ 1 & x_3 & y_3 & z_3 \\ 1 & x_4 & y_4 & z_4 \end{pmatrix}. \tag{3.4}$$

The value of the shape functions at a given point $\boldsymbol{x}$ is computed from the coordinates of each apex and is given within an element $e$ by

$$N_i^e(\boldsymbol{x}) = \frac{1}{6\ V_e} \det \begin{pmatrix} 1 & x & y & z \\ 1 & x_{i+1} & y_{i+1} & z_{i+1} \\ 1 & x_{i+2} & y_{i+2} & z_{i+2} \\ 1 & x_{i+3} & y_{i+3} & z_{i+3} \end{pmatrix}, \tag{3.5}$$

such that the coefficient $b_i$ in (3.3) at a node $i$ for example is:

$$b_i = -\frac{1}{6\ V_e} \det \begin{pmatrix} 1 & y_{i+1} & z_{i+1} \\ 1 & y_{i+2} & z_{i+2} \\ 1 & y_{i+3} & z_{i+3} \end{pmatrix}. \tag{3.6}$$

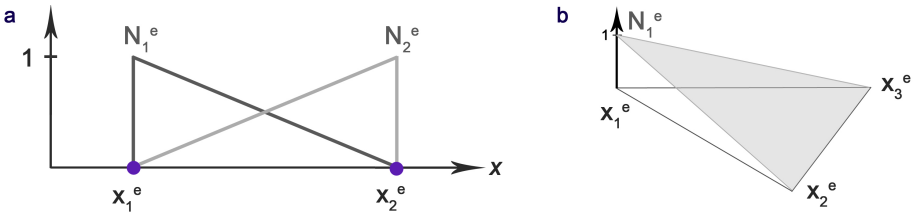


Figure 3.3: Shape functions in one (**a**) and two (**b**) dimensional elements. The sum of the shape functions at every point of the element is always 1.

The three other coefficients are obtained through cyclical permutation. This represents a transformation from Cartesian coordinates to a local coordinate system (barycentric coordinates) in which, as shown by equation (3.5), a weight is assigned to each discretization point based on its surrounding volume.

Higher order interpolation functions can equally be used. For example, quadratic functions were computed in Ref. [122] in order to investigate domain nucleation problems. While these result in a higher numeric accuracy, generally higher interpolation functions are not necessary for the accurate calculation of the magnetization dynamics[2].

The linear shape functions thus provide a basis for the piecewise linear representation of functions within each discretization element. Using this basis, the shape functions are the only space-dependent terms, so that operations applied to the discretized functions, such as differentiation and integration, are performed on the shape functions only. These operations are then converted by means of coefficient comparison into linear algebra problems.

### 3.2.2 Differentiation

Using the shape functions, a partial differentiation *e.g.* $\frac{\partial}{\partial y}$ of the function $\tilde{\boldsymbol{u}}(\boldsymbol{x})$ at a point $\boldsymbol{x}$ within an element $e$ is then simply written as

$$\begin{aligned} \frac{\partial \tilde{\boldsymbol{u}}^e}{\partial y} &= \sum_{i=1}^{4} \tilde{\boldsymbol{u}}_i^e(\boldsymbol{x}) \frac{\partial N_i^e}{\partial y} \\ &= \sum_{i=1}^{4} \tilde{\boldsymbol{u}}_i^e(\boldsymbol{x}) c_i^e \end{aligned} \tag{3.7}$$

where $c_i$ was defined in (3.3).

Generally, it is the gradient of the function which needs to be computed,

[2] Another way of improving the accuracy of a simulation is to adjust the size of the elements. Smaller elements can be used in regions where the function $\tilde{\mathbf{u}}$ changes rapidly. This is illustrated in Fig. 3.1d.

such that (3.7) becomes a matrix multiplication. For each element $e$,

$$\boldsymbol{\nabla}\tilde{\mathbf{u}}^e(\boldsymbol{x}) = \begin{pmatrix} b_1^e & c_1^e & d_1^e \\ b_2^e & c_2^e & d_2^e \\ b_3^e & c_3^e & d_3^e \\ b_4^e & c_4^e & d_4^e \end{pmatrix} \begin{pmatrix} u_x^e \\ u_y^e \\ u_z^e \end{pmatrix} = \underline{\underline{\boldsymbol{B}}}^e \tilde{\boldsymbol{u}}^e(\boldsymbol{x}). \tag{3.8}$$

In the micromagnetic code, the matrices $\underline{\underline{\boldsymbol{B}}}^e$ are initially calculated and stored during a preprocessing step and are used in the main program every time an operation is performed.

### 3.2.3 Integration

Like the differentiation, integration is performed on the shape functions. For a finite element of volume $V_e$,

$$\int_{V_e} \tilde{u}^e(\boldsymbol{x})\, dV = \int_{V_e} \sum_{i=1}^{4} \tilde{u}^e(\boldsymbol{x}) N_i^e(\boldsymbol{x})\, dV = \sum_{i=1}^{4} \tilde{u}^e(\boldsymbol{x})\, V_e \int_{V_e} \frac{N_i^e(\boldsymbol{x})}{V_e}\, dV. \tag{3.9}$$

The normalized integral $\int (N^n/V_e) dV = \frac{1}{4}$ within the tetrahedral element independent of its shape and represents the fraction of the total volume associated to each node. The integral (3.9) then takes the form

$$\int_{V_e} \tilde{u}(\boldsymbol{x})\, dV = \frac{1}{4} V_e \sum_{i=1}^{4} u_i(\boldsymbol{x}), \tag{3.10}$$

where expression (3.4) for the element volume is used.

A characteristic integral results from the computation of second order derivatives, which yield a $4 \times 4$ stiffness matrix $\underline{\underline{\boldsymbol{K}}}^e$ with components

$$K_{ij}^e = \int_{V_e} \boldsymbol{\nabla} N_i^e \boldsymbol{\nabla} N_j^e\, dV = \sum_{\alpha}^{x,y,z} c_{i\alpha}^e c_{j\alpha}^e\, V_e \tag{3.11}$$

where $i = 1, ..., 4$ and $j = 1, ..., 4$. The terms $c_{i\alpha}^n$ correspond to the components of the matrix $\underline{\underline{\boldsymbol{B}}}^e$ in equation (3.8), with $\alpha = x, y, z$.

Another often-encountered integral is the mass matrix $\underline{\underline{\boldsymbol{M}}}^e$ whose components can be evaluated analytically [123]:

$$M_{ij}^e = \int_{V_e} N_i N_j\, dV = \frac{1}{5}(a + \delta_{ij}) V_e. \tag{3.12}$$

These matrices are also computed during the preprocessing step.

## 3.3 Computation of the effective fields

The effective field is computed at each discretization node from the total energy following equation (2.19):

$$\boldsymbol{H}_{\text{eff}} = -\frac{1}{\mu_0 M_s}\frac{\partial e}{\partial \boldsymbol{m}}. \tag{3.13}$$

In the next sections we describe this computation detailed in Ref. [40].

### 3.3.1 Weak formulation and the exchange field

According to equation (2.21), the exchange field is given by:

$$\boldsymbol{H}_{\text{exc}} = \frac{2A}{\mu_0 M_s}\nabla^2 \boldsymbol{m}. \tag{3.14}$$

In addition, at the surface $\partial S$ of the magnetic body, the exchange field is determined by the Rado-Wertmann boundary conditions [124]:

$$\left.\frac{\partial \boldsymbol{m}}{\partial \boldsymbol{n}}\right|_{\partial S} = \mathbf{0}. \tag{3.15}$$

The partial differential equation (3.14) is first converted into an equivalent "weak form" by multiplying each side by an arbitrary test function $u$ and integrating over the magnetic volume:

$$\int_V \boldsymbol{u}^T \boldsymbol{H}_{\text{exc}}\, dV = \int_V \frac{2A}{\mu_0 M_s}\boldsymbol{u}^T \left(\nabla^2 \boldsymbol{m}\right) dV. \tag{3.16}$$

The vector $\mathbf{u}$ is composed of three arbitrary test functions $u(x)$, $u(y)$ and $u(z)$. Equation (3.16) is equivalent to (3.14) provided that the equality holds for *any* vector $\boldsymbol{u}$.

Integrating by parts (3.16) yields:

$$\int_V \mathbf{u}^T \boldsymbol{H}_{\text{exc}}\, dV = -\frac{2A}{\mu_0 M_s}\int_V \left(\boldsymbol{\nabla}\mathbf{u}\right)^T \boldsymbol{\nabla}\boldsymbol{m}\, dV + \frac{2A}{\mu_0 M_s}\int_{\partial S} \boldsymbol{u}^T \boldsymbol{\nabla}\boldsymbol{m}\, dS \tag{3.17}$$

and given the boundary conditions (3.15),

$$\int_V \boldsymbol{u}^T \boldsymbol{H}_{\text{exc}}\, dV = -\frac{2A}{\mu_0 M_s}\int_V \left(\boldsymbol{\nabla}\boldsymbol{u}\right)^T \boldsymbol{\nabla}\boldsymbol{m}\, dV. \tag{3.18}$$

The weak formulation therefore transformed the second order derivative in (3.14) into a first-order derivative.

The volume integration is converted into a sum over the total number $\mathcal{N}$ of finite elements. Considering only the $x$ component of the effective field for simplicity,

$$\sum_{e=1}^{\mathcal{N}} \int_{V_e} u_x H_{\mathrm{exc},x}\, dV = -\frac{2A}{\mu_0 M_s} \sum_{e=1}^{\mathcal{N}} \int_{V_e} \boldsymbol{\nabla} u_x \boldsymbol{\nabla} m_x\, dV \tag{3.19}$$

where the integration is now preformed over the volume of the individual elements.

Using (3.3), the quantities $u_x$, $m_x$ and $H_{\mathrm{exc},x}$ can be expanded within the basis of the shape functions within each element $e$:

$$\begin{cases} u_x^e(\boldsymbol{x}) \simeq \sum_{i=1}^{4} u_x^i N_i^e(\boldsymbol{x}) \\ m_x^e(\boldsymbol{x}) \simeq \sum_{j=1}^{4} m_x^j N_j^e(\boldsymbol{x}) \\ H_{\mathrm{exc},x}^e(\boldsymbol{x}) \simeq \sum_{l=1}^{4} h_l N_l^e(\boldsymbol{x}) \end{cases} \tag{3.20}$$

Equation (3.19) is then written as:

$$\sum_{e=1}^{\mathcal{N}} \sum_{i=1}^{4} \sum_{l=1}^{4} u_x^i h_x^l \int_{V_e} N_i^e N_l^e\, dV = -\frac{2A}{\mu_0 M_s} \sum_{e=1}^{\mathcal{N}} \sum_{i=1}^{4} \sum_{j=1}^{4} u_x^i m_x^j \int_{V_e} \boldsymbol{\nabla} N_i^e \boldsymbol{\nabla} N_j^e\, dV. \tag{3.21}$$

Since this equation must hold for any value set $u^i$ of the arbitrary test functions, it can be solved by comparing the coefficients of each test function $u_x^i$ on both sides of the equation. This comparison converts equation (3.21) into a system of four linear equations within each element. The stiffness matrix (3.11), which appears on the right-hand-side however is not diagonal and requires solving the full system of linear equations. In order to increase the calculation speed, a mass-lumping technique is used which allows diagonalizing this matrix [40, 118]. This approximation assigns a homogenous exchange field within each element and yields $\underline{\underline{\boldsymbol{K}}}_{ij}^e = \frac{V_e}{4}$ for the stiffness matrix. This holds very well for sufficiently small cell sizes [40].

The expression of the exchange field $h^l$ at each node $l$ in equation (3.21) is thus:

$$h_x^l = -\frac{2A}{\mu_0 M_s} \frac{4}{\sum_{e=1}^{k} V_e} \sum_{e=1}^{k} \left( \sum_{\alpha}^{x,y,z} c_{i\alpha}^n c_{j\alpha}^n \right) m_x^j V_e. \tag{3.22}$$

In the above equation, $V_e$ is the volume of the element $e$ containing the node $i$, while $\sum_{e=1}^{k} V_e/4$ is the volume associated to the node $i$, computed over all $k$ elements containing this node (which are part of its Voronoi cell). In compact

form, this can be written as the matrix multiplication:

$$h_\alpha^i = \underline{\underline{\boldsymbol{A}}}_{ij} \cdot m_\alpha^j \tag{3.23}$$

for each component $\alpha = x, y, z$ with:

$$\underline{\underline{\boldsymbol{A}}}_{ij} = -\frac{2A}{\mu_0 M_s} \frac{4}{\left(\sum_{e=1}^{k} V_e\right)} \sum_{e=1}^{k} \left( \sum_{\alpha}^{x,y,z} c_{i\alpha}^e c_{j\alpha}^e \right) V_e. \tag{3.24}$$

The matrix $\underline{\underline{\boldsymbol{A}}}$ is sparse, and can thus be stored in a compact way.

### 3.3.2 Anisotropy

Considering a second-order uniaxial anisotropy, from equations (2.14) and (3.13):

$$\boldsymbol{H}_{\text{an}}^i = -\frac{2K_u}{\mu_0 M_s} \cdot \hat{\boldsymbol{k}}_u^i \cdot (\boldsymbol{m}^i \cdot \hat{\boldsymbol{k}}_u^i) \tag{3.25}$$

where $\hat{\boldsymbol{k}}_u^i$ is the unit vector along the easy axis at each node $i$, whose direction is provided as an input to the simulations. The dot products are computed at each node considering the volume associated with the node, such that:

$$\hat{\boldsymbol{k}}_u^i = \frac{K_u}{\sum_{e=1}^{k} V_e} \left( \hat{\boldsymbol{x}} + \hat{\boldsymbol{y}} + \hat{\boldsymbol{z}} \right). \tag{3.26}$$

In the micromagnetic code, uniaxial (up to second order), cubic and surface anisotropies are computed.

### 3.3.3 Magnetostatic field

The calculation of the magnetostatic field is performed using potential theory. Following section 2.1.2, the magnetostatic field is obtained from a scalar potential $U$:

$$\boldsymbol{H}_{\text{dem}} = -\boldsymbol{\nabla} U. \tag{3.27}$$

Inside the volume, following equation (2.8),

$$\nabla^2 U = -\boldsymbol{\nabla} \cdot \boldsymbol{M} \tag{3.28}$$

while outside the volume,

$$\nabla^2 U = 0. \tag{3.29}$$

At the boundary, the following conditions must be satisfied:

$$U^{\text{in}} = U^{\text{out}} \tag{3.30}$$

$$\left(\boldsymbol{\nabla} U^{\text{in}} - \boldsymbol{\nabla} U^{\text{out}}\right) \cdot \boldsymbol{n} = \boldsymbol{M} \cdot \boldsymbol{n}. \tag{3.31}$$

In addition, the magnetic potential must vanish at infinity:

$$\lim_{x \to \infty} U(\boldsymbol{r}) = 0 \tag{3.32}$$

such that the computation of the demagnetizing field is an open boundary problem. To this effect, a hybrid finite element/boundary element method was developed by Fredkin and Koehler [125, 126], which does not require considering any nodes outside the magnetic volume.

The method consists in splitting the potential in two parts $U = U_1 + U_2$. Inside the volume, $U_1$ is given by

$$\nabla^2 U_1 \quad = \quad -\nabla \cdot \boldsymbol{M}. \tag{3.33}$$

while outside,

$$U_1 \quad = \quad 0. \tag{3.34}$$

Hence, at the volume boundary the condition (3.30) becomes:

$$U_2^{\text{out}} - U_2^{\text{in}} = U_1^{\text{in}}. \tag{3.35}$$

and the condition (3.31) yields:

$$\boldsymbol{\nabla} U_1^{\text{in}} \cdot \boldsymbol{n} \quad = \quad \boldsymbol{M} \cdot \boldsymbol{n}. \tag{3.36}$$

To solve for the demagnetizing potential inside the volume, equation 3.33 is written in the weak form using a test function $v$:

$$\int_V v \boldsymbol{\nabla}^2 U_1 \, dV = \int_V v \boldsymbol{\nabla} \boldsymbol{M} \, dV. \tag{3.37}$$

Integration by parts yields,

$$\int_V \boldsymbol{\nabla} v \cdot \boldsymbol{\nabla} U_1 \, dV - \int_{\partial S} v(\boldsymbol{\nabla} U_1 - \boldsymbol{M}) \, dS = \int_V \boldsymbol{\nabla} v \cdot \boldsymbol{M} \, dV. \tag{3.38}$$

Using the Neumann boundary condition (3.36), we obtain

$$\int_V \boldsymbol{\nabla} v \cdot \boldsymbol{\nabla} U_1 \, dV = \int_V \boldsymbol{\nabla} v \cdot \boldsymbol{M} \, dV. \tag{3.39}$$

This expression is computed by expanding its terms in the local basis defined by the shape functions, as described in section 3.3.1. The calculation involves the stiffness matrix on the left-hand side, while the matrix $\frac{V_n}{4} \underline{\underline{\boldsymbol{B}}}^e$ is used on the right-hand side.

Considering the second part of the potential,

$$\nabla^2 U_2 = 0 \tag{3.40}$$

where $U_2$ is generally non-zero over all space. In order to account for the jump condition (3.31) of the total potential, $U_2$ must obey the boundary conditions

$$\boldsymbol{\nabla} U_2^{\text{in}} \cdot \boldsymbol{n} = \boldsymbol{\nabla} U_2^{\text{out}} \cdot \boldsymbol{n} \tag{3.41}$$

and it is required that $U_2 \to 0$ for $\boldsymbol{x} \to \pm\infty$. The behavior of the potentials $U_1$ and $U_2$ at the boundary are shown in Fig. 3.4.

According to potential theory, $U_2$ can be expressed in terms of the values of $U_1$ at the boundary:

$$U_2(\boldsymbol{x}) = \frac{1}{4\pi} \int_{\partial S} U_1(\boldsymbol{x'}) \frac{\partial G(\boldsymbol{x}, \boldsymbol{x'})}{\partial \boldsymbol{n}(\boldsymbol{x'})} \, dS \tag{3.42}$$

where $G(\boldsymbol{x}, \boldsymbol{x'}) = 1/|\boldsymbol{x} - \boldsymbol{x'}|$ is Green's function.

The integral (3.42) holds for every point $\boldsymbol{x}$ within the magnetic body. The integration at each discretization point is however computationally expensive. Instead, the expression can be evaluated only at the sample boundary, yielding Dirichlet boundary conditions that allow to solve (3.40) within the magnetic volume. Approaching the boundary from inside the volume, $U_2$ is expressed by [125]:

$$U_2(\boldsymbol{x}) = \frac{1}{4\pi} \int_{\partial S} U_1(\boldsymbol{x'}) \frac{\partial G(\boldsymbol{x}, \boldsymbol{x'})}{\partial \boldsymbol{n}(\boldsymbol{x'})} \, dS + \left( \frac{\Omega(\boldsymbol{x})}{4\pi} - 1 \right) U_1(\boldsymbol{x}), \tag{3.43}$$

where $\Omega(\boldsymbol{x})$ is the solid angle subtended by the surface at the point $\boldsymbol{x}$.

The values of $U_2$ can thus be obtained form the values of $U_1$, through integration over the sample surface. The discretization of the potentials $U_1$ and $U_2$ transforms the above integral into a matrix multiplication:

$$U_2^i = D_{ij} U_1^j. \tag{3.44}$$

The integration of the Green's function was performed by Lindholm in Ref. [127]. The Laplace equation for $U_2$ is then solved within the sample using the finite-element method.

The matrix $\underline{\underline{\boldsymbol{D}}}$ is dense in the sense that it is mostly populated. An increase

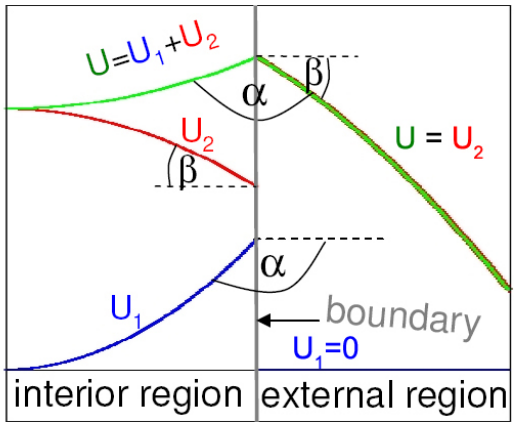


Figure 3.4: Schematic representation of the splitting of the demagnetizing potential $U = U_1 + U_2$ and the behavior of each part at the sample boundary. The gradient of $U_1$ given by equation (3.36) corresponds to the angle $\alpha$. Outside the magnetic volume, $U_1 = 0$. The gradient of $U_2$ given by the angle $\beta$ is constant along the boundary. (Adapted from from Ref. [128].)

in the number of boundary nodes therefore leads to a quadratic increase in the memory size required to store the matrix. Typically this defines the limiting size of the micromagnetic problems which can be considered. However, matrix compression methods have been developed, which allow to reduce the size of such dense matrices without noticeable loss of accuracy. A very efficient method involves hierarchical matrices [129]. The boundary matrix $\underline{\underline{\boldsymbol{D}}}$ usually does not have any particular internal structure. The compression is achieved through the computation and arrangement of this boundary matrix in blocks, which represent the interaction between clusters of boundary nodes. Between clusters that are far apart, the interaction is weaker and the matrix $\underline{\underline{\boldsymbol{D}}}$ of rank $kl$ can be decomposed into lower-rank matrices:

$$\underline{\underline{\boldsymbol{D}}}_{kl} = \underline{\underline{\boldsymbol{P}}}_{ks}\underline{\underline{\boldsymbol{Q}}}_{sl} \tag{3.45}$$

where $s$ is much smaller than $k$ or $l$. The memory required for the storage of these matrices is thus of the order $s(k+l)$, rather then $kl$ [130]. In practice, this allows reducing problems that would require a few TB of memory to a few tens of GB. The multiplication of such small matrices equally saves CPU time, compared to vector-matrix multiplications involving very large, dense matrices.

## 3.4 Integration of the equation of motion

Based on the effective field obtained at each node, the time evolution of the magnetization can be computed. The time integration of the Landau-Lifshitz-Gilbert equation, based on a discretized magnetization distribution at a time $t$ thus yields the distribution at a later time $t + \Delta t$. The simplest numeric integration method is the Euler method, where the magnetization at time $t+\Delta t$ is computed based on a single previous value. Explicit methods are however generally not stable and implicit schemes have to be used. Here, the Adams-Moulton predictor-corrector method provided by the CVODE solver [131] is used. At each node, the set of linear equations is solved by functional iteration. In the micromagnetic code, the step size $\Delta t$ is chosen as a function of the value of the torque $\boldsymbol{m} \times \boldsymbol{H}_{\text{eff}}$: it is on the femtosecond time scale, ranging between a few fs to about one hundred fs and decreases for large amplitude precessions of the magnetization. This step size is passed to the ODE solver, where an internal time step is defined.

The steps performed by the micromagnetic code to calculate the magnetization dynamics are shown in Fig 3.5.

## 3.5 Effect of a singularity

The discretization into tetrahedral elements is typically performed such that the distance between neighboring nodes is below the exchange length. However, when a Bloch point (introduced in the previous chapter, section 2.2.4) is present in a static configuration or a dynamic process, the magnetization becomes highly

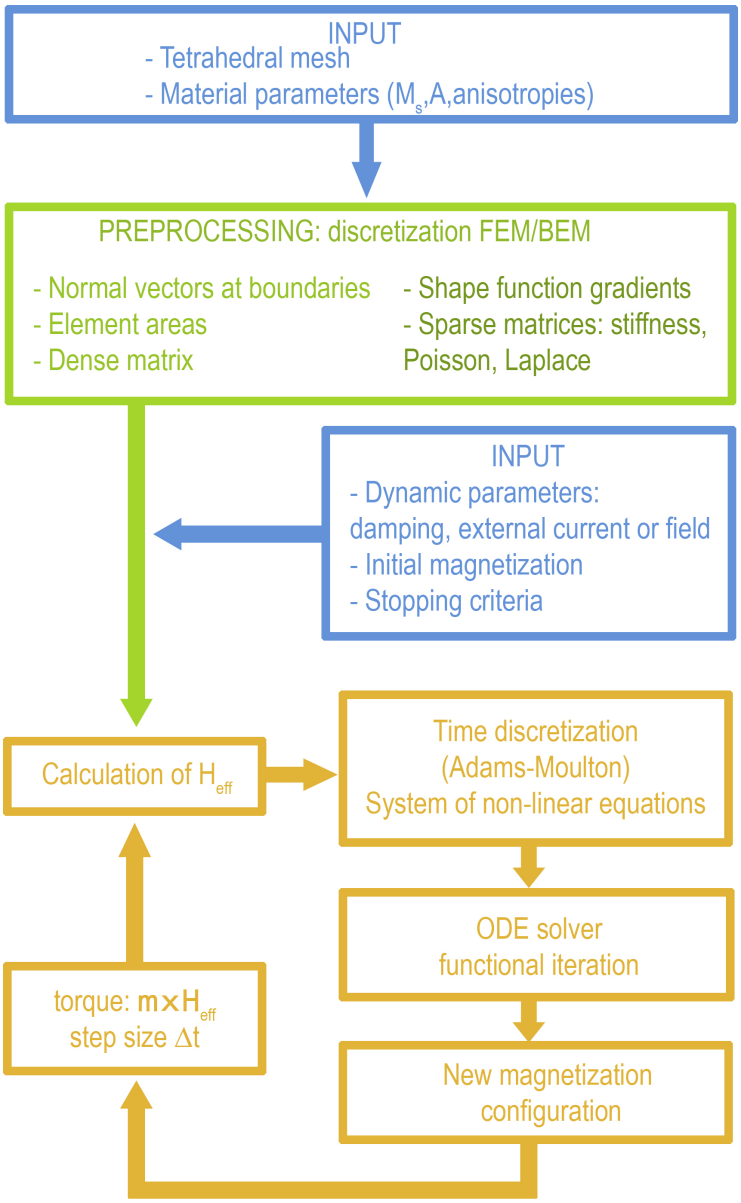


Figure 3.5: Schematic representation of the computational steps performed by the finite-element micromagnetic code.

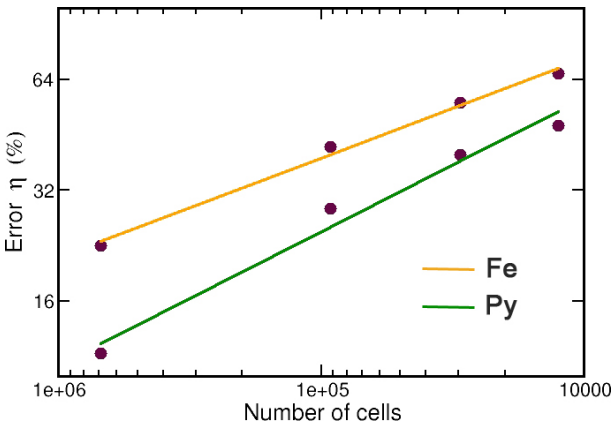


Figure 3.6: Error on the computed exchange energy of the vortex during the core reversal in the presence of a Bloch point as a function of the number of discretization elements for two different materials. The solid lines are exponential fits to the data following expression (3.47).

inhomogeneous below the exchange length. While the Bloch point itself cannot be treated within the framework of micromagnetic theory[3], it has been shown that the behavior of the magnetization around the Bloch point can reliably be described using micromagnetic simulations [28, 46]. Indeed, on a spherical shell around the singularity, the magnetization behaves smoothly.

The influence of a singularity on the accuracy of finite-element simulations has been studied mostly in engineering problems [118]. The error in such cases was found to be an exponential function of the number of discretization nodes $\mathcal{N}$ used in the computation. The error $\eta$ can be defined as:

$$\eta = \frac{||\boldsymbol{u} - \hat{\boldsymbol{u}}||}{||\boldsymbol{u}||} \times 100\%, \tag{3.46}$$

where $\boldsymbol{u}$ is an exact analytic function and $\hat{\boldsymbol{u}}$ its computed approximation. The rate of convergence for problems with a singularity is then:

$$\mathcal{O}(\mathcal{N})^{-\kappa} \tag{3.47}$$

where $\kappa$ depends on the problem parameters. In chapter 8, we show that the exchange energy of the vortex at the moment of the core reversal strongly depends on the discretization cell size and similarly exhibits an exponential behavior, due to the presence of a Bloch point. The error on the numerically calculated energy as a function of the number of discretization cells used in the computation is shown in Fig. 3.6, based on the results of chapter 8. There, we also show that the exponent $\kappa$ is a function of the exchange length of the material.

In the simulations performed in this thesis, we consequently use cell sizes well below the exchange length in order to accurately resolve the details of the magnetization dynamics.

[3] To accurately describe the Bloch point itself, the micromagnetic simulations should be combined with electronic structure (ab-initio) calculations or atomistic studies.

# 4
# Vortex dynamics

Magnetism on the nanoscale displays rich and complex dynamics. A detailed understanding of these dynamics has been achieved over the past decades owing to close interplay between experiments, theory and simulations. In particular, the switching of the magnetization has been intensely investigated in ferromagnetic nanoelements [24, 132, 30, 31] along with their excitation modes [133, 22, 134, 135]. In this context, magnetic vortices are particularly interesting owing to their distinctive dynamics, characterized by the gyration of the vortex core [23, 22, 136, 137].

In this chapter, we give an overview of vortex dynamics, mainly focusing on field-induced dynamics. In the most general case, the behavior of a micromagnetic structure in an external field can be derived by determining an analytic expression for its energy. From the total energy, the effective field can be obtained and the Landau-Lifshitz-Gilbert equation integrated to describe the resulting motion. In practice however, the expression for the different energy terms has to be derived for each considered case. To simplify such calculations, Thiele has expressed the Landau-Lifshitz-Gilbert equation in terms of generalized forces acting on the magnetic structure [19]. Assuming that the shape of the structure does not change during the displacement, this approach allows solving dynamic micromagnetic problems without the need to explicitly compute the energy of the system or to integrate the differential equations to obtain the time dependence of the magnetization. The approach was applied to magnetic vortices by Huber [20, 138], thus greatly simplifying the computation of their dynamics. We therefore start by deriving the Thiele equation and the predicted vortex dynamics. We then present the most important experimental observations of the vortex gyrotropic excitation, which have been essential in confirming the theoretical predictions. These experiments have mostly taken place within the past decade as a result of dramatic increases in experimental resolution [5].

Finally, we show that in parallel to theory and experiments, micromagnetic simulations have equally provided essential insight into vortex dynamics, for example by revealing processes, which occur on time and length scales below present experimental resolution. One such example is the strong distortion for the vortex core during its motion. Very recently, simulations have also predicted

new, unexpected dynamic processes such as the annihilation of vortex-antivortex pairs in zero field. These therefore offer insight into magnetization dynamics occurring below the exchange length.

## 4.1 Steady state dynamics

### 4.1.1 The Thiele equation

In contrast to the Landau-Lifshitz-Gilbert equation in which the calculation of the magnetization dynamics is based on the effective field, the Thiele equation describes the dynamics in terms of *forces* acting on an arbitrary spin distribution [19]. To this effect, the following assumptions are made:

1. The considered system is at equilibrium, *i.e.* moves with constant velocity;
2. The shape of the magnetic structure remains unchanged during the motion.

The latter assumption if fact holds well for small amplitude displacements.

In the following, we derive the Thiele equation for a general micromagnetic structure and apply it to the vortex. The derivation based on Refs. [8, 100]. First, a localized magnetization distribution $\boldsymbol{M}(\boldsymbol{x}-\boldsymbol{X})$ is considered, where $\boldsymbol{X}$ is the coordinate of the center of mass of the system and $\boldsymbol{x}$ a position vector. In spherical coordinates, considering that $M$ is constant, the distribution $\boldsymbol{M}$ is defined by its angular dependence on $\theta$ and $\phi$, the polar and azimuthal angles of the magnetization, defined like in chapter 2 such that $\theta = \pi/2$ is in the sample plane:

$$\theta(\boldsymbol{x}-\boldsymbol{X}), \quad \phi(\boldsymbol{x}-\boldsymbol{X}). \tag{4.1}$$

Under the influence of an external field, the magnetic distribution is displaced from its equilibrium position and the force $\boldsymbol{F}_{\text{ext}}$ acting on it can be obtained from the gradient of the total energy $E$ of the system, $\boldsymbol{F}_{\text{ext}} = -\boldsymbol{\nabla} E$. The total energy can be expressed as an integral of the local energy density $e$ over the entire magnetic volume, such that a small variation in energy due to the external force is

$$\delta E = \int \delta e \, dV, \tag{4.2}$$

where $\delta e(\boldsymbol{x}-\boldsymbol{X})$ is the variation in local energy density. Consequently, variations in $\boldsymbol{F}_{\text{ext}}$ can be expressed in terms of the local force density $\boldsymbol{f}_{\text{ext}}$:

$$\begin{aligned} \delta \boldsymbol{F}_{\text{ext}} &= \int (-\boldsymbol{\nabla}_{\boldsymbol{X}} \delta e) \, dV \\ &= \int (\boldsymbol{\nabla}_{\boldsymbol{x}} \delta e) \, dV \\ &= \int \boldsymbol{f}_{\text{ext}} \, dV. \end{aligned} \tag{4.3}$$

Here, the variation in energy density $\delta e$ is a function of the position and a functional of the magnetization $\boldsymbol{M}$. It therefore also exhibits a dependence on $\theta$ and $\phi$. Thus, from equation (4.3) the expression for $\boldsymbol{f}_{\text{ext}}$ can be obtained through chain differentiation:

$$\boldsymbol{f}_{\text{ext}} = \frac{\delta e}{\delta \theta}\, \boldsymbol{\nabla}_{\boldsymbol{x}} \theta + \frac{\delta e}{\delta \phi}\, \boldsymbol{\nabla}_{\boldsymbol{x}} \phi. \tag{4.4}$$

Thiele interpreted the right-hand-side of the above equation as the expression of an internal restoring force $\boldsymbol{f}_{\text{int}}$ that counters the applied force. This internal force is a result of the contributions from the exchange, anisotropy and demagnetizing energies. Equation (4.4) can then be written as:

$$\boldsymbol{f}_{\text{ext}} + \boldsymbol{f}_{\text{int}} = 0. \tag{4.5}$$

In the presence of the external force[1], the magnetization dynamics is described by the Landau-Lifshitz-Gilbert equation. In spherical coordinates, its form is given by (2.46):

$$\dot{\theta} = -\frac{\gamma_0}{\mu_0 M_s}\left(\frac{1}{\sin\theta}\frac{\delta e}{\delta \phi}\right) - \alpha \sin\theta \dot{\phi} \tag{2.46a}$$

$$\sin\theta \dot{\phi} = \frac{\gamma_0}{\mu_0 M_s}\frac{\delta e}{\delta \theta} + \alpha \dot{\theta} \tag{2.46b}$$

The expression for the angular dependence of the energy density is therefore:

$$\frac{\delta e}{\delta \theta} = \frac{\mu_0 M_s}{\gamma_0}\left(\dot{\phi}\sin\theta - \alpha\dot{\theta}\right) \tag{4.6a}$$

$$\frac{\delta e}{\delta \phi} = -\frac{\mu_0 M_s}{\gamma_0}\left(\dot{\theta}\sin\theta + \alpha\dot{\phi}\sin^2\theta\right). \tag{4.6b}$$

From equations (4.4) and (4.6), the expression for the restoring force can now be written explicitly:

$$\boldsymbol{f}_{\text{int}} = \frac{\mu_0 M_s}{\gamma_0}\left[\left(-\dot{\phi}\sin\theta + \alpha\dot{\theta}\right)\boldsymbol{\nabla}\theta + \left(\dot{\theta}\sin\theta + \alpha\dot{\phi}\sin^2\theta\right)\boldsymbol{\nabla}\phi\right], \tag{4.7}$$

where the gradient is taken with respect to the field position variable: $\boldsymbol{\nabla} \equiv \boldsymbol{\nabla}_{\boldsymbol{x}}$. For steady-state motion with velocity $\boldsymbol{v}$, the position of the magnetic distribution is given by $\boldsymbol{X} = \boldsymbol{v}t$. Then, according to (4.1),

$$\theta = \theta(\boldsymbol{x} - \boldsymbol{v}t) \qquad \phi = \phi(\boldsymbol{x} - \boldsymbol{v}t), \tag{4.8}$$

and a Taylor expansion yields

$$\dot{\theta} = -\boldsymbol{v}\cdot\boldsymbol{\nabla}\theta \qquad \text{and} \qquad \dot{\phi} = -\boldsymbol{v}\cdot\boldsymbol{\nabla}\phi. \tag{4.9}$$

[1] The form of various external forces is detailed in section 4.1.3.

Equation (4.7) can be thus written in terms of the velocity $\boldsymbol{v}$:

$$\boldsymbol{f}_{\text{int}} = \frac{\mu_0 M_s}{\gamma_0} \left[ \boldsymbol{v}\ \boldsymbol{\nabla}\phi\ \sin\theta\ \boldsymbol{\nabla}\theta - \alpha \boldsymbol{v}\ \boldsymbol{\nabla}\theta\ \boldsymbol{\nabla}\theta - \boldsymbol{v} \sin\theta\ \boldsymbol{\nabla}\theta\ \boldsymbol{\nabla}\phi - \alpha \boldsymbol{v} \sin^2\theta\ \boldsymbol{\nabla}\phi\ \boldsymbol{\nabla}\phi \right] \tag{4.10}$$

or alternatively, grouping the terms in $\alpha$:

$$\boldsymbol{f}_{\text{int}} = \frac{\mu_0 M_s}{\gamma_0} \left[ (\boldsymbol{v}\ \boldsymbol{\nabla}\phi\ \sin\theta\ \boldsymbol{\nabla}\theta - \boldsymbol{v} \sin\theta\ \boldsymbol{\nabla}\theta\ \boldsymbol{\nabla}\phi) - \boldsymbol{v} \cdot \alpha \left( \boldsymbol{\nabla}\theta\ \boldsymbol{\nabla}\theta + \sin^2\theta\ \boldsymbol{\nabla}\phi\ \boldsymbol{\nabla}\phi \right) \right] \tag{4.11}$$

The first term can be written more succinctly as the cross product $\boldsymbol{v} \times (\sin\theta\ \boldsymbol{\nabla}\theta \times \boldsymbol{\nabla}\phi)$ by making use of the vector identity $(\boldsymbol{a} \cdot \boldsymbol{c})\boldsymbol{b} - (\boldsymbol{a} \cdot \boldsymbol{b})\boldsymbol{c} = \boldsymbol{a} \times (\boldsymbol{b} \times \boldsymbol{c})$. We now define

$$\boldsymbol{g} = -\frac{\mu_0 M_s}{\gamma_0} (\sin\theta\ \boldsymbol{\nabla}\theta \times \boldsymbol{\nabla}\phi) \tag{4.12}$$

and

$$\underline{\underline{\boldsymbol{d}}} = -\frac{\mu_0 M_s}{\gamma_0} \left( \boldsymbol{\nabla}\theta\ \boldsymbol{\nabla}\theta + \sin^2\theta\ \boldsymbol{\nabla}\phi\ \boldsymbol{\nabla}\phi \right), \tag{4.13}$$

such that equation (4.11) becomes:

$$\boldsymbol{f}_{\text{int}} = \boldsymbol{g} \times \boldsymbol{v} + \alpha\ \underline{\underline{\boldsymbol{d}}} \cdot \boldsymbol{v}. \tag{4.14}$$

The quantity $\boldsymbol{g}$ is the *gyrotropic vector density* and governs the dynamics of magnetic structures, while $\underline{\underline{\boldsymbol{d}}}$ is the *dissipation tensor*[2]. The total gyrotropic and dissipation terms are obtained by integrating over the volume of the sample:

$$\mathbf{G} = \int \boldsymbol{g}\ dV, \tag{4.15}$$

and

$$\underline{\underline{\boldsymbol{D}}} = \int \underline{\underline{\boldsymbol{d}}}\ dV. \tag{4.16}$$

This leads to the Thiele equation [19]:

$$\boldsymbol{F}_{\text{ext}} + \boldsymbol{G} \times \boldsymbol{v} + \alpha\ \underline{\underline{\boldsymbol{D}}} \cdot \mathbf{v} = 0. \tag{4.17}$$

The gyrotropic and dissipative terms correspond to the precessional and the damping terms in the Landau-Lifshitz-Gilbert equation, respectively. These describe the steady-state motion of micromagnetic structures in the presence of an external force

$$\boldsymbol{F}_{\text{ext}} = -\partial E / \partial \boldsymbol{X}. \tag{4.18}$$

In the next section, we discuss the analytic expression of the integrals (4.15) and (4.16) for the particular case of a vortex.

[2] The original definition of $\underline{\underline{\boldsymbol{d}}}$ includes the damping constant $\alpha$. We however prefer to keep $\alpha$ as a prefactor like in Ref. [56], which will be useful when we describe current-induced dynamics in chapter 7.

### 4.1.2 Internal forces acting on a vortex

The expression for the gyrotropic vector and the dissipation tensor were derived by Huber for the vortex [20, 138]. In addition to these two terms, we also describe the restoring force acting on the displaced vortex which is due to the finite size of the sample.

#### Force induced by the gyrotropic vector

In thin films the vortex structure does not vary significantly along the thickness of the sample. The angles of the magnetization $\theta$ and $\phi$ thus only depend on the position $(x, y)$ in the plane of the sample, and the gradients $\boldsymbol{\nabla}\theta$ and $\boldsymbol{\nabla}\phi$ are also in the plane of the vortex. The cross product (4.12) thus lies in the $z$ direction, perpendicular to the sample plane and the gyrotropic vector density is then given by

$$g_z = -\frac{\mu_0 M_s}{\gamma_0} \cos\theta \left( \frac{\partial\theta}{\partial x}\frac{\partial\phi}{\partial y} - \frac{\partial\theta}{\partial y}\frac{\partial\phi}{\partial x} \right). \tag{4.19}$$

From (4.12), the $z$ component of the gyrotropic vector is thus [19]:

$$G_z = -\frac{\mu_0 M_s}{\gamma_0} \iiint_V \cos\theta \; J(x,y) \; dx \; dy \; dz, \tag{4.20a}$$

where $J(x,y) = \partial(\theta,\phi)/\partial(x,y)$ is the Jacobian mapping the coordinate transformation form $(x, y)$ to $(\theta, \phi)$. Placing the origin of the coordinate system at the core of the vortex, the integration can be performed in cylindrical coordinates over the limiting values for the angular distribution of the vortex magnetization:

$$\begin{cases} \theta = 0 \text{ or } \pi \;\text{ for }\; r = 0, \qquad \theta = \pi/2 \;\text{ for }\; r = \infty \\ \phi = 0 \rightarrow 2\pi n, \text{ where } n \text{ is the winding number.} \end{cases}$$

Considering the angles in the counter-clockwise direction, the integral (4.20a) becomes

$$G_z = -\frac{\mu_0 M_s}{\gamma_0} \int_0^h \int_0^{2\pi n} \int_{\pi/2 \text{ or } \pi}^{0 \text{ or } \pi/2} \cos\theta \; d\theta \; d\phi \; dz \tag{4.20b}$$

for a sample of thickness $h$. The resulting gyrocoupling vector $\boldsymbol{G}$ for a vortex is then [20]:

$$\boldsymbol{G} = 2\pi \; \frac{\mu_0 M_s h}{\gamma_0} \; np \; \hat{\boldsymbol{z}}, \tag{4.21}$$

where $p$ is the core polarization: $p = +1$ for $(\theta = 0)$ at $r = 0$ and $p = -1$ for $(\theta = \pi)$.

Due to the dependence of $\boldsymbol{G}$ on the winding number, the force

$$\boldsymbol{F}_{\text{gyro}} = \boldsymbol{G} \times \boldsymbol{v} \tag{4.22}$$

is opposite on vortices and antivortices, inducing them to precess in opposite directions for identical polarizations[3]. The frequency of this motion is determined by the sample aspect ratio, and is described in the following section.

From the definition (4.12), we noted that the magnitude of the gyrovector effectively reflects the dependence of the magnetization on two spatial coordinates; hence the term "gyrocoupling vector" initially introduced by Thiele [19].

### Restoring force

When the vortex is displaced from its equilibrium position, the circular arrangement of the magnetization is distorted, resulting in an internal demagnetizing field opposing the displacement of the vortex. The vortex is therefore effectively bound within a magnetostatic potential well, which is close to harmonic for small displacements [140, 141]. The potential energy of the vortex is

$$E_{\mathrm{ms}} = \frac{1}{2}\,\kappa \boldsymbol{X}^2, \tag{4.23}$$

where $\boldsymbol{X}$ gives the position of the vortex and $\kappa$ is a positive constant. The resulting force

$$\boldsymbol{F}_{\mathrm{ms}} = -\kappa \boldsymbol{X} \tag{4.24}$$

tends to restore the vortex to its equilibrium position.

The restoring constant is inversely proportional to the initial susceptibility $\chi_0$ of the sample. For a rigid vortex in submicron samples with small aspect ratio [141, 142], it is given by:

$$\kappa = \pi \frac{\mu_0 M_s^2 h}{\chi_0}. \tag{4.25}$$

The initial susceptibility is a function of the sample thickness $h$ and radius $R$ [141]:

$$\frac{1}{\chi_0} = 2\frac{h}{R}\left[\ln\left(\frac{8}{h/R}\right) - \frac{1}{2}\right] \qquad \left(\frac{h}{R} \ll 1\right). \tag{4.26}$$

Considering the angular frequency of the motion $\boldsymbol{\omega} = \omega \hat{\mathbf{z}}$ and the velocity of the vortex $\boldsymbol{v} = \boldsymbol{\omega} \times \boldsymbol{X}$, where $\boldsymbol{X}$ is in the plane of the vortex, we get:

$$\begin{aligned} \boldsymbol{G} \times \boldsymbol{v} &= \boldsymbol{G} \times (\boldsymbol{\omega} \times \boldsymbol{X}) \\ &= (\boldsymbol{G} \cdot \boldsymbol{X})\boldsymbol{\omega} - (\boldsymbol{G} \cdot \boldsymbol{\omega})\boldsymbol{X} \\ &= -G\omega \boldsymbol{X}. \end{aligned} \tag{4.27}$$

[3] The gyrotropic force is formally equivalent to the Lorentz force on a charged particle [139]. Here, the out-of-plane magnetization creates a self-induced field whose direction is given by the core polarization, with the vortex skyrmion number $np/2$ (2.34) acting as the charge.

For low damping values, the dissipative term can be neglected and the Thiele equation (4.17) written as:

$$-\kappa \boldsymbol{X} + \boldsymbol{G} \times \boldsymbol{v} = 0 \tag{4.28}$$

In this approximation, the oscillation frequency of the vortex [140, 141] is

$$\omega_0 = \frac{\kappa}{G}. \tag{4.29}$$

From (4.21), (4.25) and (4.29), the vortex thus precesses with a frequency:

$$\omega_0 = \frac{1}{2}\frac{\gamma_0 M_s}{\chi_0}. \tag{4.30}$$

This frequency is a function of the aspect ratio of the sample through its dependence on $\chi_0$. A comparison with micromagnetic simulations shows however that this model does not adequately describe the vortex resonance frequency [141], systematically predicting a significantly higher value. The discrepancy largely comes from the fact that the (rigid) vortex displacement leads to the formation of surface magnetic charges at the sample edges. The result in an incorrect description of the vortex energy dependence on its position. This can be solved by requiring that the magnetization be parallel to the side surfaces, *i.e.* by enforcing the condition $\mathbf{m} \cdot \mathbf{n} = 0$, where $\mathbf{n}$ is a vector normal to the boundary. In this model [143, 141], the inverse susceptibility is given by

$$\frac{1}{\chi_0} = 9.98\frac{h}{R}, \qquad \text{for } \frac{h}{R} \ll 1. \tag{4.31}$$

and the frequency of the oscillations is:

$$\omega_0 = \frac{2}{9}\frac{\gamma_0 M_s}{\chi_0}. \tag{4.32}$$

The different numeric factors in equations (4.30) and (4.32) are due to the differences in the energy calculation in both models. Taking into account the vanishing side surface charges, equation (4.32) predicts frequencies which are in good agreement with simulations in the absence of damping ($\alpha = 0$) [141]. Comparison with experimental data [44, 144] shows that this analytic result also holds in soft magnetic materials with low damping, such as $Ni_{80}Fe_{20}$ (Permalloy) where $\alpha \sim 0.01$.

Generally, for submicron samples the resonant frequency of the vortex is below one GHz, typically in the range of a few hundreds of MHz.

#### Dissipative force

The dissipation force $\alpha \, \underline{\underline{\boldsymbol{D}}} \cdot \mathbf{v}$ introduces a "viscous drag" [20] and is described by the second rank tensor $\underline{\underline{\boldsymbol{D}}}$:

$$\begin{pmatrix} D_{xx} & D_{xy} \\ D_{yx} & D_{yy}. \end{pmatrix} \tag{4.33}$$

According to (4.13), $\underline{\underline{\boldsymbol{D}}}$ can be written as the product $\underline{\underline{\boldsymbol{S}}}\,\underline{\underline{\boldsymbol{S}}}^T$ [145] where

$$\underline{\underline{\boldsymbol{S}}} = \begin{pmatrix} \partial\theta/\partial x & \partial\theta/\partial y \\ \sin\theta(\partial\phi/\partial x) & \sin\theta(\partial\phi/\partial y) \end{pmatrix}. \tag{4.34}$$

Following (4.34), the volume integral (4.16) can explicitly be written [146] as:

$$D_{ij} = -\frac{\mu_0 M_s}{\gamma_0} \iiint_V \left( \frac{\partial\theta}{\partial i}\frac{\partial\theta}{\partial j} + \sin^2\theta \, \frac{\partial\phi}{\partial i}\frac{\partial\phi}{\partial j} \right) dx\, dy\, dz \quad (i = x, y,\ j = y, x) \tag{4.35}$$

where $D_{xy} = D_{yx} = 0$ [20] and we label $D_{xx} = D_{yy} = D_0$.

The largest contribution to this integral comes when the vortex is far from equilibrium, where $\sin^2\theta \sim 1$ and the divergence of $\theta$ is small [20], so that only the term in $\phi$ remains. The integration is straight-forward in cylindrical coordinates, over $\int \boldsymbol{\nabla}\phi\boldsymbol{\nabla}\phi \; r dr d\phi dz$. Using the expression for $\phi$ in a vortex introduced in section 2.2.3, $\varphi = n\phi + \varphi_0\frac{\pi}{2}$ and it follows that [95]

$$\boldsymbol{\nabla}\phi = \frac{n}{r}\hat{\phi}. \tag{4.36}$$

For a vortex of thickness $h$ and radius $R$, (4.35) becomes

$$\begin{aligned} D_0 &= -\frac{\mu_0 M_s}{\gamma_0} \int_0^h \int_0^{2\pi} \int_{r_{\text{core}}}^R \frac{n^2}{r^2} \, r dr d\phi dz \\ &= -\frac{\mu_0 M_s}{\gamma_0} \pi h \ln(R/r_{\text{core}}) \qquad (n^2 = 1 \text{ for (anti)vortices}) \end{aligned} \tag{4.37}$$

where the core radius is taken as the lower bound of the integration over $dr$ [20, 146].

Having explicitly expressed the internal forces acting on a vortex, in the following section we consider the expression of two external forces.

### 4.1.3 External forces acting on a vortex

We consider here the forces due to an external field and resulting from the interaction of a vortex with other vortices or antivortices. The force due to spin-polarized currents is discussed in chapter 7.

#### Force due to magnetic fields

When an external field is applied, the magnetization tends to align with the field, resulting in an increase in size of the regions where the magnetization is parallel to the field. The displacement of the vortex therefore depends on its vorticity. The resulting force $\boldsymbol{F}_{\text{B}_{\text{ext}}}$ is independent of the vortex polarization and causes its displacement perpendicular to the applied field [146]:

$$\boldsymbol{F}_{\text{B}_{\text{ext}}} = \mu\,(\hat{\boldsymbol{z}} \times \boldsymbol{H}_{\mathbf{ext}})\,. \tag{4.38}$$

Taking into account the vanishing side-surface charges ($\boldsymbol{m} \cdot \boldsymbol{n} = 0$) [143] the factor $\mu$ is [147]:

$$\mu = \frac{2}{3}\pi M_s R h \varphi_0, \tag{4.39}$$

where $\varphi_0 = 1$ for a counterclockwise circulation of the magnetization. The resulting motion is investigated in section 4.1.4.

#### Vortex-vortex interaction

The motion of a vortex can also be influenced by the presence of other nearby vortices. The vortex-vortex interaction is formally similar to the Coulomb force and has been derived explicitely for two-dimensional vortices [20, 148, 139]. In such systems, as long as the cores do not overlap, the force exerted by a vortex $i$ on a vortex $j$ is:

$$\boldsymbol{F}_{ij} = 2\pi S^2 J n_i n_j \frac{\boldsymbol{X}_i - \boldsymbol{X}_j}{(\boldsymbol{X}_i - \boldsymbol{X}_j)^2} \qquad i, j = 1, 2, ..., n. \tag{4.40}$$

This force is proportional to the exchange constant $J$ and the magnitude $S$ of the magnetization. It is however the winding number which determines whether it will be attractive or repulsive. For three-dimensional vortices, the explicit form of this force has not been derived [149], however its dependence on the winding number and the distance between vortices holds:

$$\boldsymbol{F}_{ij} \propto n_i n_j \frac{\boldsymbol{X}_i - \boldsymbol{X}_j}{X_{ij}^2}. \tag{4.41}$$

The interaction is topological, with the winding number acting as an effective charge. Notably, (4.41) does not depend on the relative orientation of the cores. This feature will be confirmed for three-dimensional vortices in chapter 5 using micromagnetic simulations.

### 4.1.4 Vortex motion

#### Initial displacement in an external field

In order to illustrate the dynamics in response to an external field, we consider a vortex in a Permalloy cylindrical sample with radius 100 nm and thickness 20 nm. We simulate its response following a short 60 mT Gaussian pulse applied in the plane of the sample. The width $\sigma$ of the pulse is of 100 ps. The vortex has a polarization $p = +1$, and the cases when $\varphi_0 = +1$ and when $\varphi_0 = -1$ are investigated. The dynamic calculations are performed using a typical damping constant value of $\alpha = 0.01$ [146, 150].

According to (4.38), the resulting force exerted on the vortex should cause its displacement away from the equilibrium position perpendicularly to the field, along a direction determined by the vorticity. In Fig. 4.1a and b, the simulations show that in fact the vortex initially moves *along* the field direction: in this case, the direction of the motion is determined by the vorticity as well as

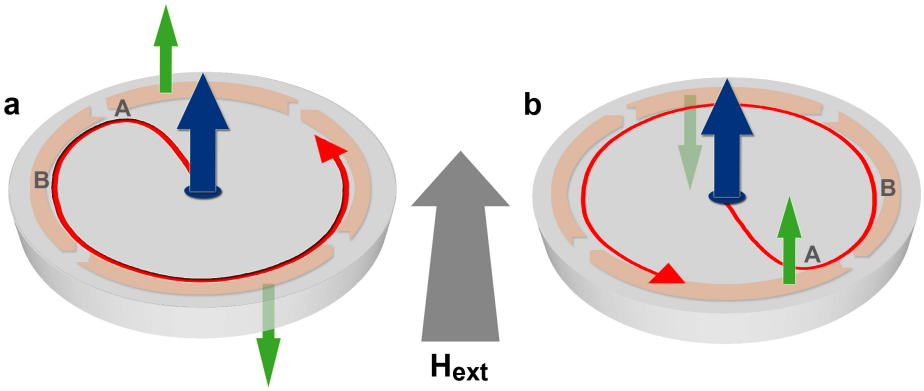


Figure 4.1: Simulated initial displacement of a vortex as a function of its vorticity in response to a sub-nanosecond field pulse. The trajectory over the first nanosecond is shown in red. **a**, A counterclockwise in-plane magnetization produces an initial displacement of the vortex in the direction of the field. **b**, The clockwise magnetization causes the vortex to move in the direction opposite to the field. The vorticity is indicated by the full circulating orange arrows. The torques exerted by the external field are shown in green. The blue arrow represents the polarization of the core. At moment **A**, the restoring force balances the action of the external field. At **B**, the overall displacement of the vortex corresponds to the one expected from equation (4.38).

by the core *polarization*. This behavior has been observed experimentally in Ref. [23]. The discrepancy with equation (4.38) comes from the fact that the latter describes the behavior of the vortex in a quasi-static field. In contrast, when a brief field pulse is applied, the torque term $-\gamma_0(\boldsymbol{M}_\mathrm{s} \times \boldsymbol{H}_\mathrm{ext})$ in the Landau-Lifshitz-Gilbert equation is predominant and determines the dynamics. Fig. 4.1 also shows the torques generated on different regions of the vortex, which cause the displacement of the core along the field direction when the in-plane magnetization rotates counterclockwise and against it when it rotates clockwise. The sub-nanosecond dynamics of the vortex is thus determined by the vorticity, as well as the polarization of the vortex.

After about 150 ps (point marked **A** in Fig. 4.1), the vortex displacement results in a restoring force which exactly balances the action of the external field. The vortex then describes a precessional motion as dictated by the gyrotropic vector (4.22). We note that after about 300 ps (point **B**), the overall displacement of the vortex is equivalent to the one expected from equation (4.38).

### Steady-state dynamics

Once the restoring force balances the action of the Gaussian field pulse, the vortex reaches an equilibrium radius and we have, neglecting damping:

$$\boldsymbol{G} \times \boldsymbol{v} = \kappa \boldsymbol{X}. \tag{4.42}$$

In a symmetric geometry, the general solution of this equation is a circular trajectory [140]:

$$\boldsymbol{X}(t) = X(\cos\ \omega t, \sin\ \omega t)\ \hat{\boldsymbol{r}}, \tag{4.43}$$

where $\hat{\boldsymbol{r}}$ is the radial unit vector. The radius $X$ of this trajectory depends on the strength of the excitation.

This motion can be maintained by using an oscillating field tuned to the resonant frequency of the sample or by periodically supplying energy to the system in the form of field pulses in phase with the vortex oscillation [23]. For both cases shown in Fig. 4.1, the direction of the motion at equilibrium is identical (counter-clockwise) and is governed by the core polarization. Owing to the dependence of $\boldsymbol{G}$ on the product of the winding number and the polarization, vortices always rotate counterclockwise when the direction of the core polarization points towards the observer, while antivortices rotate clockwise [23]. This motion represents the lowest excitation mode of a vortex, and its frequency lies in the sub-GHz range, as described earlier.

The first direct measurement of vortex motion was performed by Argyle *et al.* [21] using an optical microscope, by exploiting the magnetooptical Cotton-Mouton effect. The vortex was found at the intersection of two 90° Néel walls in an 80 nm thick micron-sized cross-shaped Yttrium iron garnet film. The system was driven at resonance by a sinusoidal in-plane field and, although the lateral resolution did not allow to image the core, the gyration of the vortex could be deduced from the motion of the 90° walls coupled to it. The comparison between the measured resonant frequency and calculations based on the Thiele equation (4.42) allowed to verify the analytic predictions. Using time-resolved Kerr microscopy, Park *et al.* [22], later measured the gyrotropic excitation of isolated vortices in micron and nanometer-size Permalloy disks. These measurements allowed to determine the resonant frequency of the vortices, but lacked the lateral resolution to precisely image the gyrotropic motion. Choe *et al.* used XMCD-PEEM [23] to directly image the gyrating motion of the vortex with a spatial resolution below 100 nm, combined with a temporal resolution of about 70 picoseconds. The position of the core was deduced from the evolution of the in-plane magnetization. Recently, Chou *et al.* [137] have demonstrated that the out-of-plane magnetization in the core could be directly imaged using scanning transmission x-ray microscopy (STXM). This technique uses the XMCD effect for the generation of the magnetic contrast and achieves a lateral resolution of about 30 nm. Additionally, because the images are formed by integrating the magnetic distribution over the thickness of the sample, this allows to take advantage of the broadening of the vortex core in thicker films mentioned in chapter 2.2.3. Our simulations show that the diameter of the vortex core in a 20 nm thick Fe disk is of approximately 7.5 nm, while it broadens to about 15 nm in a 50 nm thick disk. The same doubling of the core radius is observed in Permalloy.

Beyond the gyrotropic mode, higher frequency excitations can be excited, which however do not involve the vortex core [151, 152]. These are mainly magnetostatic standing modes arising from the finite geometry of the sample.

These have been investigated for example by means of time-resolved Kerr microscopy [153, 22, 154, 155] and Brillouin light scattering [151].

#### Relaxation in zero field

Once the field is switched off, the vortex spirals back to its equilibrium position. The relaxation time is a function of the value of the damping parameter $\alpha$ [141]. In submicron samples with $\alpha \sim 10^{-2}$, this is typically of the order of ten nanoseconds.

## 4.2 Vortex core deformations

In chapter 2, we pointed out that while analytic models describing the magnetization distribution of the static vortex core are generally in good agreement with micromagnetic simulations (Fig. 2.4), these however reveal the existence of a slight deformation of the in-plane magnetization [41]. This is attributed to the strong dipolar field of the core which affects the magnetic structure on a ring around it, leading to a negative "halo" of the out-of-plane component of the magnetization, as shown in Fig. 4.2a. The concentric deformation corresponds to negative magnetic charges, which compensate for the positive charge of the core.

In the case of a moving vortex, similarly an out-of-plane component of the magnetization develops in the vicinity of the core. This results in a localized dip in the magnetization traveling with the vortex [44, 45], as shown in Fig 4.2b. The distortion develops perpendicular to the vortex motion [140] and becomes pronounced for large amplitude displacements, when the radius of the motion is comparable to the radius of the vortex.

It was recently suggested in Refs. [57, 156] that the formation of this dip is due to a dynamic field associated with the gyrovector. The expression of this field is obtained following an approach introduced by Döring [157]. Considering a steady-state displacement, the damping along with the external driving field can be neglected and a kinetic potential is added to the total energy to account for the motion. The effective field (2.47) therefore now includes a kinetic part which induces the local precession of the magnetization according to (2.39):

$$\frac{d\boldsymbol{m}}{dt} = -\gamma_0[\boldsymbol{m} \times \boldsymbol{H}_{\text{kin}}] \tag{4.44}$$

where $\boldsymbol{m} = \frac{\boldsymbol{M}}{M_s}$ is the reduced magnetization. From equation (4.9), we obtain that

$$\frac{d\boldsymbol{m}}{dt} = -(\boldsymbol{v} \cdot \boldsymbol{\nabla})\boldsymbol{m}, \tag{4.45}$$

which leads to:

$$\gamma_0 \left[\boldsymbol{m} \times \boldsymbol{H}_{\text{kin}}\right] = (\boldsymbol{v} \cdot \boldsymbol{\nabla})\boldsymbol{m}. \tag{4.46}$$

Multiplying by $\boldsymbol{m}\times$ both sides of the above equation and using the vector identity (2.43) yields, with $\boldsymbol{m} \perp \boldsymbol{H}_{\text{kin}}$, the expression for the kinetic field as a

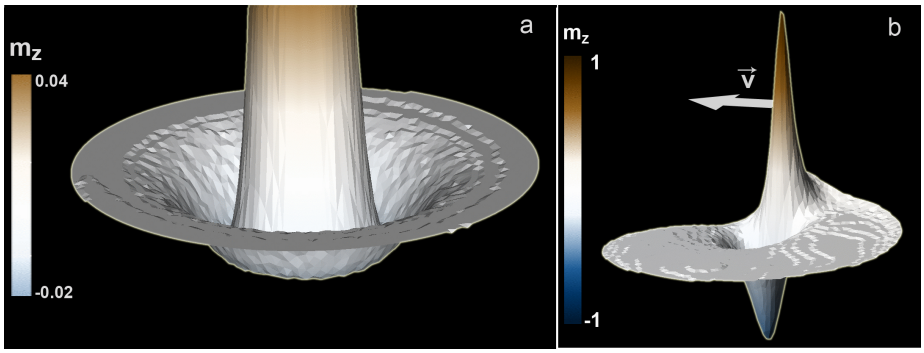


Figure 4.2: Simulations of the static and dynamic deformations of the vortex core structure. **a**, Topography of the out-of plane component of the magnetization around the core of a static vortex. The strong demagnetizing field of the core creates a symmetric deformation in its vicinity. **b**, The core of a moving vortex is strongly distorted during its motion as a function of its velocity. This results in the formation of a localized dip in the opposite direction of the core polarization.

function of the vortex velocity [57]:

$$\boldsymbol{H}_{\text{kin}} = -\frac{1}{\gamma_0}\boldsymbol{m} \times [(\boldsymbol{v} \cdot \boldsymbol{\nabla})\boldsymbol{m}] \,. \tag{4.47}$$

It was calculated in Ref. [156] that the out-of-plane component of this field is maximal at the core, in the direction opposite to its polarization. The strength of the kinetic field increases with the vortex velocity up to about 100-200 mT and its interaction with the local magnetization in the vicinity of the core is presently assumed to be responsible for the observed deformation. In this thesis, we investigate in detail the formation of the dip, its origin as well as its role in the ultrafast dynamics of vortices in chapters 5 and 8. In contrast however, we find that the rapid formation of the dip is attributed to the exchange field.

Finally, we note that the dynamics described in section 4.1.4 still hold, even when the core is strongly deformed. We find that they are in fact applicable as long as the out-of-plane component of the magnetization in the dip does not exceed approximately $\pm 0.8\ m_z$.

## 4.3 Vortex-antivortex interactions

Owing to the attractive nature of the force (4.41) between vortices and antivortices, these can form stable bound pairs in ferromagnets. Such a pair has a total winding number $n = 0$, and its motion has mostly been studied in two-dimensional systems [148, 158, 159, 160]. The coupled vortex and antivortex can undergo translational or rotational motion, depending on the relative polarization of their cores. Micromagnetic simulations have recently shown that

these pairs can also annihilate [46, 161] and that the annihilation process is equally governed by the relative core polarizations.

### 4.3.1 Steady-state dynamics

The motion of the pair in the absence of damping can be written as a function of the polarization $p$ of the vortex and the antivortex [148]:

$$p_{\mathrm{v}}\boldsymbol{v}_{\mathrm{v}} - p_{\mathrm{av}}\boldsymbol{v}_{\mathrm{av}} = 0. \tag{4.48}$$

where $\boldsymbol{v}_{\mathrm{v}}$ and $\boldsymbol{v}_{\mathrm{av}}$ are the respective velocities. This gives rise to two cases:

1. *The vortex and antivortex have identical core orientations:*
   The pair describes a translational motion, also called Kelvin motion [158], in a direction perpendicular to the axis of the pair. The velocity of the displacement is inversely proportional to the distance between the vortex and the antivortex [148].

2. *The vortex and antivortex have opposite core orientations:*
   The pair rotates about a common center with an angular velocity inversely proportional to the square of the distance between the vortex and the antivortex [159].

Owing to dissipation, the distance between the vortex and the antivortex is expected to decrease in time, leading to the dissolution of the pair. The dynamics of such vortex-antivortex annihilation are described below.

### 4.3.2 Annihilation

Micromagnetic simulations predict that the dynamics of the annihilation[4] process depends on the relative polarization of the vortex and antivortex cores. These were studied in detail in Ref. [46], which is the basis for the present discussion.

In the simulations, a single cross-tie was artificially isolated in a square thin-film sample and the structure was left to dynamically relax to a vortex state in the absence of an external field.

#### Dynamics for identical polarizations

For parallel core orientations, the vortices were observed to rotate about the antivortex with decreasing radius. This follows from (4.48), which then reads for the three-body system:

$$p_{\mathrm{v}1}\boldsymbol{v}_{\mathrm{v}1} + p_{\mathrm{v}2}\boldsymbol{v}_{\mathrm{v}2} = p_{\mathrm{av}}\boldsymbol{v}_{\mathrm{av}}, \tag{4.49}$$

[4] The term *vortex annihilation* is equally used in the literature to describe the expulsion of the vortex from a sample [162]. In this thesis, we only use it in connection to the dissolution of a vortex-antivortex pair.

such that if the antivortex is pinned, the two vortices rotate about it in a direction defined by their gyrotropic vectors[5].

As the radius of the motion decreases, the cores merge and a 180° rotation of the system results in the continuous unwinding of the in-plane magnetic structure into a single vortex structure.

### Dynamics for opposite polarizations

When the vortex and antivortex cores are antiparallel, according to (4.49) one of the vortices is required to have zero velocity. The other vortex and the antivortex then rotate about each other as the distance between the two structures decreases.

The pair however does not dissolve smoothly, and the annihilation is mediated by the injection of a Bloch point at one of the surfaces and its propagation through the film thickness. As the singularity traverses the sample, it dissolves the vortex-antivortex structure. As a result, the total energy of the system rapidly decreases as shown in Fig. 4.3, and the exchange energy of the two cores is released in the form of spin waves. The production of spin waves following the vortex-antivortex annihilation has also been reported by Lee *at al.* [163] and studied in detail in Ref. [164].

It has been pointed out in Ref. [165] that the nature of the annihilation processes described above has a topological origin. For an identically polarized vortex-antivortex pair, the total skyrmion number $q = np/2$, along with the winding number $n$ are zero. When the pair dissolves, these topological quantities are conserved and the magnetic structure can unwind continuously. However, when the vortex and the antivortex are oppositely polarized, the total skyrmion number changes from $q = +1$ to $q = 0$ following the annihilation. Such a discontinuous transformation can only be mediated by a singularity.

The skyrmion configuration in ferromagnets has been studied in Refs. [166, 167, 168]. Its exchange energy is given according to Refs. [97, 165] by

$$E_{\text{exc(Skyrmion)}} = 8\pi A h \tag{4.50}$$

and only depends on the exchange constant $A$ and the film thickness $h$. The energy obtained from (4.50) is in good agreement with the decrease in energy observed in Fig 4.3, which shows the time evolution of the exchange energy during the annihilation process[6].

[5] If the system is assumed to describe a translational motion, then the antivortex velocity should be double of that of the vortices, which would break the symmetry of the system and also oppose the attractive force (4.41). Hence, in the absence of an external field the antivortex remains pinned between the rotating vortices.

[6] Remarkably, simulations of vortex-antivortex annihilation carried out in Ref. [169] within the framework of lattice quantum chromodynamics predict a similar energy signature for the annihilation process, illustrating its topological nature.

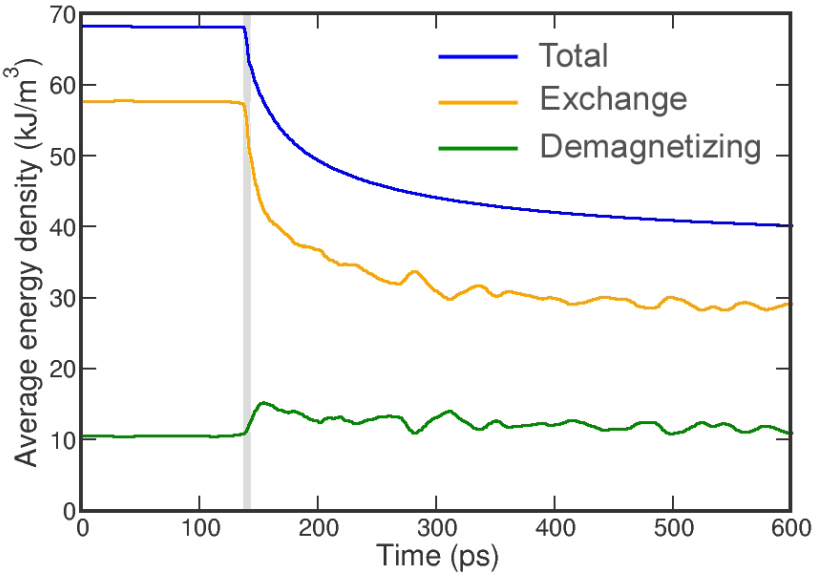


Figure 4.3: Time evolution of the partial and total average energy densities during the vortex-antivortex annihilation process in a 100×100×10 nm Permalloy thin film element. The grey area marks the duration of the annihilation process, which causes a steep decrease in the total exchange energy. The oscillations of the demagnetizing and exchange energies are consistent with the formation and propagation of spin waves. The plot is based on the data in Ref. [46].

## 4.4 Beyond the rigid body approximation

In this chapter, we gave an overview of vortex dynamics based on the analytic expression given by the Thiele equation and on experiments which have largely confirmed the theoretical predictions. Most of these investigations focused on the steady-state dynamics characterized by the precession of the vortex. We also described dynamic processes predicted by micromagnetic simulations, such as the distortion of the vortex core. This dynamic feature shows in which way the rigid body model breaks down for large amplitude displacements of the vortex – or equivalently, for large velocities. While the vortex behavior in not considerably affected unless the core is strongly deformed, this leads us to ask: How is the dynamics affected when this distortion becomes maximal? We answer this question in the next chapter, where we investigate the ultrafast dynamics of the vortex.

Another dynamic process discovered by means of simulations is the annihilation of a vortex-antivortex pair. In this context, does this annihilation, which was studied in an artificial setup, equally occur in measurable dynamic processes? The next chapter shows that it does, and moreover in a quite unexpected manner.

# 5

# Ultrafast vortex core reversal[1]

In the previous chapter, the gyrotropic mode of the vortex was described. This mode occurs for low-amplitude excitations, when the force generated by an external field exactly compensates the internal restoring force of the vortex. The oscillatory motion can therefore be sustained when the vortex is driven at resonance. The question then arises:

- What happens when the vortex is driven by a *strong* and *short* perturbation?

In this chapter, we show that strong and non-resonant perturbations lead to a novel process in micromagnetism: *the reversal of the vortex core*. This reversal was observed experimentally by VanWaeyenberge *et al.* [27] using time-resolved scanning transmission x-ray microscopy (STXM). In that experiment however, the change in core polarization was found to occur in response to short bursts of a *resonant* excitation. We demonstrate here that the reversal is not related to the vortex resonance and that it can easily be triggered by unipolar field pulses only a few tens of mT strong. Moreover, our simulations elucidate the details of the complex micromagnetic mechanism leading to the reversal: it is mediated by a rapid sequence of vortex-antivortex creation and annihilation processes, which unfold over only a few tens of picoseconds.

The fact that this process can be triggered by a single, low in-plane field pulse is surprising in view of the high stability of the vortex core. Indeed, in a study based on micromagnetic simulations, Thiaville *et al.* [28] found that it is necessary to overcome an energy barrier of about 500 $k_{\mathrm{B}}T$ in zero field to switch the core. Kikuchi *et al.* showed experimentally that the core can be reversed by means of a strong static external field applied antiparallel to its orientation. In that case, the core structure was effectively crushed by the external static field and rebuilt in the opposite direction. The required field varied between 300 and 500 mT [29, 170, 171]. Despite suggestions that the vortex core could be used for binary data storage [29, 171], such high switching fields made vortices rather impractical.

[1]The material in this chapter is based on *R. Hertel, S. Gliga, M. Fähnle, and C. M. Schneider, Phys. Rev. Lett* **98***, 117201 (2007)* and *S. Gliga, R. Hertel and C.M. Schneider, Physica B* **403***, 334 (2008).*

Here, we first present the experimental evidence for the core reversal triggered by means of low resonant in-plane fields, as reported in Ref. [27], together with the proposed micromagnetic model for the reversal. Second, we detail the results of our simulations, including the micromagnetic reversal mechanism. Third, we provide a diagram for the operational range of this reversal in the studied sample triggered by unipolar field pulses. Fourth, we describe the energy evolution of the vortex during the reversal. Finally, we conclude with recent experiments by Weigand *et al.* [172], confirming that the vortex core can be switched by means of single unipolar field pulses.

## 5.1 Experimental observation of the vortex core reversal

For a resonantly excited vortex, the radius of the gyrating motion is a function of the applied field strength, as given by equation (4.42). An increase in the amplitude of the driving field is thus expected to cause an increase of the gyration radius, as long as the vortex is not expelled from the sample. In Ref. [27], the gyrotropic mode of a vortex in a square micron-sized Permalloy sample was excited via an alternating in-plane field tuned at the resonant frequency of the sample. This resonant excitation typically requires low fields (0.1 mT in that experiment) applied over tens to hundreds of ns. The subsequent gyrating motion of the vortex was imaged using time-resolved STXM [173, 174].

In X-ray transmission microscopy, the sample is illuminated by cicularly polarized light. Owing to the magnetic dichroism effect, as the light traverses the sample, it is absorbed depending on the orientation of the light helicity vector relative to the local magnetization, thereby generating the magnetic contrast. In this manner, the trajectory of the core could be deduced from the changes of the in-plane magnetization.

Surprisingly, following an increase in the amplitude of the AC field to 1.5 mT over an oscillation period, the core was observed to gyrate in the opposite direction, unambiguously indicating that its polarization had been reversed. A model for this reversal process, sketched in Fig. 5.1, was suggested by Hertel in Ref. [27], based on the conservation of the winding number. Indeed, in contrast to the case when it is "crushed" by a strong external field, the core cannot directly switch its polarization in response to an in-plane field. It was thus suggested that a *new* vortex must be created with opposite polarization. However, the total winding number of a thin film-element is a topological invariant (section 2.2.3), so this process must equally result in the production of an antivortex. This would then naturally trigger the vortex-antivortex annihilation process described in section 4.3, leaving behind a vortex with opposite polarization.

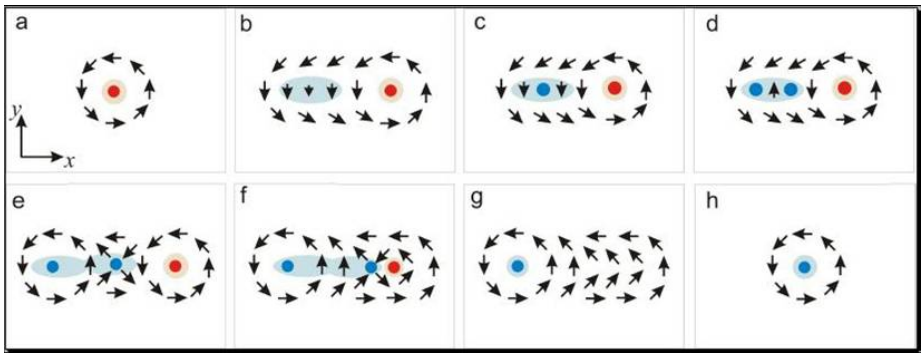


Figure 5.1: Proposed mechanism for the vortex core reversal mediated by the production of a new vortex-antivortex pair with opposite polarization, followed by the annihilation of the new antivortex with the original vortex. Reprinted by permission from Macmillan Publishers Ltd: *B. Van Waeyenberge* et al., *Nature 444, 461 (2006)*.

## 5.2 Reversal triggered by unipolar field pulses

In contrast to the experimental study in Ref. [27], our aim was to determine the vortex behavior under the influence of *short and strong unipolar* in-plane field pulses. The simulations demonstrate that the core switch is not connected to the relatively slow resonant frequency of the vortex: it in fact unfolds over only a few tens of picoseconds. The reversal is schematically represented in Fig. 5.2.

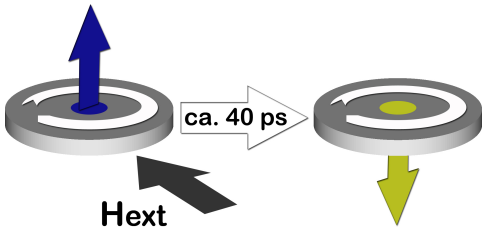


Figure 5.2: Schematic representation of the field-pulse driven vortex core switch. The vortex core orientation can be reversed by a short in-plane field pulse triggering the switching process, which unfolds over about 40 ps.

The simulations are performed for a 20 nm thick Permalloy disk with a radius of 100 nm. The sample is discretized into 150 780 tetrahedral elements. The largest distance between neighboring discretization points is approximately 3 nm. This results in an average (equivalent cubic) cell size[2] of about 1.6 nm$^3$. The material parameters are: $A = 13$ pJ/m (exchange constant), $\mu_0 M_s = 1.0$ T ($M_s$: saturation magnetization), $K_u = 0$ ($K_u$: magnetocrystalline anisotropy) and $K_s = 0.1$ mJ/m$^2$ [175] ($K_s$: surface anisotropy). The Gilbert damping

[2]Because all the tetrahedra are not of equal size, the cell size cannot be obtained directly from the formula for the volume of a tetrahedron.

constant is $\alpha = 0.01$ [150].

### 5.2.1 Core reversal mechanism

A typical example of the core reversal process is presented in Fig. 5.3 for the case of an 80 mT Gaussian-shaped field pulse of duration 60 ps, applied in the plane of the sample. The left column of Fig. 5.3 shows the $x$ component of the magnetization as it would be imaged for example using the XMCD effect. In order to clearly visualize the microscopic processes leading to the core reversal, we highlight the $m_x = 0$ and $m_y = 0$ isosurfaces as illustrated in Fig. 2.2. The intersection of these isosurfaces marks the exact position of the vortex core. The right column of Fig. 5.3 shows a magnification of the region around the vortex. Before the external field is applied, the isosurfaces appear as straight ribbons, oriented along the $x$ and $y$ axis, respectively, crossing each other perpendicularly at the center of the core. When the field pulse is applied, the vortex shifts away from its original position along the field direction and the formerly circular arrangement of the magnetization around the core is stretched, resulting in bent isosurfaces. A few picoseconds after the peak value of the pulse is reached, the strong distortion of the magnetization leads to the formation of two additional intersections, marking the creation of a vortex-antivortex pair. We find that the magnetization direction in the core of the new vortex is opposite to the polarization of the original core. Once the pair is created, the antivortex quickly moves towards the original vortex and they rapidly annihilate according to the process discussed in section 4.3.2. The vortex-antivortex annihilation results in the sudden generation of spin waves, as reported in Refs. [46, 163]. The final magnetic structure is a vortex having opposite polarization with respect to the original vortex. The core switching does not affect the in-plane sense of rotation of the magnetization and hence results in a change of the vortex handedness.

### 5.2.2 Evolution of the out-of-plane magnetization

The change in orientation of the perpendicular core magnetization, while not explicitly shown in Fig. 5.3, can be seen in Fig. 5.4. At equilibrium, the slight symmetric distortion of the in-plane magnetization in the direction opposite to the core shown in section 4.2 is visible. The dynamic evolution of this oppositely magnetized region is then shown at the moment of the pulse maximum (labeled *0 ps* on the figure). When the out-of-plane component locally reaches $m_z = -1$, the structure evolves into a vortex-antivortex pair. The pair nucleation is followed by the annihilation of the original vortex with the new antivortex. In this dynamic process, we interpret the formation of the out-of-plane component as a result of the tendency of the system to reduce the exchange energy connected with the strong inhomogeneity of the in-plane magnetic structure. Indeed, the vortex structure is heavily distorted within a few tens of ps, leading to an asymmetric distribution of the magnetization around the core. This asymmetry is characterized by a region where the $m_x = 0$ and the $m_y = 0$ isosurfaces approach each other, such that the distance over which the magnetization changes

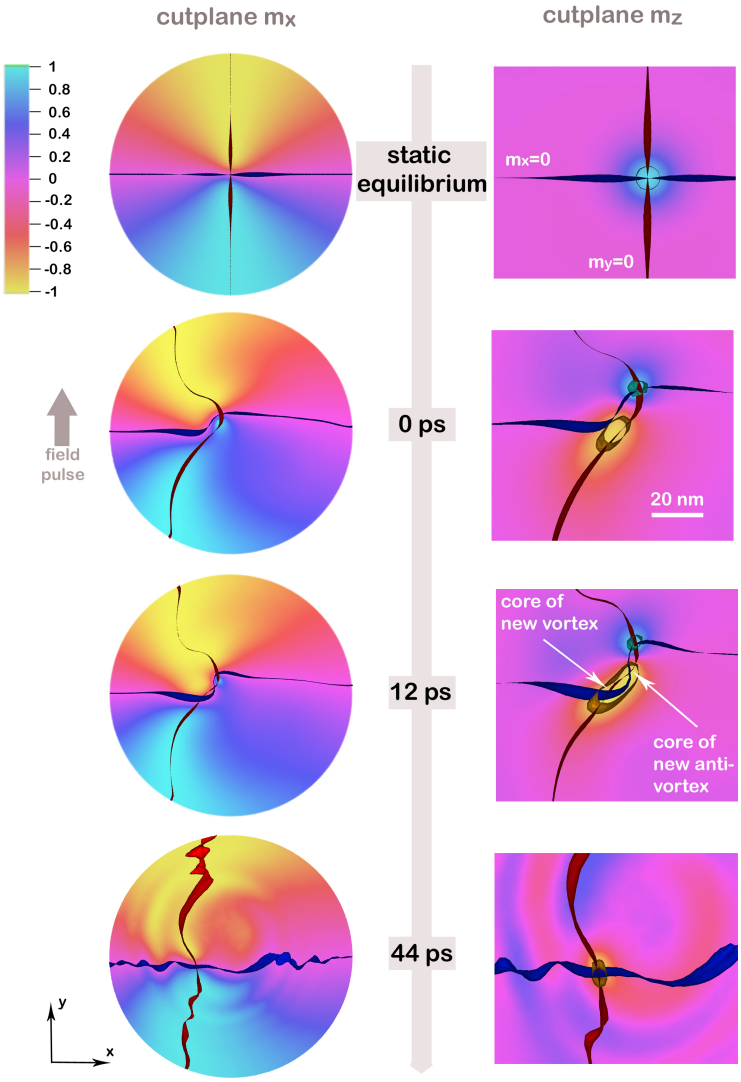


Figure 5.3: Pair-creation mediated vortex core reversal in the Permalloy disk-shaped sample. A Gaussian field pulse is applied in the sample plane, along the y axis. The **left column** shows the evolution of the x component of the magnetization. The times indicated are relative to the pulse maximum. The blue and red ribbons represent the $m_x = 0$ and $m_y = 0$ isosurfaces, respectively. The **right column** shows a magnification of the region where these ribbons intersect, marking the cores of the original vortex. At 12 ps after the pulse maximum, a new vortex-antivortex pair is created and finally a single vortex remains at the issue of the reversal. Its core has opposite polarization with respect to the initial vortex, indicated by the yellow color on the underlying cutplane, which represents the z component of the magnetization. The green and orange cylindrical ribbons are the isosurfaces where $m_z = 0.8$ and $m_z = -0.8$, respectively.

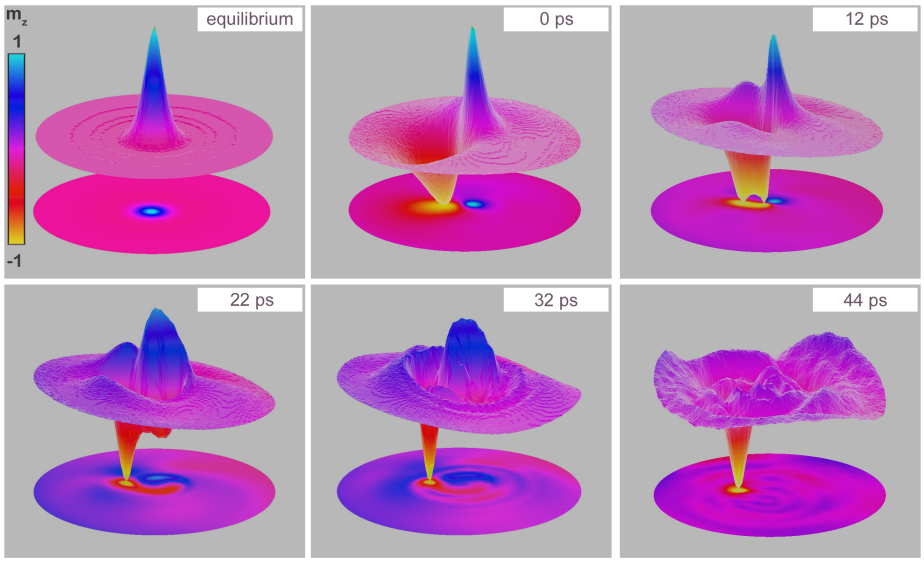


Figure 5.4: Topography of the out-of-plane component of the magnetization during the core switch. A small variation in $m_z$ outside the core can be seen at equilibrium (static dip). The formation of a large negative dip of $m_z$ is shown at the pulse maximum (0 ps). At 12 ps following the pulse maximum, this dip evolves into a pair, with two separate points at $m_z = -1$. About 10 ps later, this leads to the annihilation of the original vortex with the new antivortex. At 32 ps, the produced spin waves are visible and the new vortex with opposite polarization is shown at 44 ps.

its in-plane direction by 90° is rapidly reduced to only a few nanometers. The system circumvents the formation of such a strongly inhomogeneous structure by rotating the magnetization out of the plane. The exchange field is therefore responsible for the rapid *formation* of the pronounced out-of-plane component in the distorted vortex structure in this case, thereby locally reducing the in-plane component of the magnetization and maintaining a smooth transition, as shown in Fig. 5.4 at *0 ps*. On the other hand, as discussed in section 4.2, the *direction* into which this out-of-plane dip develops is determined by the magnetostatic field of the vortex core.

### Gyrofield

We now use the results presented above to probe the possible effect of the gyrofield introduced in equation (4.47) on the evolution of the dynamic distortion of the core. Following Ref. [57], we estimate the strength of the out-of-plane component of this field to about 170 mT in the direction opposite to the core polarization. If this field is responsible for the formation of the strong out-of-plane component of the magnetization, the distortion should not evolve in its

absence. We thus attempt to counteract the effect of the gyrofield by applying a static field along the direction of the core polarization, in addition to the 80 mT in-plane switching pulse. We find that the switch is indeed suppressed, however only for static fields of about 450 mT – well above the gyrofield strength. This value is in fact comparable to the demagnetizing field of the (static) vortex core, rather indicating that it is necessary to dynamically "crush" the magnetization dip in order to suppress the reversal. Our results therefore do not support the interpretation according to which the dip formation is driven by the gyrofield. This can equally be understood by considering the gyrofield strength: a field of about one hundred mT is expected to influence the magnetization over a few ns. In this context, the gyrofield may describe the buildup of the dip during the slower, resonant excitation of the vortex. However, it cannot drive the observed *fast* buildup of the dip, within only a few tens of ps. We further investigate this aspect in chapter 9, where we find that a local field above one Tesla is required to trigger the formation of a vortex-antivortex pair over a few tens of ps.

### Dipolar field

Next, we investigate whether the dipolar field generated by the core plays a role in the dynamic formation of the dip. To this effect, we computed the magnetic flux within the vortex structure as well as outside the sample, where the flux is equal to the stray field. The results are shown in Fig 5.5 at equilibrium and during the vortex motion, when the dip in magnetization is pronounced ($m_z = -0.6$). For a static vortex, the core region is the only source of a radial dipolar field. When the vortex is displaced from equilibrium however, the stray field configuration is mainly determined by the volume charges arising from the distortion of the in-plane structure of the magnetization. If the stray field of the core played an active role in the evolution of the dip, the field lines generated at the vortex core should close through the dip. This is however not the case, as seen in Fig. 5.5b.

From these results, we thus conclude that:

1. The dipolar field of the moving core does not play a role in the dynamic evolution of the out-of-plane distortion of the magnetization;

2. The evolution of the dip is not experimentally observable using techniques sensitive to the stray field;

3. The absence of dipolar interactions between the vortex core and the dip illustrates the fact that the vortex-vortex force (4.41) does not depend on the core polarization.

These findings as well as the discrepancy between the gyrofield model and our simulations are consistent with our interpretation that the evolution of the dip is driven by the exchange field.

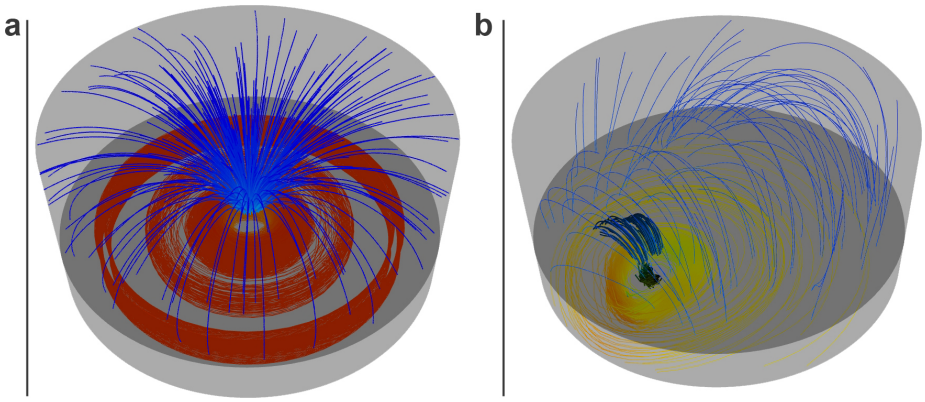


Figure 5.5: Evolution of the dipolar field in a moving vortex. **a**, Vortex at equilibrium: the flux inside the sample is shown in red and the stray field computed in an "air cap" above the sample is in blue. **b**, The flux computed in a displaced vortex (close to the sample edge) is shown in yellow. The distortion of the in-plane structure leads to the formation of magnetic charges: the resulting stray field is indicated by the thin blue lines. Thick blue lines represent the stray fields of the core and the dip.

#### Stability under perpendicular fields

Until now, the considered field pulses were perfectly aligned with the plane of the sample. We therefore verify the stability of the switching mechanism with respect to deviations from perfect alignment. To this effect, we apply the 80 mT field pulse used in Fig. 5.4, at angles up to 20°. We find that the switching mechanism remains unaffected. When the field pulse is applied at larger inclination angles, the switching process no longer occurs. This is however due to the fact that in those cases, the in-plane component of the field is reduced below 75 mT and is not sufficient to trigger the reversal. The detailed field parameters required to switch the core are studied below.

## 5.3 Switching field parameters

We conducted a systematic study of the parameters necessary to trigger the core reversal and found that it occurs only for well-defined combinations of the applied pulse duration and strength, as shown in Fig 5.6. The diagram was obtained for the sample described in section 5.2 by varying the pulse width $\sigma$ in steps of 2.5 ps between $t = 0$ and $t = 20$ ps, and in steps of 10 ps afterwards. The pulse strength was varied in increments of 5 mT throughout the studied range. The precise boundaries in the diagram weakly depend on the size of the discretization cells: these variations are attributed to the mesh dependence of the Bloch point nucleation [28] linked to the vortex-antivortex annihilation. To

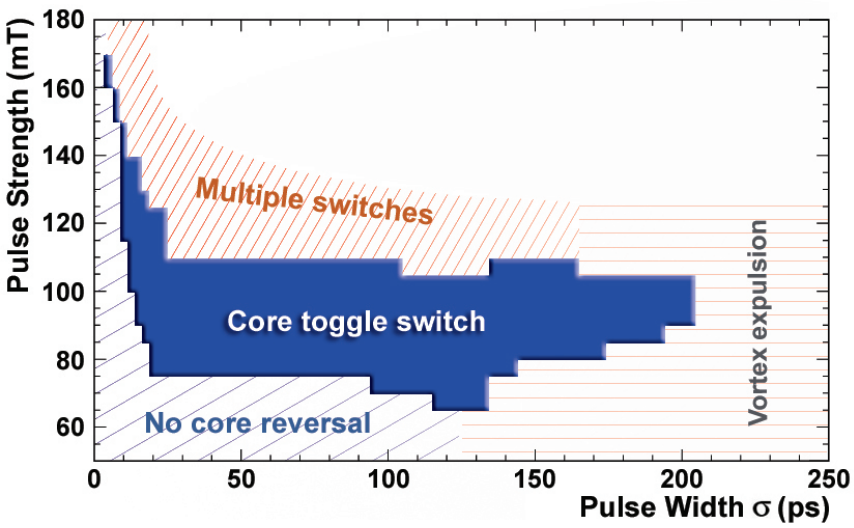


Figure 5.6: Diagram for the pulse parameters leading to a toggle switch of the vortex core in a Permalloy disk, 100 nm in radius and 20 nm thick. The pulse duration is quantified by its width $\sigma$ and the strength by its maximum value.

estimate this dependence, the distance between discretization nodes was varied by $\pm 0.7$ nm at the edges of the diagram. For example, for a pulse 20 ps wide with amplitude 80 mT, the variation in the field required to switch the core is of +5.0 mT for a mesh with a distance of about 2.3 nm between nodes, as compared to a mesh with a distance of about 3 nm. The variation is of $-5.6$ mT for a node spacing of 3.7 nm, as compared to 3 nm.

We find that the phase space within which the core reversal occurs is relatively narrow, in particular in order to obtain a single, controllable toggle switch (blue region). Too low fields do not cause the core to switch, while high fields give rise to sequences of multiple pair creations and annihilations. Notably, by increasing the pulse duration, the switching can be accomplished using 65 mT pulses. In contrast, increasing the applied field strength allows triggering of the switch with pulses only 5 ps long. Ultimately, too strong and too long pulses lead to a temporary expulsion of the vortex from the sample. Some regions of the diagram do, however, exhibit particular behaviors:

- *Bottom region:* 65 mT pulse, $\sigma = 130$ ps. With increasing pulse duration, the vortex is driven close to the sample edge. In this case, the switch occurs when the vortex core is only a few nm away from the edge. For longer field pulses, the vortex is expelled from the sample.

- *Top region:* 110 mT pulse, $\sigma = 140$ ps. For pulses between 110 ps and 140 ps, the overall excitation of the sample causes the core to switch twice in a region where a single switch is expected. In this case, the second

switch seems to be triggered by the spin waves produced following the annihilation.

- *Expulsion region:* In this region, the long field pulses cause the expulsion of the vortex from the sample, unless they are strong enough to cause the core reversal in the vicinity of the sample edge. This results in the step-like shape of the diagram. For a larger sample, the diagram would presumably extend further, and it would take longer pulses to expel the vortex.

While the pulse parameters required to reverse the core are sensitive to the sample geometry, the reversal itself is insensitive to variations in particle shape or size. Indeed, we find that the reversal process occurs as well in elliptical and square submicron sized magnetic thin-film elements. The reversal is also independent of the value of the damping constant $\alpha$ used in the Landau-Lifshitz-Gilbert equation[3]. This suggests that the field-pulse induced generation and subsequent annihilation of magnetic vortex-antivortex pairs is a *general property* of magnetic vortices. The switching should therefore equally be triggered by electric current pulses, which we demonstrate in chapter 7.

## 5.4 Energy evolution

The results presented so far have described the reversal mechanism and provided a detailed map of the field parameters required to trigger the switch. Further understanding of the switching process can be obtained by considering the energy evolution of the vortex during the reversal. In Fig. 5.7, we show the time evolution of the partial energies during the core reversal triggered by a 90 mT Gaussian pulse of width $\sigma = 30$ ps. The demagnetizing, exchange and surface anisotropy energy densities are plotted as well as their sum, the internal energy. The total energy also includes the Zeeman contribution. Under the influence of the external field the in-plane magnetic structure is gradually distorted and the exchange energy increases smoothly, eventually becoming the dominant term at the moment when the vortex-antivortex pair is formed. The subsequent annihilation is marked by a sudden decrease in the exchange energy. This is associated with the injection of the Bloch point in the sample and its subsequent expulsion. The singularity propagates through the 20 nm thick sample, traversing it within approximately 10-12 ps, independent of the external field parameters.

The propagation of the Bloch point is shown in Fig. 5.8a,b using the isosurface representation. In the simulations, the singularity always propagates along the vortex or the antivortex core, resulting in their merging and dissolution. Given the difficulties mentioned in section 3.5 in accounting for the Bloch point in a continuum model, its computed position may be the result of discretization artifacts. It is, however, consistent with its topology, as shown earlier in

[3] An example of the core reversal in an elliptical sample for a higher value for $\alpha$ performed in this thesis can be found at ftp://ftp.aip.org/epaps/phys_rev_lett/E-PRLTAO-98-083710. Such variations are described in further detail in chapter 8.

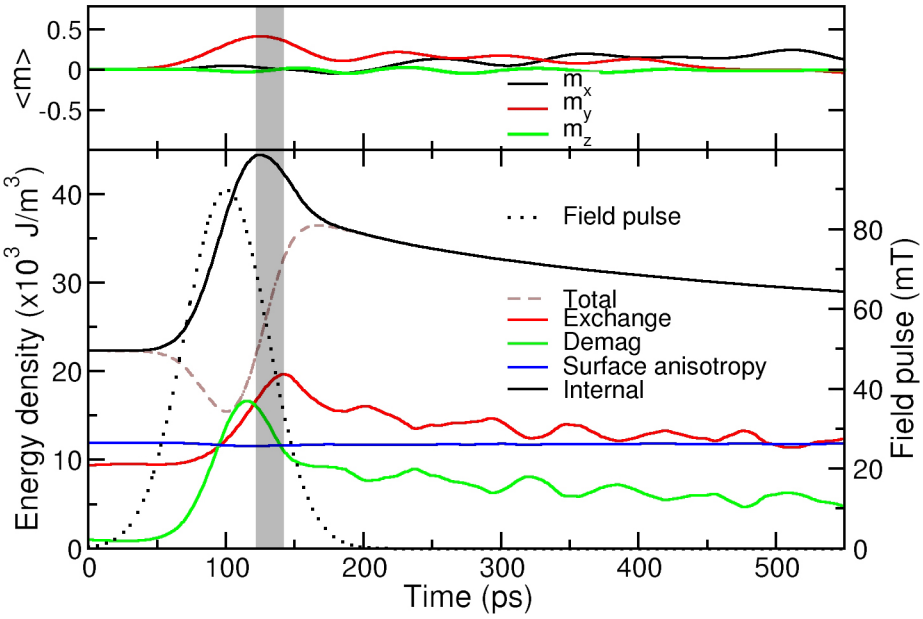


Figure 5.7: **Top**, Temporal evolution of the space-averaged magnetization components, showing the field-induced displacement of the vortex, and its precession back to equilibrium. **Bottom**, Average energy densities during the vortex core reversal process. The scale on the left refers to the average energy densities; the one on the right to the applied field pulse. The shaded region indicates the time elapsed between the pair creation and the end of the annihilation. This duration is independent of the excitation parameters.

Fig. 2.6 where a circulating Bloch point has the same in-plane structure as a vortex. A 90° rotation of this configuration yields the antivortex structure (counter-circulating Bloch point) [100]. On the basis of these considerations, we therefore do not rule out that the Bloch point may indeed have preferred propagation paths along the vortex or antivortex core.

Following the vortex-antivortex annihilation, spin waves are produced (shown in Fig. 5.8c), causing the oscillations of the exchange and demagnetizing energy densities observed in Fig. 5.7. This ringing [24, 176] lasts for a few ns, until the energy released from the cores is dissipated. At the same time, the vortex relaxes to its original position. During the entire switching process, the surface anisotropy energy does not significantly vary (maximum variation of about 2%), showing that it does not play a role in the core switch.

In the reversal investigated in Fig. 5.7, the core switches approximately 40 ps after the field maximum, as in the case presented in Fig. 5.3. While the time of the pulse maximum has been arbitrarily chosen as a point of reference, from the preceding analysis the switching process is defined by two events: first, *the creation of a new pair*, and second (some 10 ps – 20 ps later) the onset of

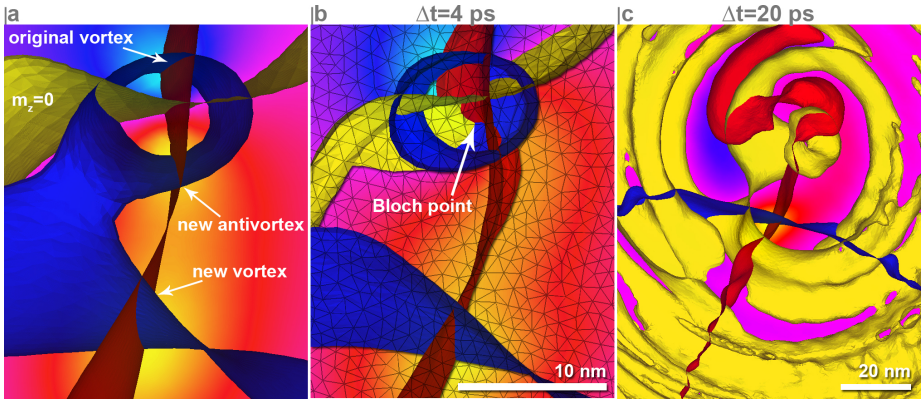


Figure 5.8: Simulated Bloch point propagation during the vortex-antivortex annihilation shown in the studied Permalloy disk with a node discretization distance of 1 nm. This yields an effective cell size of 0.5 $nm^3$. **a**, Production of the vortex-antivortex pair. Along the blue and red isosurfaces $m_x = 0$ and $m_y = 0$, respectively. Along the yellow-green isosurface separating the original vortex and the new antivortex, $m_z = 0$. The background colors represent the $z$ component of the magnetization, using the same color scale as in Fig. 5.3. **b**, Snapshot of the Bloch point traversing the sample. The Bloch point is located at the intersection of the three isosurfaces. The finite-element mesh is shown along the cutplane containing the Bloch point: the singularity is located between the discretization points, where the value of the magnetization is interpolated. In this case, the Bloch point propagates along the antivortex core, dissolving both cores in its wake. **c**, Resulting spin wavefronts following the annihilation highlighted by the $m_z = 0$ isosurface.

the *annihilation process*, itself lasting about 10 ps – 15 ps. These time scales are independent of the external field parameters. In contrast, the formation of the dip strongly depends on the pulse strength and duration. In chapter 9, we demonstrate that it is possible to bypass the dip formation and to directly trigger the switching process, resulting in effective switching times of only a few tens of ps.

## 5.5 Experimental observation of single-pulse induced core reversal

Recently, using time-resolved STXM, Weigand *et al.* [172] have experimentally confirmed this possibility of triggering the core reversal using single short field pulses. In their experiment, a vortex in a submicron-sized Permalloy square element was excited by means of in-plane non-resonant, unipolar nanosecond field pulses. Although the imaging technique was stroboscopic, the successive core reversals could be resolved, thereby also demonstrating the deterministic aspect

of the core switch. They have equally found that the switch can be triggered by 700 ps long pulses of about 10 mT. Such pulses would have caused the expulsion of the vortex from our sample (see Fig. 5.6), showing the strong dependence of the switching field parameters on the sample size. The dependence of the field parameters on the vortex dimensions was also investigated in Ref. [177].

In another experiment by Vansteenkiste *et al.* [37], the dynamic deformation of the vortex core was imaged using STXM, providing experimental proof for the deformation of the core, which precedes the reversal. Differential images obtained from micromagnetic simulations and convoluted with the experimental resolution were used to interpret the data. Neudert *et al.* [178] also observed a strong deformation of the vortex core in a micron-sized Permalloy disk in response to nanosecond field pulses using time-resolved Kerr microscopy. However, owing to both the limited lateral resolution (ca. 300 nm) and to the stroboscopic nature of the imaging technique, it was not possible to determine whether this corresponded to a stretched vortex or to a superposition of two vortices with switched polarizations. In the same paper, the authors also used micromagnetic simulations to demonstrate that the applied field pulses could lead to the core reversal.

## 5.6 Summary: The fastest field induced switching process

In this chapter, we have presented a detailed description of the ultrafast micromagnetic mechanism, which leads to the reversal of the vortex core. This reversal involves a series of complex processes that unfold on the nanometer scale, namely the creation of a vortex-antivortex pair followed by an annihilation process. The new pair results from the evolution of an oppositely magnetized region in the vicinity of the core. This complex chain of events unfolds on a time scale of a few tens of picoseconds and only requires a short in-plane field pulse of suitable shape to be initiated. The ultrafast speed of this process is as surprising as the finding that the sequence of subprocesses develops almost automatically.

We have shown that the core reversal is not related to the vortex resonance and predicted that it can be triggered by means of ultrafast unipolar field pulses. This has been confirmed experimentally in a recent study [172]. The ultrafast nature of the core reversal however still remains to be investigated experimentally.

The pair-creation mediated vortex core reversal is comparable in scope with the precessional switching of the magnetization [30, 31]. Both are ultrafast reversals triggered by short field pulses perpendicular to the direction of the magnetization and characterized by a toggle switch operational mode. Moreover, they share common features: the possibility of switching the magnetization back and forth using suitably shaped unipolar pulses; the existence of a threshold field above which the switching occurs; and the occurrence of multiple reversals at

stronger fields. However, while the precessional switching exploits the demagnetizing field, leading to switching speeds of the order of 200 ps, the pair creation and annihilation processes are driven by the exchange field. The magnitude of this internal field is of the order of 100 T, which is about 100 times larger than the demagnetizing field, explaining the higher speed (40 ps) of the core reversal. The ultrafast core reversal therefore represents a further step towards reaching the fundamental limit of field-induced switching. An additional advantage of the vortex core reversal lies in the simplicity of the required sample and magnetic structure – vortices naturally form in submicron-sized magnetic disks.

In summary,

- We have presented a novel nanomagnetic switching mechanism: the reversal of the vortex core. This reversal is mediated by the creation of a new vortex-antivortex pair in the vicinity of the existing core and the subsequent annihilation of the new antivortex with the original vortex.
- Unfolding over about 40 ps, the vortex core reversal represents *the fastest field-induced reversal mechanism* known to date.
- Our simulations provide detailed predictions, some of which have already been confirmed experimentally, showing the predictive power of micromagnetic simulations.

# 6

# Ultrafast antivortex dynamics[1]

The study of the ultrafast *vortex* dynamics presented in the preceding chapter has shown that the antivortex plays a decisive role in the mechanism leading to the reversal of the vortex core. Experimental studies by Neudert *et al.* on cross-tie walls indicate that antivortices play an equally important role as vortices in magnetization dynamics. The authors investigated the dynamic behavior of cross-tie walls in micron-sized Permalloy samples using time-resolved Kerr microscopy. They reported the creation of new cross-ties, *i.e.* of vortex-antivortex pairs in response to high-frequency fields [179] and to nanosecond field pulses [180] applied in the plane of the samples.

The dynamics of antivortices has however generally been investigated in less detail, probably because they always occur alongside vortices, forming cross-tie configurations exhibiting rather complex dynamics. Recently, the dynamics of a single cross-tie was investigated by Kuepper *et al.* by means of time resolved x-ray microscopy (PEEM) [181] in response to sub-nanosecond, low intensity magnetic field pulses. It was found that the interaction between the two vortices and the antivortex can lead to a reduction in the amplitude of the antivortex gyration, and even the inversion of its rotation direction with respect to its gyrocoupling vector, depending on the relative core orientations.

The next logical step is therefore to investigate the dynamics of a *single antivortex*. The *static* observation of an isolated antivortex was reported by Shigeto *et al.* [94] using magnetic force microscopy. Subsequently, micromagnetic simulations were used in Ref. [182], to investigate the gyrotropic motion of an isolated antivortex, as well as higher frequency magnetostatic modes, analogous to those found in vortices (see section 4.1.4).

The dynamic studies carried out on antivortices have so far focused on small perturbations from equilibrium produced by external fields. The question we investigate in the present chapter is:

- How does an *isolated antivortex* respond to ultrashort field pulses?

Our simulations show that the dynamics of an isolated antivortex can be char-

[1]The material in this chapter is based on *S. Gliga, M. Yan, R. Hertel, and C. M. Schneider, Phys. Rev. B* **77**, *060404(R) (2008)* and *S. Gliga, R. Hertel, and C. M. Schneider, J. Appl. Phys.* **103**, *07B115 (2008)*.

acterized by the production of a short-lived antivortex-vortex pair, followed by an annihilation process. These processes are thus complementary to the studied vortex response and equally lead to the reversal of the magnetization of the antivortex core. The reversal also results in the production of spin wave bursts. We show that the antivortex structure can therefore be used for the effective generation and propagation of spin waves that can drive novel logic circuits, such as described for example in Ref. [183]. We further investigate the stability of the antivortex structure and attempt to experimentally stabilize a single antivortex.

## 6.1 Antivortex preparation

Unlike vortices, which automatically form in disks of a certain size [83], it is rather difficult to isolate an antivortex, *i.e.* to prepare a nanostructure that only contains a single antivortex. This was achieved experimentally by Shigeto *et al.* using Permalloy thin-film elements consisting of four connected rings [94]. The antivortex was observed at the ring junction. Here, to stabilize an isolated antivortex, we use like in Ref. [182] a sample whose shape corresponds to the connecting part of four adjacent rings, as shown in Fig. 6.1. Our sample is constructed from four circular segments of radius 200 nm. It is discretized into 197 232 tetrahedral elements, with an average distance of 4 nm between discretization points. The four short stretching strips are 40 nm wide and 20 nm thick. The antivortex was obtained by saturating the sample perpendicularly to the plane and then letting the magnetization relax via minimization of the total energy. The in-plane shape anisotropy of this particular geometry sustains an antivortex due to the tendency of the magnetization to align with the sample boundaries. The antivortex is however not the only possible magnetization state: by using dynamic relaxation methods, we also observe the formation of a metastable vortex state. The lowest-energy configuration is formed by two domain walls. These are discussed in section 6.3.

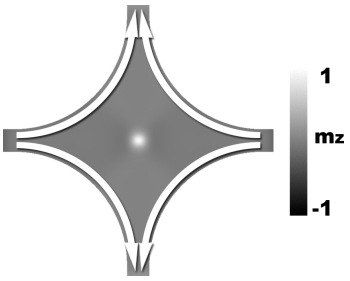


Figure 6.1: Modeled sample used to stabilize a single antivortex. The white arrows indicate the direction of the magnetization along the boundaries. The color scale represents the out-of-plane magnetization. The white dot is the antivortex core.

The material parameters used in the simulations are those of polycrystalline Permalloy: $A = 13\,\mathrm{pJ/m}$ (exchange constant), $\mu_0 M_\mathrm{s} = 1.0\,\mathrm{T}$ (with $M_s$ the saturation magnetization), $K$=0 (anisotropy constant) and $K_s = 0.0001$ J/m$^2$ (surface anisotropy) [175]. The magnetization dynamics was calculated using the Landau-Lifshitz-Gilbert equation with damping parameter $\alpha = 0.01$.

## 6.2 Field-induced dynamics

In the following section, the dynamics of the antivortex is studied in response to a short in-plane Gaussian-shaped pulse, as shown in Fig. 6.2. The pulse has a maximum strength of 60 mT and a duration $\sigma$=80 ps. The evolution of the magnetization in the core region is shown by visualizing the in-plane magnetization (left column of Fig 6.2) and by using the same isosurface representation as in the previous chapter (Fig 6.2, right column).

After the field pulse is applied, the antivortex is displaced from its equilibrium position, resulting in the strong distortion of the in-plane magnetization. This distortion is shown in Fig. 6.2, 20 ps after the pulse maximum. In the vicinity of the core the magnetization rotates out of the plane in the direction opposite to the antivortex core, analogous to the dip formation in a distorted vortex. Approximately 80 ps after the pulse maximum, a *new* antivortex is emitted from the original antivortex. The conservation of the total winding number requires that a vortex is also produced, which is found between the two antivortex structures. The newly formed antivortex-vortex pair is visible from the two additional intersections of the $m_x = 0$ and $m_y = 0$ isosurfaces. This strongly inhomogeneous structure is eventually resolved through the annihilation of the initial antivortex with the newly created vortex, which is oppositely polarized. The newly formed antivortex is left behind and has its core pointing in the opposite direction (shown at 140 ps).

The production of an antivortex-vortex pair from an antivortex structure is a previously unreported micromagnetic process. The resulting transient magnetic configuration can be considered an *anti cross-tie wall* – a single vortex enclosed by two antivortices which is never observed at static equilibrium. It is also striking that, in spite of their different magnetic in-plane structures, the ultrafast dynamics of vortices and antivortices are analogous, involving the creation of new magnetic structures followed by a destruction process. Here, the strength of the isosurface representation is obvious: it captures the main features of the processes unfolding in both vortices and antivortices, demonstrating their complementarity.

## 6.3 Antivortex stability

In Fig. 6.2, following the excitation, the system relaxes back to an antivortex structure. However, for stronger pulses, we observe that a vortex can nucleate at the sample edges. This nucleation process is visualized in Fig. 6.3 for two field pulse strengths, using the $m_x = 0$ and $m_y = 0$ isosurfaces. For a pulse of 60 mT, only an antivortex-vortex pair is produced (Fig. 6.3a). At 80 mT however, the isosurfaces additionally cross at the boundary, indicating that a vortex has nucleated (Fig. 6.3b). The distance between this vortex and the pair is large enough that the orientation of its core is independent of the polarization of the pair. Fig. 6.3 also shows that the isosurfaces are perpendicular to the sample edges, a result of the Rado-Wertmann boundary condition for the

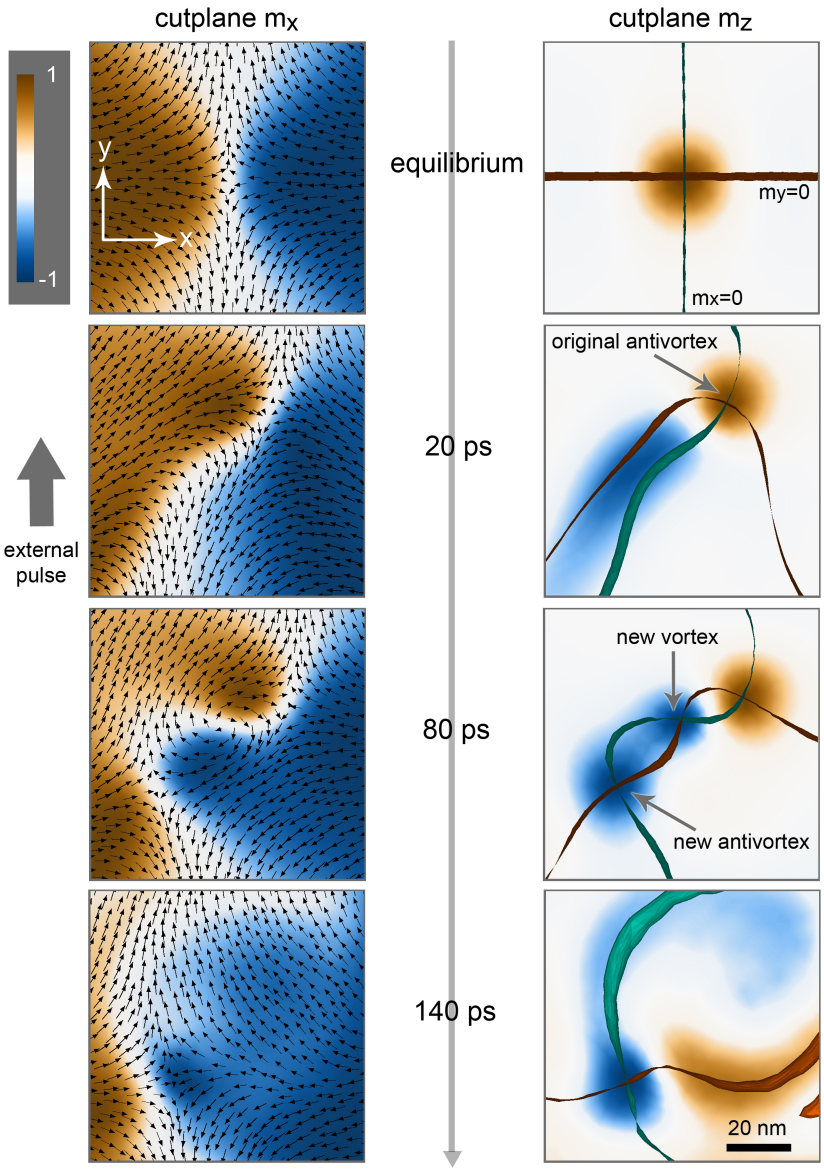


Figure 6.2: Antivortex dynamics induced by an ultrafast in-plane field pulse. The frames are snapshots of the region around the core at different times relative to the applied field's maximum. In the **left column**, the arrows represent the in-plane magnetization and the colors its component along the x axis. The colors in the **right column** quantify the out-of-plane component of the magnetization in the same region, while the green and red ribbons are the $m_x = 0$ and $m_y = 0$ isosurfaces.

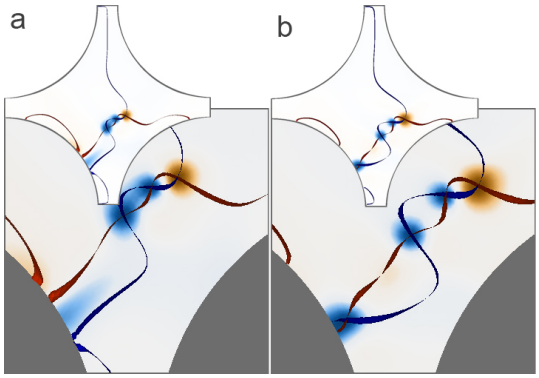


Figure 6.3: Vortex nucleation at the sample edges during the antivortex core reversal process. **a**, For a Gaussian pulse of 60 mT and 80 ps duration, no edge nucleation occurs. **b**, For a stronger pulse (80 mT) of the same duration, the $m_x = 0$ and $m_y = 0$ isosurfaces cross at the sample boundary, indicating the nucleation of a vortex. The colormap represents the out-of-plane component of the magnetization, as in Fig. 6.2.

exchange energy: $\frac{d\boldsymbol{m}}{d\boldsymbol{n}}\big|_{\partial S} = \mathbf{0}$, where $\boldsymbol{n}$ is the unit vector normal to the surface $\partial S$ [124]. The magnetization gradient is therefore non-vanishing only along a direction parallel to the sample edges. Since isosurfaces and gradient lines are perpendicular to each other [184, 185], the $m_x = 0$ and $m_y = 0$ isosurfaces are always perpendicular to the sample edges[2].

The introduction of a vortex in the sample affects the dynamics of the antivortex and thus also the final equilibrium of the structure. The different possible final states are shown in Fig. 6.4 as a function of the applied pulse's strength and duration. The diagram indicates that while it is rather difficult to isolate an antivortex, it is easy to dissolve it. Starting with low and short field pulses, we find that there is a set of parameters for which the system is slightly excited, causing the antivortex core to gyrate about its equilibrium position (white region). This motion was investigated in Ref. [182]. When the core switch occurs, the system relaxes into an antivortex configuration for a rather narrow set of field pulse parameters (green area). For stronger or longer pulses, vortex nucleation occurs at the same time as the antivortex core reversal, as illustrated in Fig. 6.3. The vortex can then migrate through the sample, leading to the expulsion of the antivortex after a few ns (orange area). In the blue area, for pulses above 60 mT, the pulse is sufficiently strong to induce the production of new pairs originating from *both* the antivortex and the nucleated vortex. The result is the generation of a transient state containing multiple cross-ties. This triggers a series of annihilations in which the initial antivortex and the nucleated vortex are dissolved. The final magnetic configuration is then a pair of head-to-head and tail-to-tail domain walls.

The strong dependence of the final magnetization state on the excitation

[2]Here, we do not take into account the Rado-Wertmann boundary condition for surface anisotropy. The value of surface anisotropy is indeed small (see section 6.1) and does not play a significant role in the dynamics, as determined in section 5.4.

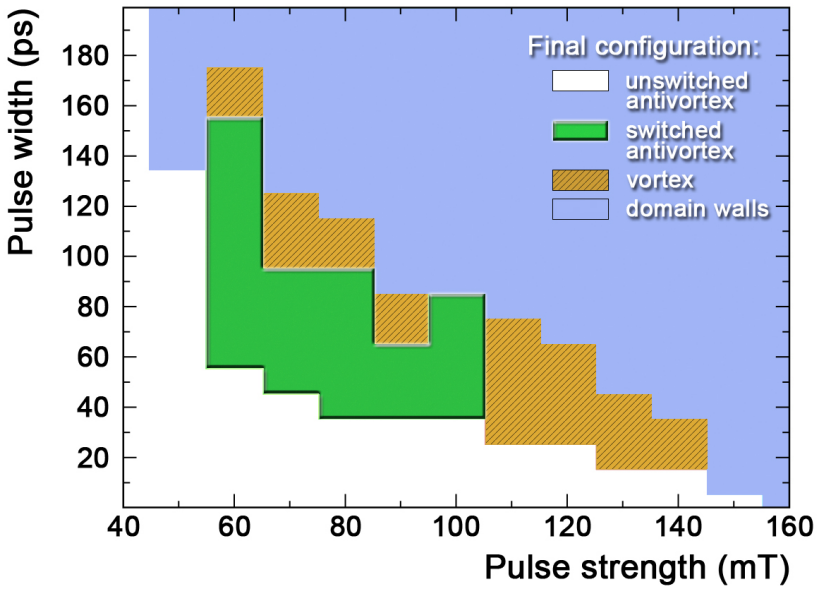


Figure 6.4: Final magnetic configuration in the astroid-shaped sample (Fig. 6.1), as a function of the applied field pulse strength and duration. The pulse duration is defined as the width $\sigma$ of the Gaussian. In the diagram, the duration is varied in increments of 10 ps, while the pulse strength is varied in steps of 10 mT.

parameters underlines the metastable character of the isolated antivortex structure. In an attempt to avoid vortex nucleation and thus increase the antivortex stability, notches are added to the sample, as shown in Fig. 6.5a. Such notches have been shown to repel vortex walls in thin-film elements [186]. In this case however, the notches seem to facilitate the nucleation of a vortex.

The weak stability of the antivortex can be explained by the presence of regions in the sample where the magnetization diverges, creating a volume charge density $\rho = -\mu_0 M_s(\boldsymbol{\nabla} \cdot \boldsymbol{m})$. At the branch extremities, where the magnetization is perpendicular to the sample boundary, surface charge densities $\sigma = \mu_0 M_s(\boldsymbol{n} \cdot \boldsymbol{m})$ are also present. The magnetic flux in the sample is therefore open, giving rise to the stray field shown in Fig. 6.5b. The computation of the stray field is preformed following section 5.2.2 by defining a region of air around the sample. It can be noticed that in each one of the loops, the flux circulates in a different direction, such that these flux closure loops can be considered as *virtual* vortices, *i.e.* vortices whose center is located outside the sample. Because they are close to the sample boundary, these virtual structures can easily enter the sample and nucleate a vortex, as in Fig 6.3. In contrast,

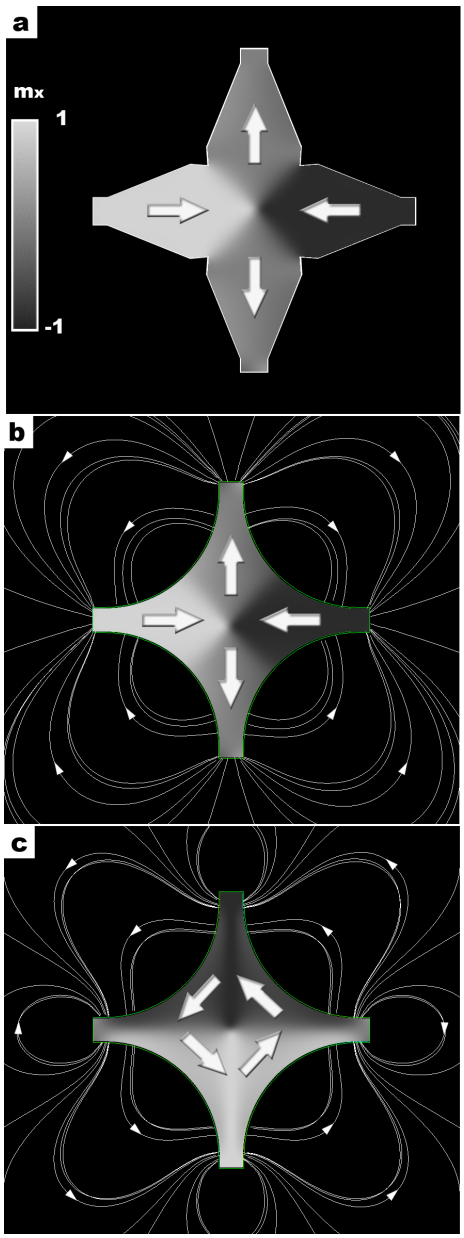


Figure 6.5: Antivortex stability. **a**, Modified sample with four notches located at the sites where a vortex tends to nucleate. The thick white arrows indicate the direction of the in-plane magnetization in the sample. The black and white scale quantifies the x component of the magnetization. **b**, Stray field of an antivortex. The flux does not circulate in the same direction in each loop, giving rise to virtual vortices around the structure. **c**, Stray field generated by a vortex: the flux circulates in a single direction around the structure.

Fig. 6.5c shows the demagnetizing field of a sample containing a vortex. In this case, the flux lines loop around the single central vortex structure, lending greater stability to the configuration.

## 6.4 Experimental investigation

Based on the above results, a sample is designed to improve the stability of the antivortex. The idea consists of surrounding the astroid-shaped region in Fig. 6.1 by magnetic material in order to stabilize the virtual vortices surrounding the antivortex, thereby stabilizing the antivortex structure itself. The sample consists of four circular segments cut out within a square, thus creating an astroid shape surrounded by four quadrants. For this purpose, 30 nm thick nanocrystalline Cobalt thin-film samples with very low anisotropy were prepared. The pattern in Fig. 6.7 was cut out *in situ* by means of focused ion beam (FIB) lithography using Ga ions. The effective spacing between the elements is about 50 nm. The samples were prepared by S. Cherifi from the Institut NÉEL in Grenoble, who performed the measurements with J. Mennig using spin-polarized scanning electron microscopy (SEMPA) at the Institute of Solid State Research (IFF 9) at the Forschungszentrum Jülich. In SEMPA, an unpolarized focused electron beam is used to stimulate the emission of spin-polarized secondary electrons. The analysis of the spin-polarization of the secondary electrons allows the local magnetization to be determined. The entire sample is scanned by moving the focused electron beam over the surface.

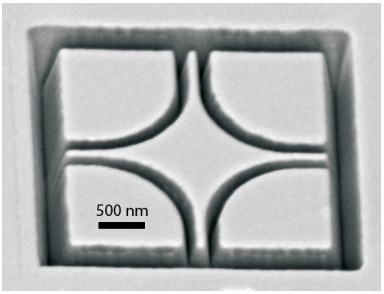


Figure 6.7: Sample fabricated for the experimental investigation of an isolated antivortex. The four circular segments were obtained by FIB in a 30 nm thick Co sample.

One of the experimentally observed structures is shown in Fig. 6.6a, where the magnetic contrast along both the $x$ and $y$ directions is used to reconstruct the in-plane magnetization distribution. While vortices are indeed stabilized around the astroid, the structure present at the center of the sample is not an antivortex, but rather a *vortex*. In Fig. 6.6b, we show our simulations of a vortex state in a similar geometry, which are directly comparable to the measurements. The contrast generated if an antivortex structure was present are shown in Fig. 6.6c. Clearly, the vortex and the antivortex states look very similar, hence the necessity of considering both components of the in-plane magnetization in determining the imaged structure. In Fig. 6.6d, the contrasts generated by a magnetization state consisting of a head-to-head and a tail-to-tail domain wall are displayed.

It therefore appears that other structures must be conceived, in order to

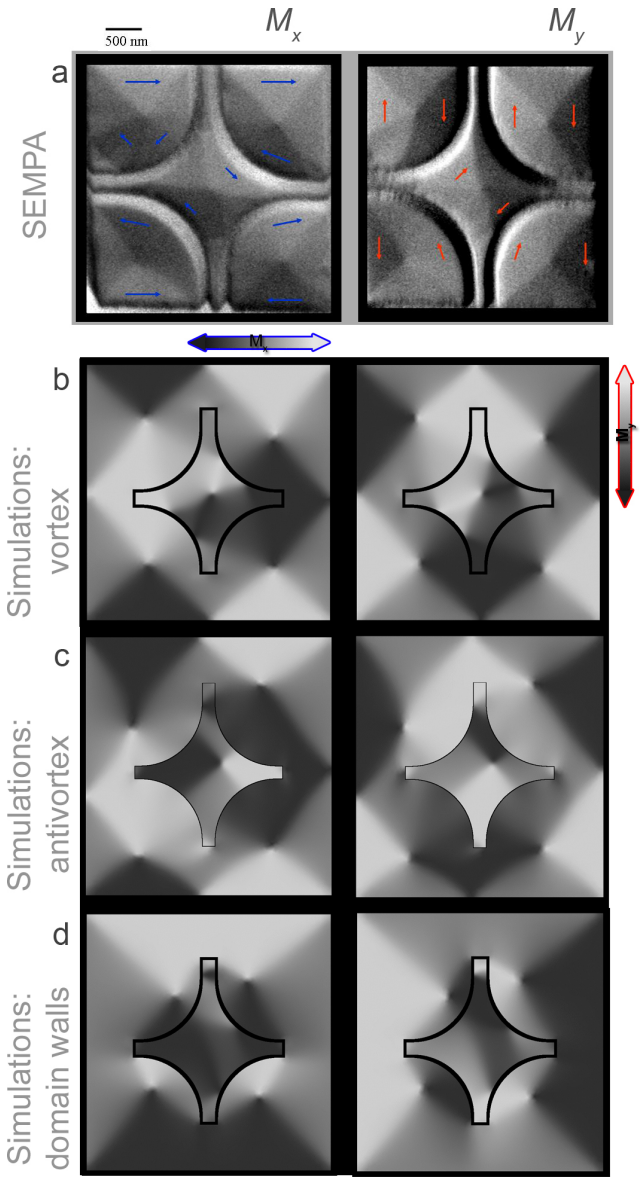


Figure 6.6: Experimental observation of the magnetic structure in a patterned Co thin film using SEMPA. **a**, The measurements reveal that a vortex pattern forms in the central region of the sample. On the left image, the x component of the magnetization is shown. The y component is shown on the right image. **b**, Simulated vortex structure. The colormap indicates, like above, the x and y components of the magnetization. **c**, Simulated antivortex structure. **d**, Simulated state containing a head-to-head and a tail-to-tail domain wall. The tail-to-tail wall is visible in the upper part of the astroid structure, whereas a head-to-head wall is visible in its lower part.

stabilize an antivortex. For example, MFM measurements reported in Ref. [187] revealed the presence of antivortices in sub-nanometer rings. Also, a "clover leaf" shape was used by Shigeto *et al.* [94] as well as in the simulations presented in Ref. [188].

## 6.5 Spin wave generation

Spin wave-based logic circuits represent a novel concept for building magnetic circuits compatible with conventional electronic devices. In this concept, the information is carried by the spin wave phase and is manipulated through its interaction with different types of domain walls [46]. Logical functionality is achieved by exploiting wave superposition. The spin wave bursts produced following the antivortex core reversal could therefore be used to inject spin waves into a strip acting as a waveguide, thereby acting as a wave source for such circuits.

It has been suggested in Ref. [164] that the core reversal of a *vortex* could be used for spin wave generation. The proposed geometry consists of connecting to a nanodisk in a vortex state, a strip along which the spin waves can propagate. In such a geometry, however, a 90° Néel wall is inevitably present between the source and the strip. Such domain walls have been reported to hinder spin wave propagation, mostly by reflecting them [189]. An antivortex would therefore be more suitable than a vortex to act as a source of spin waves: in contrast to the vortex, the spin waves produced in the antivortex can propagate unhindered into a branch, which naturally extends the magnetic configuration of the sample, as shown in Fig. 6.8. In principle, all the branches can be extended in order to connect to neighboring antivortex elements. Such a network could for example be achieved within an antidot array [190] and provide a regular array of antivortices.

## 6.6 Summary

In this chapter we presented the complex modifications undergone by an antivortex in response to ultrashort field pulses. We found that the static topological complementarity of vortices and antivortices is exhibited equally in their ultrafast dynamic behavior. Indeed, short pulses can trigger the reversal of the antivortex core, which occurs through a rapid sequence of pair creation and annihilation processes, namely the creation of a new antivortex and the annihilation of the original one with a short-lived vortex. This represents a novel fundamental process in magnetism on the nanoscale.

Our investigations were carried out by isolating the antivortex structure in a specially-tailored sample. However, using SEMPA, we showed that experimentally isolating an antivortex is rather difficult. Moreover, while antivortices possess rich and complex dynamics, the limits of their stability require an excellent control of the exciting field parameters in order to avoid modifying the in-plane

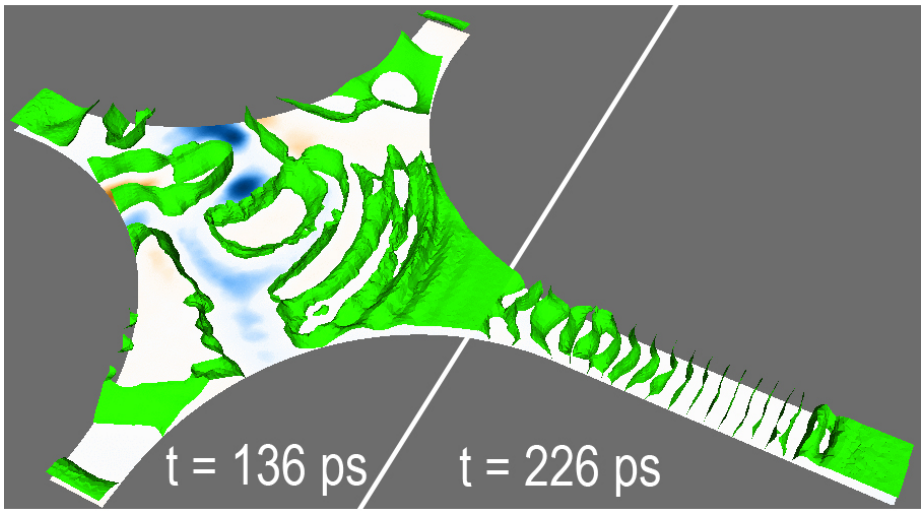


Figure 6.8: Spin wave production and propagation using an antivortex structure. The spin waves are produced following the reversal of the antivortex core and their propagation is shown at 136 ps and at 226 ps following the pulse maximum (pulse parameters: 60 mT, 80 ps). These propagate smoothly into the extended branch. The $m_z = 0$ isosurface is represented in green, allowing visualization of the wave fronts. The blue spot represents the switched core.

magnetic structure. If the antivortex stability can be increased, however, the annihilation of transient magnetic structures during the switching process could be used to generate spin waves for novel logical circuits.

Our results also indicate that antivortices play an equally important role as vortices in the dynamics of cross-tie domain walls. The pulse-induced dynamic transformations of cross-ties and the formation of new magnetization patterns observed in Refs. [180, 179] therefore likely result from pair creation and annihilation processes triggered equally by vortices and antivortices.

In summary,

- The ultrafast dynamics of antivortices in response to short and strong in-plane field pulses is characterized by the emission of a new antivortex and the annihilation of the original one with a transient vortex. These processes lead to the reversal of the antivortex core and are *complementary* to the ultrafast response of vortices.
- The antivortex structure is intrinsically metastable and can difficultly be isolated.
- The ultrafast core reversal of the antivortex could be used for the generation and propagation of spin waves.

# 7

# Current-induced vortex core reversal

Up to now, the investigated magnetization dynamics was triggered by magnetic fields. The control of the magnetization dynamics on increasingly smaller scales by means of external fields however presents two important challenges. First, the required fields for switching the magnetization become larger as the lateral dimensions of the magnetic structures decrease. Second, magnetic fields are difficult to focus in order to address small individual elements. This is a problem, notably for magnetic devices in which nanoelements are patterned in dense arrays. Schemes have therefore been developed which allow to selectively switch single elements for example in magnetoresistive random access memories (MRAM) [191, 192]. The long-range nature of the dipolar field however practically limits the applicability of such implementations. In this context, the spin transfer torque effect [51, 52] presents a promising alternative for controlling the magnetization in nanoelements.

In this chapter, we therefore investigate vortex dynamics driven by spin-polarized electric currents. First, we analytically describe the electric excitation of vortices. Theoretical and experimental studies [193, 45, 194] have indeed shown that the gyrotropic mode of the vortex can be excited by spin polarized currents. Moreover, similar to the field-induced core switch, Yamada *et al.* [57] have experimentally demonstrated that the core orientation can be reversed by exciting the gyrotropic mode of the vortex using a sinusoidal electric current tuned to the resonant frequency of the vortex. The micromagnetic mechanism leading to the core reversal in such *resonant switching* was however not resolved. Second, we therefore briefly describe the resonant core reversal, focusing on its switching mechanism. Third, we consider the question:

- Can the vortex polarization be reversed by means of a single, short in-plane electric pulse?

We demonstrate that it is indeed possible and that this *non-resonant* electrical switching pathway leads to considerably faster reversal times. This allows solving the selectivity problem in dense arrays of vortices and enables in principle the direct integration of vortex-based nanoelements in electronic circuits.

## 7.1 Vortex dynamics induced by a spin-polarized current

We start by describing the Thiele equation, extended to take into account the influence of a spin-polarized current and its implications for vortex motion. Considering the drift velocity of the electron spins $\boldsymbol{u}$ defined in (2.50), the force $\boldsymbol{F}_{\mathrm{STT}}$ exerted on the vortex by the spin-polarized current is of the form [195, 193]

$$\boldsymbol{F}_{\mathrm{STT}} = -\boldsymbol{G} \times \boldsymbol{u}, \tag{7.1}$$

where $\boldsymbol{G}$ is the gyrocoupling vector (4.15). The Thiele equation then reads [56, 193, 196]:

$$-\kappa \boldsymbol{X} + \boldsymbol{G} \times (\boldsymbol{v} - \boldsymbol{u}) + \underline{\underline{\boldsymbol{D}}} \cdot (\alpha \boldsymbol{v} - \beta \boldsymbol{u}) = 0. \tag{7.2}$$

The dimensionless coefficient $\beta$ is the degree of non-adiabaticity of the spin-current introduced in section 2.3.2 and is of the order of $10^{-2}$ [56], *i.e.*, comparable in magnitude to $\alpha$. The expression for the damping term reflects the fact that the current can enhance or decrease the magnetic damping. We also note that for small displacements when the potential $-\kappa \boldsymbol{X}^2/2$ can be neglected, we get $\boldsymbol{v} = \boldsymbol{u}$ when $\alpha = \beta$. The vortex displacement then occurs along the direction of motion of the electrons [196]. Thus, unlike in a magnetic field (4.38), the current-induced vortex displacement is independent of the vorticity. This represents an additional advantage of current-induced dynamics over field-induced dynamics since the sense of circulation of the in-plane magnetization is difficult to control [197, 198]. For larger displacements, when the restoring force $-\kappa \mathbf{X}$ balances the current-induced force however, the vortex motion becomes perpendicular to the current direction. The resulting gyrotropic motion is then determined by the gyrocoupling vector, as described in chapter 4. It has been noted [193] that in contrast to domain wall dynamics [108], no threshold current is required to induce the vortex motion in the absence of extrinsic pinning and that the maximal displacement velocity of the vortex is proportional to the current density $J$.

Experimental evidence for the excitation of the gyrotropic motion of the vortex by means of direct and alternating spin-polarized currents was given in Refs. [45, 194, 199]. For example in Ref. [45], Kasai *et al.* used magnetoresistance measurements to determine the resonant frequency of an electrically excited vortex.

## 7.2 Core reversal triggered by an alternating current

Similarly, Yamada *et al.* [57] resonantly excited a vortex in Permalloy submicron disks using increasing current densities. The initial and final polarizations of the vortex for each current density were measured with MFM, allowing to experimentally establish the critical current at which the electric switching of the vortex core occurs. Because MFM is a static imaging method, the reversal mechanism in this case could not be determined.

In order to understand this mechanism, we investigate here the vortex response to a resonant excitation. The time evolution of the magnetization is obtained from the Landau-Lifshitz-Gilbert equation including the adiabatic (2.48) and non-adiabatic (2.49) spin torque terms. The dynamics is computed in the same disk-shaped Permalloy sample used in section 5.2 (200 nm diameter, 20 nm thickness with a distance of about 3 nm between discretization points). The polarization is set to $P = 0.7$ [200] with the non-adiabatic parameter $\beta = 0.02$ [56] and damping factor $\alpha = 0.01$.

The resonant frequency $\omega_0$ of the vortex in our sample is determined by first displacing it from its equilibrium position and then following its trajectory as it relaxes. From Fig. 7.1 we thus find $\omega_0 = 776$ MHz, in agreement with the value predicted by equation (4.32) of 779 MHz. An in-plane alternating current of the form $j(t) = J\sin(\omega_0 t)$ is then applied to excite the vortex. For this study, a uniform current density distribution is assumed throughout the sample. Also, the influence of the Oersted field is not considered: indeed, this field's contributions at the top and bottom surfaces of our thin sample mostly cancel out. At the same time, along the edges of the sample we calculate that the strength of the Oersted field is of only about 20–30 mT, which is not sufficient to induce significant distortions of the magnetization along the vortex thickness. Exciting the vortex with increasing current densities, we find that a minimum current density of $J = 4 \times 10^{11}$ A/m$^2$ is necessary in order to reverse the core. This reversal occurs approximately 14 ns after the current is turned on. Increasing $J$ causes a steep decrease of the switching time, as shown in Fig. 7.2.

Our simulations further show that the reversal mechanism is independent of the current density and that it is in fact identical to the one found in the field-driven case. Fig. 7.3 shows the steps leading to the reversal of the core induced by an alternating current with $J = 1.2 \times 10^{12}$ A/m$^2$. Once again the $m_x = 0$ and $m_y = 0$ isosurfaces are used to locate the position of the vortex core. Initially, the radius of the vortex motion increases until it reaches a stable orbit. After 2900 ps, the structure of the gyrating core is heavily distorted, causing the formation of a pronounced dip in its vicinity. At $t = 2992$ ps, this results in the

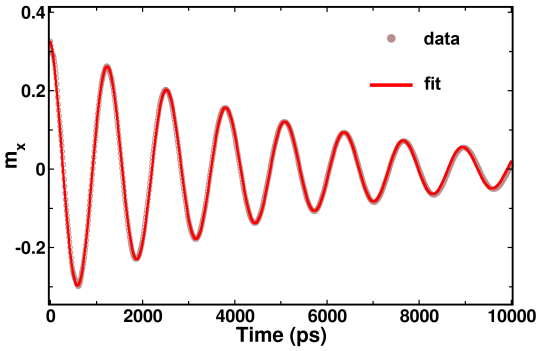


Figure 7.1: Oscillation of the volume-averaged x component of the magnetization during the dynamic relaxation of the vortex ($\alpha = 0.03$). The fit the to the data yields a resonance frequency of 776 MHz.

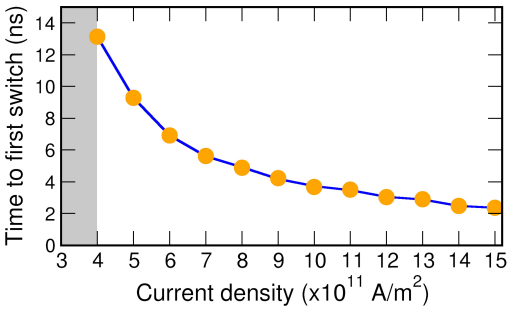


Figure 7.2: Switching time of the core from the moment an electric current is applied as a function of the resonant current density. The grey shaded region indicates where the current density is too low to trigger the switch.

creation of an oppositely polarized vortex-antivortex pair. The original vortex is in this case very close to the edge of the sample, leading to the distortion of its in-plane structure. At the same time, the magnetization at the sample boundary is not aligned with the edges anymore, resulting in surface charges. The newly formed vortex and the oppositely polarized antivortex annihilate within approximately 10 ps, leaving behind a single vortex core with opposite polarization. The core reversal mechanism thus unfolds over the same ultrashort timescale found in chapter 5.

Following the switch, the vortex gyrates in the opposite direction. After a few ns the core reverses again, thereby periodically alternating between opposite polarizations as long as a current is applied.

Next, we verify the influence of the damping constant $\alpha$ on the current density $J$ required to switch the core. Fig. 7.4 reveals a power function dependence of the form $J_{\text{switch}} = 150\,[\text{A/m}^2] \times \alpha^{0.81}$ (best fit to the data). From the fit, we deduce that an amplitude of $J \simeq 2 \times 10^{11}$ A/m$^2$ is necessary for the alternating current to trigger the core switch when $\alpha = 0$. We note that the effective damping of the vortex is determined by the values of $u$ and $\beta$ according to equation (7.2).

## 7.3 Core reversal induced by short current pulses[2]

We demonstrate here that the core reversal can equally be triggered by short *non-resonant* in-plane current pulses, similar to the field-pulse-induced core reversal studied in chapter 5. In contrast to resonant switching where the core orientation periodically reverses as long as the oscillatory current is applied, reversing the core by means of single pulses allows to precisely control its orientation.

To this effect, we apply short Gaussian pulses of varying strengths and using a damping of $\alpha = 0.03$. The pulses have a width $\sigma = 100$ ps. To trigger the core reversal, we find that the amplitude of the pulses must exceed

[2]This section is based on *Y. Liu, S. Gliga, R. Hertel, and C. M. Schneider, Appl. Phys. Lett.* **91**, *112501 (2007).*

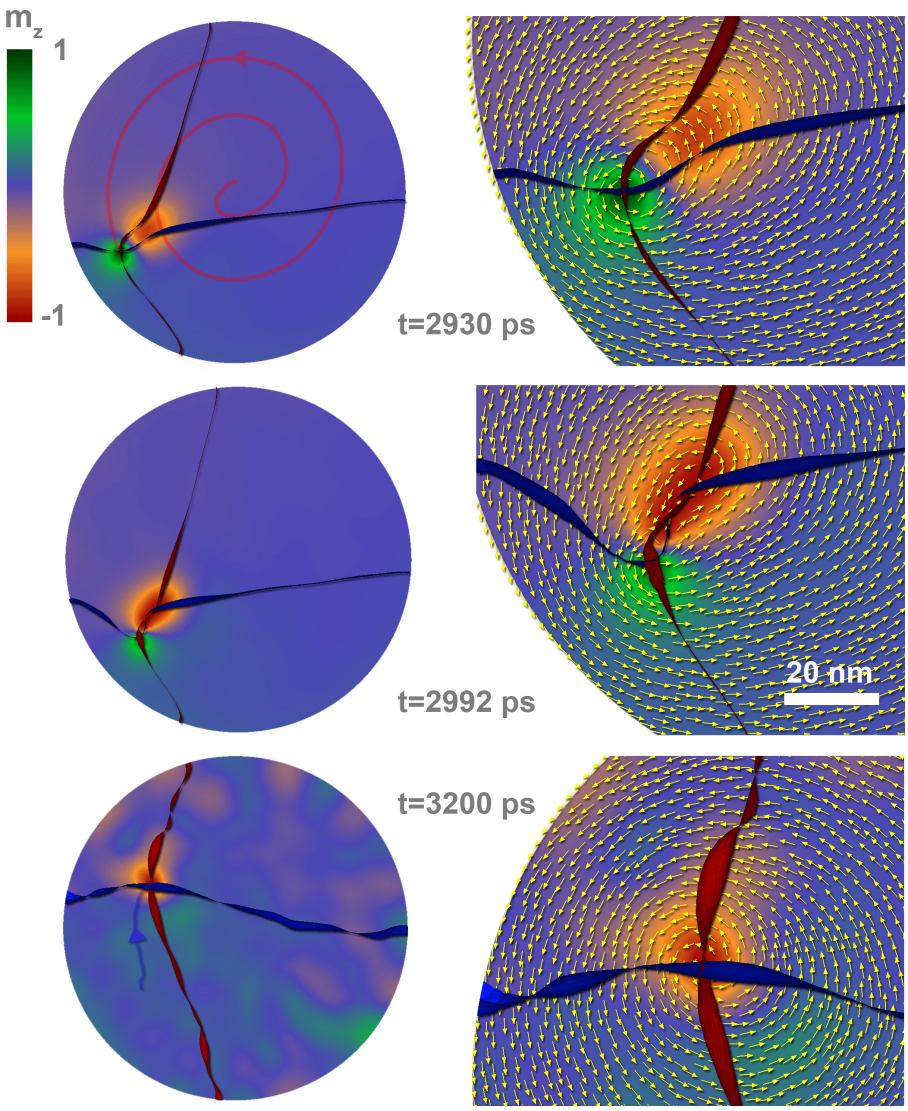


Figure 7.3: Steps leading to the reversal of the vortex core in response to a resonant spin-polarized current with $J = 1.2 \times 10^{12}$ A/m$^2$. The blue and red ribbons respectively represent the $m_x = 0$ and $m_y = 0$ isosurfaces. The colors represent the z-component of the magnetization. In the **right** column, the vortex trajectory is highlighted, while the **left** column shows a zoom on the pair formation. The arrows represent the in-plane magnetization. About 2930 ps following the application of the current, the dip has a pronouced out-of-plane component: $m_z = 0.8$. At $t = 2992$ ps, a new vortex-antivortex pair is formed. At the same time the distortion of the in-plane structure of the initial vortex is apparent in the vicinity of the sample edge. At $t = 3200$ ps, the new vortex with reversed polarization gyrates in the opposite direction.

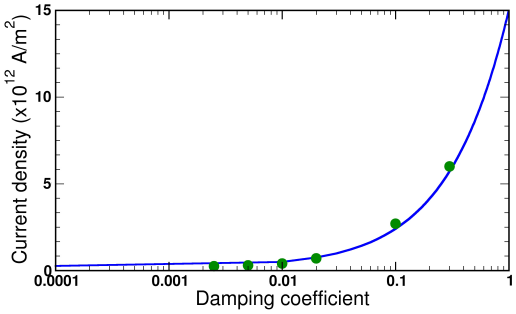


Figure 7.4: Evolution of the resonant current density amplitude required to trigger the core reversal as a function of the damping coefficient $\alpha$. The data (solid green circles) is fitted to a power function (blue line).

$J = 6.7 \times 10^{12}$ A/m$^2$. This is about an order of magnitude higher than the current densities required for the resonant switch. Although such a strong current might affect the structural stability of the sample if it was applied continuously, its effects should be small given that short pulses are being used. Following the application of the current pulse, the vortex is rapidly displaced in the direction of the electron flow (as expected when $\alpha \sim \beta$). We find that the micromagnetic reversal process is again the same: the in-plane magnetization of the vortex is heavily distorted leading to the creation of a pair, followed by a rapid annihilation within about 10–15 ps (Fig. 7.5).

In contrast to the resonant switch however, an increase in the current density does not only lead to faster switching, but also to *multiple switches*. These consist in a repeated series of vortex-antivortex pair creation and annihilation processes as observed in the case of the field-induced core reversal in section 5.3. Fig. 7.6a shows the time evolution of the average energy density during succes-

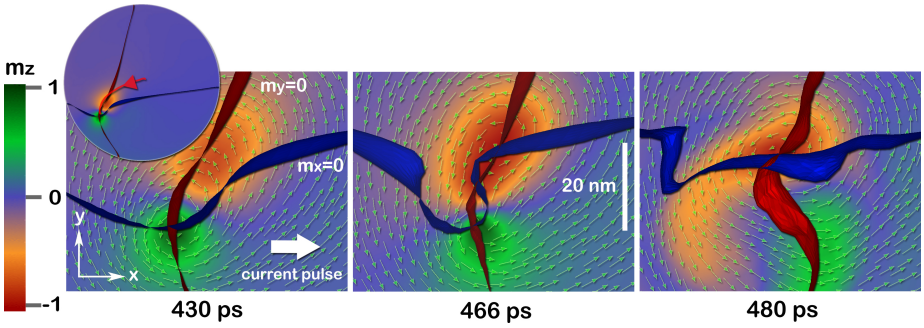


Figure 7.5: Core reversal in response to a Gaussian current pulse of $7.4 \times 10^{12}$ A/m$^2$ and a width $\sigma = 100$ ps. The vortex is rapidly shifted away from its equilibrium position in the direction of the electron flow, as shown in the inset. The evolution of the magnetization is then only shown for a small region around the core. The times are given with respect to the moment when the current pulse is applied. The arrows represent the in-plane magnetization and the isosurfaces are the same as in Fig. 7.3.

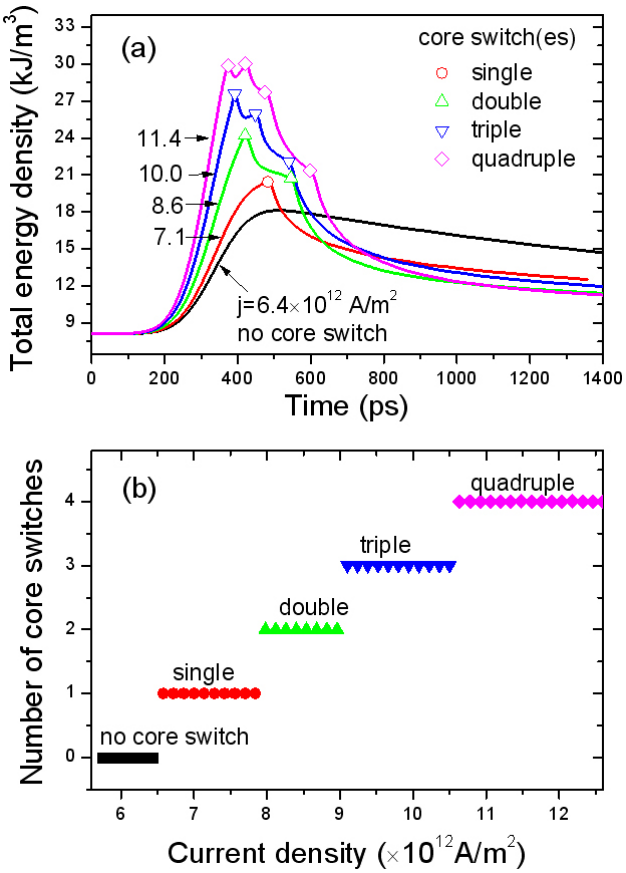


Figure 7.6: **a**, Average total internal energy density as a function of time for multiple core switches. The maximum strength of the current pulse is indicated next to each curve. **b**, Number of vortex core switches as a function of the applied current density.

sive reversals. Following each annihilation, the total energy rapidly decreases, as observed in section 5.4. In addition, it appears that as long as the total energy density is greater than a threshold value (*i.e.* the value when the first switch occurs for $J = 8.6 \times 10^{12}$ A/m$^2$), further switches occur. Here, a double core switch is obtained with current pulses of about $8.5 \times 10^{12}$ A/m$^2$, while triple and quadruple switches occur with pulses of $10 \times 10^{12}$ and $11 \times 10^{12}$ A/m$^2$, respectively. Ultimately, for very large currents (above $20 \times 10^{12}$ A/m$^2$), the vortex core is expelled from the sample. Fig. 7.6b shows the number of core switches as a function of the applied current's strength. Interestingly, the switching process appears to be "quantized", indicating that *a well defined energy is required to trigger the reversal mechanism.* This is explored in detail in chapter 8.

We additionally verify if the value of the non-adiabatic term $\beta$ or the spin-polarization of the current affect the reversal. In the case of domain walls for example, it has been shown [56] that dynamic characteristics such as pinning and the breakdown velocity (Walker limit) depend on the value of $\beta$. It turns out that neither parameter affects the vortex core switching process. In the

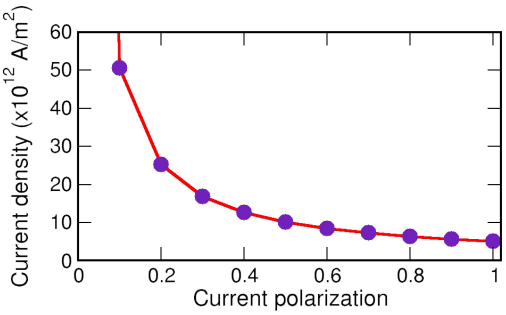


Figure 7.7: Current density required to trigger the vortex core reversal as a function of the polarization.

extreme case where $\beta = 0$ we find that the reversal is unaffected, suggesting that non-adiabatic processes do not play a significant role in this case. Concerning the current spin polarization, we observe that the current density required to trigger the switch is inversely proportional to the current polarization as shown in Fig. 7.7. Currents that are not spin-polarized do not trigger the reversal.

In a recent experimental study, Yamada *et al.* [201] have confirmed the possibility of switching the vortex core by means of single nanosecond-long current pulses of densities up to $1.3 \times 10^{12}$ A/m$^2$. The core polarization was determined from MFM scans taken before and after the pulses. We already noted in chapter 5.5 that the stroboscopic experiments of Weigand *et al.* [172] suggested how the core reversal is deterministic. The results of Yamada *et al.* however indicate that for low current densities close to the switching threshold the reversal probability is of only about 50%, possibly due to vortex pinning at defects. This suggests that an experimentally reproducible switch is only realizable well above the threshold current density (or field strength).

## 7.4 Summary: Resonant versus non-resonant switching

In this chapter, we have presented the possibility of electrically reversing the polarization of a magnetic vortex via *two distinct pathways*: by means of a resonant current and with short current pulses. We found that the magnetization reversal occurs through *the same mechanism in both cases*: it is mediated by a sequence of vortex-antivortex pair creation and annihilation events identical to the field-driven vortex. We found however that the time scales associated with these two pathways differ by an order of magnitude. Indeed, when the vortex is excited resonantly the core switch is triggered within approximately ten nanoseconds. In contrast, when the vortex is excited by means of short unipolar pulses the reversal is noticeably faster, occurring within a few hundreds of picoseconds. In addition, suitably-shaped pulses allow to precisely control of the core orientation, whereas the core orientation switches repeatedly when the vortex is excited at resonance. Another distinction between the two investi-

gated reversal pathways is the response of the vortex when the current density is increased. At resonance, an increase in the amplitude of the alternating current leads to a faster reversal while for non-resonant excitations stronger current densities lead to multiple switches.

We finally note that other methods for reversing the core have also been demonstrated in the literature, for example by means of DC currents [202] or using a single period of a resonant excitation [203]. The possibility of electrically controlling the polarization has led to novel concepts for magnetic random-access memories based on the orientation of the vortex core (VRAM) [204, 205].

In summary,

- We have investigated two distinct pathways leading to the vortex core reversal using spin-polarized electric currents. The first is based on the *resonant* excitation of the vortex, while the second is triggered by short and strong *non-resonant* pulses.
- While the switching times for these pathways differ by an order of magnitude, the underlying micromagnetic mechanism leading to the core switch is identical.
- The possibility of reversing the core with single current pulses represents a promising and reliable route to controlling the orientation of the core, which could be used in magnetic-based random-access memories.

# 8

# Energetic origin of the core switch

In the previous chapter, we showed that the micromagnetic process leading to the vortex core reversal is independent whether the triggering excitation is resonant or not. This indicates that the reversal has in fact a unique underlying origin. Thus, the reversal always unfolds over a fixed amount of time spanning approximately 40 ps. It is the *total* switching time, considered from the moment when the perturbation is applied, that strongly depends on the current parameters used to excite the vortex. This dependence can lead to a difference of an order of magnitude in the reversal time between the case when the vortex is excited resonantly, compared to when it is driven by single pulses. Based on these results, in this chapter we investigate the following questions:

- Which parameter controls the core reversal?
- What determines the time difference between the *resonant* and *non-resonant* reversals?
- How can the energy quantization of the switching process observed in the previous chapter be explained?

Recent experimental and theoretical studies have found that the core reversal occurs for a well-defined velocity of the vortex [57, 156, 203]. It has therefore been suggested that the core reversal is determined by the vortex velocity. In this case, the reversal should be a purely dynamic process that does not require overcoming an energy barrier [156]. An analogy was thus made [57] with the Walker velocity of domain walls at which the wall becomes unstable, leading to periodic changes in its structure [206, 207]. In the case of a vortex, the dynamic instability would lead to the reversal of the core. The source of the instability was assumed to be due to the gyrotropic field described in section 5.2.2.

The simulations presented in this thesis, however, have established that the dynamic deformation of the core is not driven by the gyrofield in the ultrafast case, but rather by the exchange field. Also, the core reversal is not the result of the breakdown of the vortex structure, but rather results from the creation of a new vortex-antivortex pair. In addition, velocity does not allow explaining the quantization we observed in Fig. 7.6, which seemed to be correlated to

specific values of the internal energy of the vortex. Finally, experimental measurements of the vortex core reversal velocity [37] show discrepancies with the values derived from theoretical calculations [156].

The interpretation in terms of velocity is thus incomplete. We therefore suggest here that rather than *velocity*, it is *energy* that determines the core reversal. Indeed, we previously found that the reversal is triggered by the production of a new vortex-antivortex pair. The production of pairs however can only described in the context of field theories [208]. We thus expect that vortex-antivortex pair production occurs, like charged pair production in quantum mechanics, once a well-defined *energy threshold* is reached.

In the following, the evolution of the internal energy of the vortex is studied during both the resonant and non-resonant switching pathways. Our analysis reveals that the core reversal is connected to a well-defined critical threshold value of the exchange energy. Remarkably, we find that this threshold is independent of the electric excitation parameters. We equally demonstrate that the threshold does not depend on intrinsic parameters such as the size of the vortex or the damping. This establishes the fundamental role played by the exchange energy in driving the switching process.

## 8.1 Core switch triggered at resonance

Throughout this chapter, the Permalloy disk-shaped sample described in section 7.2 is used. The damping constant is $\alpha = 0.01$, the surface anisotropy $K_s = 0.1$ mJ/m$^2$, the polarization $P = 0.7$ and the non-adiabatic factor is set to $\beta = 0.02$, as previously.

### 8.1.1 Energy evolution

We first consider the case when the vortex is driven by a resonant current $j(t) = J\sin(\omega_0 t)$. Its amplitude is set to $J = 1.2\times10^{12}$ A/m$^2$, like in section 7.2. The value of $\omega_0$ was previously found to be 776 MHz. Fig. 8.1 shows the time evolution of the exchange, demagnetizing and total volume-averaged energy densities of the vortex. Each switching event is distinguishable by a sharp increase in the exchange and total energy densities, followed by a sudden drop (the first switch occurs at 3 ns). Comparing the energy evolution to the evolution of the magnetization shown in Fig. 7.3, we notice that these increases correspond to the production of new vortex-antivortex pairs. In contrast, the increase in the demagnetizing energy density, which peaks about 100 ps before the exchange and total energy densities, is related to the formation of the pronounced oppositely magnetized dip in the vicinity of the core shown in Fig. 7.3 at $t = 2930$ ps. Once the pair is produced (yellow-colored area) the demagnetizing energy drops sharply. The pair annihilation which follows results in a sudden decrease in energy. The produced spin waves subsequently cause the observed oscillations of the demagnetizing and exchange energy densities.

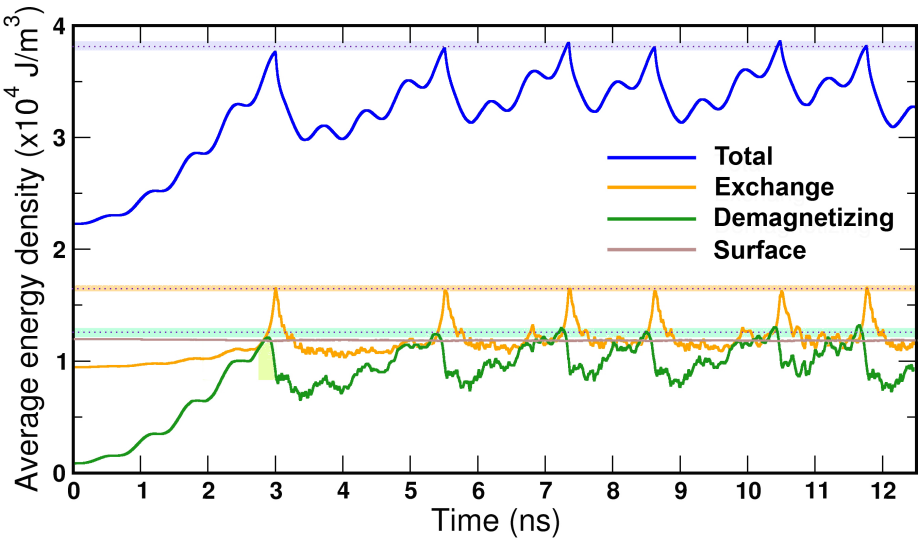


Figure 8.1: Evolution of the total and partial energy densities during the core reversal triggered by an alternating current of amplitude $J = 1.2 \times 10^{12}$ A/m$^2$. The dashed lines indicate the average energy values at the moment of the core switch and the color bands their standard deviation. The light shaded region highlights the decrease of the demagnetizing energy term during the formation of a new vortex-antivortex pair (only shown for the first switch). The total energy is the sum of the exchange, demagnetizing and surface terms.

Clearly, the core reversal occurs at *specific energy densities*. Analyzing the successive reversals over a period of 25 ns, we determine the threshold value $e_{\rm thr}$ of each energy density term and the variation in energy density with respect to the static equilibrium of the vortex $\Delta e_{\rm thr}$:

$$\begin{aligned} e_{\rm thr}^{\rm tot} &= (3.81 \pm 0.03) \times 10^4 \text{ J/m}^3, \quad \Delta e_{\rm thr}^{\rm tot} = (1.59 \pm 0.03) \times 10^4 \text{ J/m}^3 \\ e_{\rm thr}^{\rm exc} &= (1.65 \pm 0.02) \times 10^4 \text{ J/m}^3, \quad \Delta e_{\rm thr}^{\rm exc} = (0.70 \pm 0.02) \times 10^4 \text{ J/m}^3 \\ e_{\rm thr}^{\rm dem} &= (1.27 \pm 0.04) \times 10^4 \text{ J/m}^3, \quad \Delta e_{\rm thr}^{\rm dem} = (1.18 \pm 0.04) \times 10^4 \text{ J/m}^3. \end{aligned} \tag{8.1}$$

The indicated errors are the standard deviation of the computed averages. We mainly attribute these small variations of 1-3% to excitations caused by the spin waves. Minor variations can also be due to the discretization, as the successive switches occur at different regions of the irregular finite-element mesh.

On Fig. 8.1, we also show the evolution of the surface anisotropy energy density (grey line). Like in section 5.4, we find that it only shows a variation of approximately 2% over the entire 25 ns period. A close examination shows that this variation occurs during the switching process, certainly due to the dramatic variations in the magnetization, which take place. We performed simulations setting $K_s = 0$ and found that surface anisotropy does indeed not play any role

in the switching process[1].

We now consider the value of the threshold energy for pair formation. Given that the newly created vortex and antivortex structures are only a few nm apart, the exchange energy is dominant and the dipolar contribution to the total energy of the pair can therefore be neglected. The pair energy is then given by equation 4.50:

$$E_{\text{pair}}^{\text{exc}} = 8\pi A h = 6.53 \times 10^{-18}\ \text{J}. \tag{8.2}$$

The volume of our sample is of $6.28 \times 10^{-22}$ m$^3$ (thickness $h = 20$ nm) and therefore the corresponding increase in exchange energy density necessary for pair formation should be

$$\Delta e_{\text{pair}}^{\text{exc}} = 1.04 \times 10^{4}\ \text{J/m}^3. \tag{8.3}$$

This is in fact larger than the value we find for $\Delta e_{\text{thr}}^{\text{exc}}$ from the simulations. In first approximation, this can be understood from the significant overlap of the new vortex and antivortex cores. Indeed, the distance between them (as shown for example in Fig. 5.4 at $t = 12$ ps) is of approximately 20 nm, or only two core radii, so that their energy is effectively lower than the energy of two distinct cores. In section 8.4 however we show rigorously that the discrepancy is directly related to the size of the finite-element mesh.

Finally, we note that following the core switch, the average demagnetizing energy density in Fig. 8.1 does not fall below a fixed value (approximately $8 \times 10^3$ J/m$^3$), indicating that most of the additional demagnetizing energy in the sample $\Delta e_{\text{thr}}^{\text{dem}}$ is due to finite size effects, such as the distortion of the in-plane structure of the vortex and the interaction of the vortex with the sample edge, as observed in Fig. 7.3.

### 8.1.2 Variations with the applied current

Since the core reversal thresholds only depend on the production of the vortex-antivortex pair, the switching thresholds are expected to be unaffected when the current density $J$ is varied. To verify this, the density of the resonant current is varied between $J_s = 4 \times 10^{11}$ A/m$^2$ (minimum current required to trigger the switch) and $J_s = 1.5 \times 10^{12}$ A/m$^2$. Like in the previous section, we extract the energy densities at the moment of the core switch. The results are shown in Fig. 8.2. Contrary to our expectation, the energy densities however seem to increase: for example, the total energy density varies by 5% over the studied current density range. This deviation is larger than the statistical variations found in (8.1). We suspect here that at increasingly high current densities the system is in fact driven at a faster rate than the magnetization can react and the switching threshold is effectively overshot.

[1] A study of the influence of an axial anisotropy perpendicular to the surface plane on the core reversal has been conducted in Ref. [209]. It was equally found that such an anisotopy does not play a significant role unless its value is extremely large.

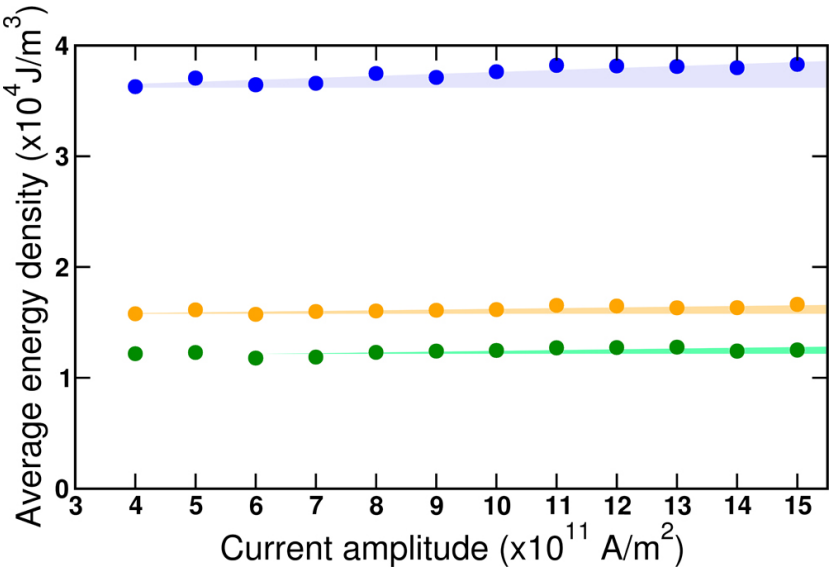


Figure 8.2: Evolution of the averaged maximal values of the partial energy densities during the core switch as a function of the amplitude of a resonant current. The current amplitude is varied in intervals of $1 \times 10^{11}$ A/m$^2$. The core only switches for densities above $4 \times 10^{11}$ A/m$^2$. The shaded regions highlight the increase in energy densities.

To test this hypothesis, we therefore cut the current a few picoseconds before the core switch occurs in the simulations, allowing the system to relax. If it already is above the threshold, the core switch should occur even in the absence of a driving force. This is indeed what we observe: the core switches even when the energy densities shown in Fig. 8.2 are not reached, indicating that these in fact exceed the switching threshold. By cutting the current at different moments back in time, the point when the system exactly reaches the switching energy can be determined. These obtained total and exchange energy thresholds are plotted in Fig. 8.3 as a function of current density. From that data, we extract the correct thresholds for the vortex core switch:

$$\begin{aligned} e_{\mathrm{thr}}^{\mathrm{tot}} &= (3.57 \pm 0.02) \times 10^4 \ \mathrm{J/m^3}, \quad \Delta e_{\mathrm{thr}}^{\mathrm{tot}} = (1.35 \pm 0.02) \times 10^4 \ \mathrm{J/m^3} \\ e_{\mathrm{thr}}^{\mathrm{exc}} &= (1.55 \pm 0.01) \times 10^4 \ \mathrm{J/m^3}, \quad \Delta e_{\mathrm{thr}}^{\mathrm{exc}} = (0.60 \pm 0.01) \times 10^4 \ \mathrm{J/m^3}. \end{aligned} \tag{8.4}$$

The exchange threshold thus corresponds to about 60% of the value required for the production of a new pair (8.3).

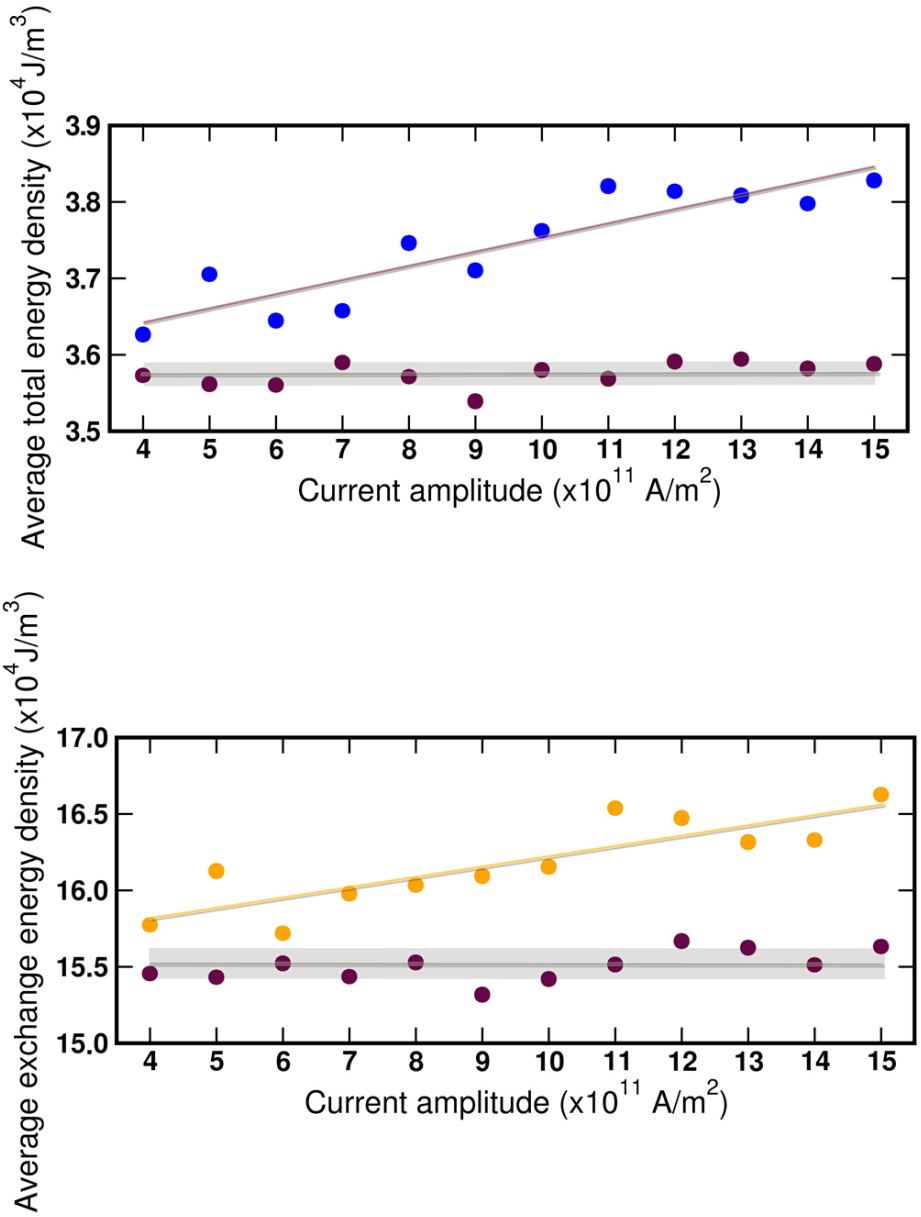


Figure 8.3: Thresholds for the total (**top**) and exchange (**bottom**) energy densities during the core switch. The blue and orange data are from Fig. 8.2 and result from overshooting the minimum threshold. The extracted thresholds are shown in dark blue for both cases; the dark grey line indicates their average value and the grey area indicates the standard deviation.

## 8.2 Energy evolution in response to short current pulses

The time evolution of the internal energy when a core switch is triggered by short non-resonant pulses is shown in Fig. 8.4. Two Gaussian pulses of different strengths and width $\sigma = 100$ ps are used. The energy evolution at the moment of the core reversal is the same as at resonance: a peak in exchange energy marking the pair production is followed by a sudden drop. For the studied sample geometry, $J = 7.3 \times 10^{12}$ A/m$^2$ is the minimum current density for which the switch occurs. At higher currents, the switch occurs a few tens of picoseconds earlier, and the threshold energy is overshot. This overshoot can lead to multiple switches for sufficiently strong currents. The switching thresholds are obtained again as described in section 8.1.2:

$$\begin{aligned} e_{\mathrm{thr}}^{\mathrm{tot}} &= 3.55 \times 10^4 \text{ J/m}^3, \quad \Delta e_{\mathrm{thr}}^{\mathrm{tot}} = 1.33 \times 10^4 \text{ J/m}^3 \\ e_{\mathrm{thr}}^{\mathrm{exc}} &= 1.52 \times 10^4 \text{ J/m}^3, \quad \Delta e_{\mathrm{thr}}^{\mathrm{exc}} = 0.58 \times 10^4 \text{ J/m}^3. \end{aligned} \tag{8.5}$$

These are within about 2-3% of the values we found at resonance (8.4). We can therefore conclude that *the thresholds for the vortex core switch are independent of the type of excitation.*

For completeness, we also investigate the influence of the degree of spin

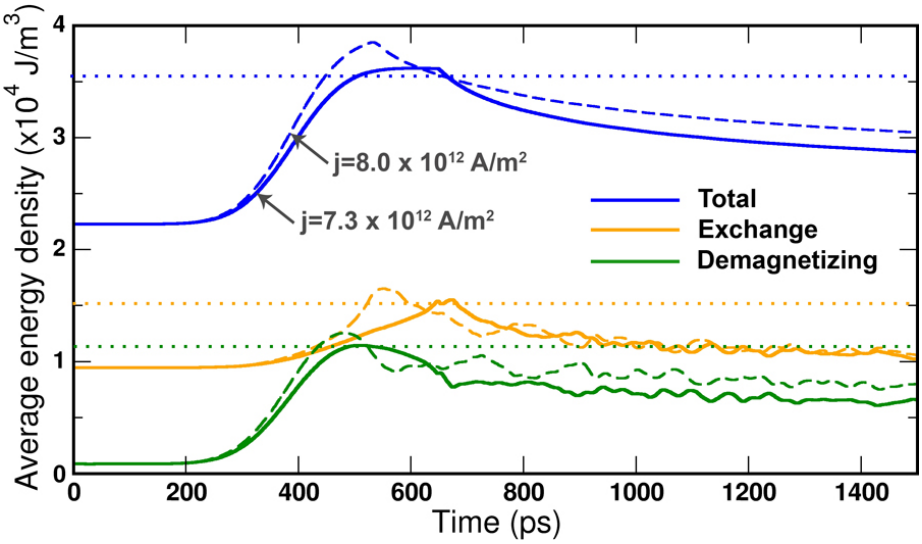


Figure 8.4: Evolution of the partial and total average energy densities for the core switch triggered by two current pulses of different strengths. The continuous and dashed lines correspond to the response for pulses with maximal amplitudes of J = 7.3 × 10$^{12}$ and J = 8.0 × 10$^{12}$ A/m$^2$, respectively. The horizontal dotted lines indicate the switching threshold energies.

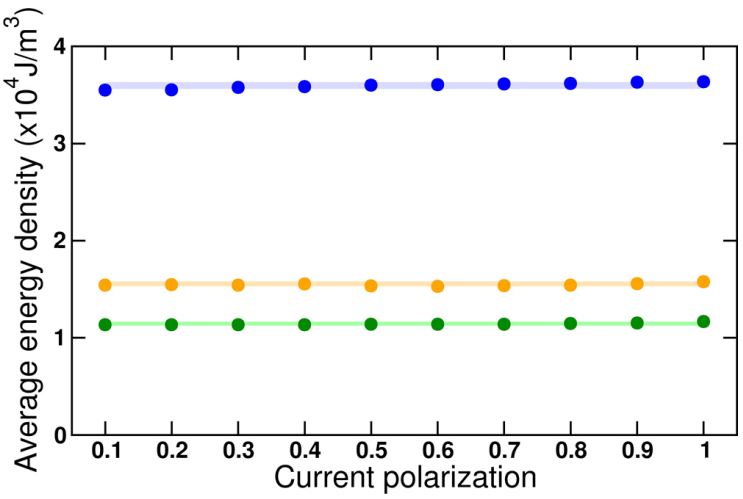


Figure 8.5: Energy densities at the moment of the core switch as a function of the degree of spin polarization of the current. The switch is triggered by non-resonant pulses, with amplitudes given in Fig. 7.7. The shaded regions show the standard deviation for each set of data which is less than 2%.

polarization of the current on the switching thresholds. The results are given in Fig. 8.5, which shows that the threshold energy densities do not vary with the current polarization.

## 8.3 Energy thresholds as a function of intrinsic parameters of the vortex

Having established that the switching thresholds are independent of the electric excitation parameters, we now look at the effect of intrinsic parameters such as the value of the damping constant and the sample size. In section 7.4, we found that varying $\alpha$ strongly affects the current densities required to switch the core. Similar to Fig. 8.1, we show in Fig. 8.6 the temporal evolution of the energy of a vortex core switched at resonance for $\alpha = 0.3$, which is thirty times larger than the damping value used so far. In this case, a driving current with an amplitude of $J_s = 6 \times 10^{12}$ A/m$^2$ is necessary to trigger the core reversal. At first look, the total and exchange energy densities are about 10% larger than the ones found in (8.4) for $\alpha = 0.01$. However, we determine that in this case the threshold is overshot as well. Extracting the total and exchange thresholds at $\alpha = 0.3$ over a period of 15 ns thus gives:

$$e_{\mathrm{thr}}^{\mathrm{tot}} = (3.58 \pm 0.02) \times 10^4 \text{ J/m}^3, \quad \Delta e_{\mathrm{thr}}^{\mathrm{tot}} = (1.35 \pm 0.02) \times 10^4 \text{ J/m}^3$$
$$e_{\mathrm{thr}}^{\mathrm{exc}} = (1.51 \pm 0.01) \times 10^4 \text{ J/m}^3, \quad \Delta e_{\mathrm{thr}}^{\mathrm{exc}} = (0.57 \pm 0.01) \times 10^4 \text{ J/m}^3. \quad (8.6)$$

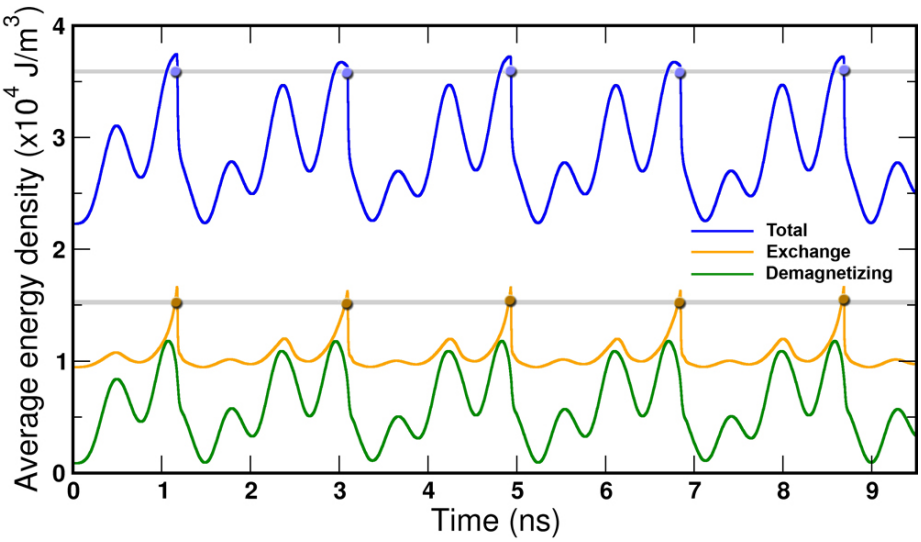


Figure 8.6: Evolution of the vortex energy for $\alpha = 0.3$ driven by a sinusoidal current of amplitude $J = 6 \times 10^{12}$ A/m$^2$. The blue and orange full dots indicate the threshold total and exchange energies each time the core reverses. The grey bands show the standard deviation on the average threshold energies.

These values turn out again to be within a few percent from those found for $\alpha = 0.01$ in (8.4). Further simulations with $\alpha = 0, 0.05, 0.1$ and $0.2$ confirm that the threshold energies remain unchanged by variations of $\alpha$.

Now, the radius of the sample is increased to 150 nm, keeping the thickness at 20 nm and $\alpha$ at 0.01. Fig. 8.7 shows the energy evolution of the vortex in response to a short electric pulse of strength $9 \times 10^{12}$ A/m$^2$ and $\sigma = 100$ ps. From expression (8.2), the exchange energy density required for the production of the vortex-antivortex pair is in this case

$$e_{\text{pair}}^{\text{exc},r=150\text{ nm}} = 0.46 \times 10^4 \text{ J/m}^3. \tag{8.7}$$

From the data in Fig. 8.7, we extract the following values for the threshold energies:

$$\begin{aligned} e_{\text{thr}}^{\text{tot},r=150\text{ nm}} &= 2.31 \times 10^4 \text{ J/m}^3, \quad \Delta e_{\text{thr}}^{\text{tot}} = 0.68 \times 10^4 \text{ J/m}^3 \\ e_{\text{thr}}^{\text{exc},r=150\text{ nm}} &= 0.74 \times 10^4 \text{ J/m}^3, \quad \Delta e_{\text{thr}}^{\text{exc}} = 0.28 \times 10^4 \text{ J/m}^3 \end{aligned} \tag{8.8}$$

Thus, despite a 50% increase in the sample radius, the value of $\Delta e_{\text{thr}}^{\text{exc}}$ represents again about 60% of the energy density required for the formation of a pair, as found in (8.4). This confirms that the switching threshold is equally independent of the vortex radius.

Additionally, we note here that the minimum current density for switching the core in this case is of $J = 9.1 \times 10^{12}$ A/m$^2$, which is higher than for the

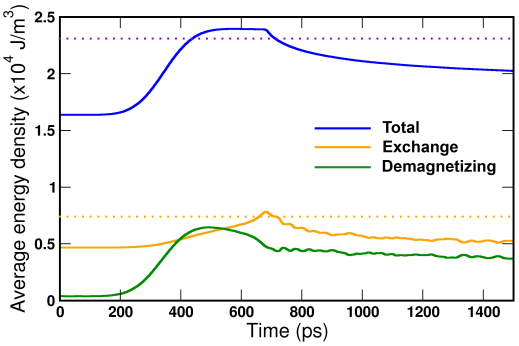


Figure 8.7: Energy evolution and switching thresholds (dotted lines) for a vortex in a sample of radius 150 nm and thickness 20 nm. The excitation is a Gaussian-shaped electric pulse with an amplitude of $J = 9.1 \times 10^{12}$ J/m$^2$.

smaller disk with a radius of 100 nm for which the minimum current density is of $J = 7.3 \times 10^{12}$ A/m$^2$. This illustrates the fact that the switching current scales with the size of the nanostructure. In contrast, the switching fields required to reverse the core are inversely proportional to the sample size.

## 8.4 Energy thresholds in iron

So far, we confirmed that, as expected from the analytic expression (8.2), the core reversal threshold is independent of the type of excitation as well as of intrinsic parameters of the vortex such as the sample radius and the damping constant value. Indeed, the value of the threshold is only expected to vary with the material and sample thickness.

We therefore start by investigating the switching threshold in a different material, namely Fe. For the simulations, we use the following parameters: $A = 2.1 \times 10^{-11}$ J/m and $\mu_0 M_s = 2.15$ T. A cubic anisotropy of $K_{c1} = 48$ kJ/m$^3$ is also included, however we find that this term does not affect the energy threshold. The same sample is considered as in section 8.1.1 with $r = 100$ nm, thickness 20 nm and a discretization distance between nodes of about 3 nm. Switching the vortex core using current pulses, we obtain the following thresholds:

$$\begin{aligned} e_{\text{thr}}^{\text{tot,Fe}} &= 5.21 \times 10^4 \text{ J/m}^3, \quad \Delta e_{\text{thr}}^{\text{tot,Fe}} = 1.64 \times 10^4 \text{ J/m}^3 \\ e_{\text{thr}}^{\text{exc,Fe}} &= 2.43 \times 10^4 \text{ J/m}^3, \quad \Delta e_{\text{thr}}^{\text{exc,Fe}} = 0.73 \times 10^4 \text{ J/m}^3. \end{aligned} \tag{8.9}$$

The analytic value for the exchange energy density of a pair is of $1.68 \times 10^4$ J/m$^3$. Interestingly, the computed threshold $\Delta e_{\text{thr}}^{\text{exc,Fe}}$ only represents 43% of this value, which does not correspond to our previous findings where the threshold was at 60%. In fact, a similar discrepancy was found in Ref. [59] between the critical velocities in Py and Fe. The reason for this difference was not explained and was considered as part of the computational error on the value of the velocity. We however find a different origin for this discrepancy, namely our choice of cell size. It has indeed been shown that the discretization strongly

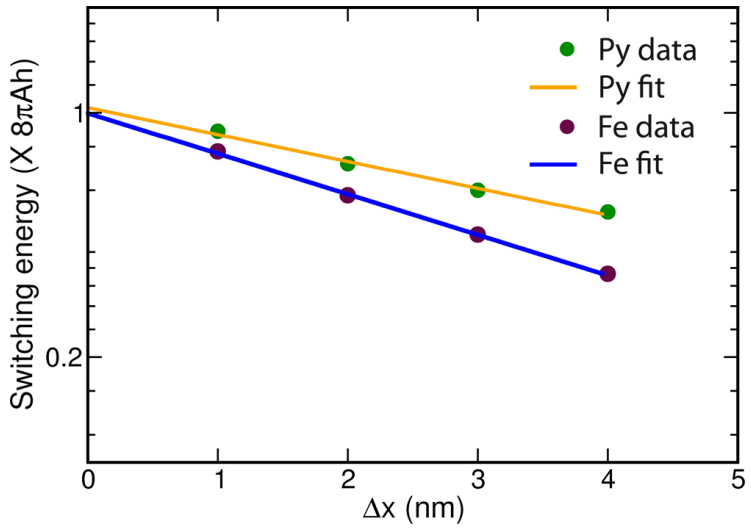


Figure 8.8: Evolution of the exchange energy threshold in Fe and Py as a function of the average distance Δx between neighboring discretization points. The best fit to the data is given by the exponential functions (8.10) and (8.11). A distance of 1 nm between nodes approximately corresponds to an equivalent cubic cell of 0.5 nm$^3$.

affects the computed value of the exchange energy of a magnetic configuration, in particular when a Bloch point is involved [28]. In such cases, the correct energies are obtained through extrapolation to zero cell size. We therefore vary the average spacing between discretization nodes $\Delta x$ from one to four nanometers: Fig. 8.8 shows the threshold energy as a function of $\Delta x$ for Fe and Py. Fits to the data reveal an exponential behavior of the energy:

$$E^{\mathrm{Fe}}_{\mathrm{switch}} = 1.002\ (8\pi Ah) \times e^{-0.27\cdot\Delta x} \tag{8.10}$$

$$E^{\mathrm{Py}}_{\mathrm{switch}} = 1.025\ (8\pi Ah) \times e^{-0.17\cdot\Delta x}. \tag{8.11}$$

Extrapolating to zero cell size thus yields an energy threshold of $8\pi Ah$ for the core reversal with an accuracy of 0.2% for Fe and of 2.5% for Py. The difference in accuracy is due to the fact that our fits are based on only a few points. Indeed, for discretization distances above 4 nm, the mesh is too coarse to precisely determine the threshold energy whereas below 1 nm we are limited by very long computation times.

This result confirms the energetic origin of the core reversal. It also explains the existence of a critical velocity. Döring [157] indeed showed that for a moving domain wall, a wall mass can be defined such that the classical expression for the kinetic energy $E = \frac{1}{2}mv^2$ holds. In this context, the critical velocity would be a direct consequence of the obtained energy threshold, given that a corresponding expression holds for the vortex.

We also note that the numerical values in the exponents of equations 8.10 and 8.11 correspond to $\frac{1}{l_{\mathrm{exc}}}$, where $l_{\mathrm{exc}}$ is the exchange length of the material. The exchange energy at the moment of the reversal is thus generally given as a function of the material and discretization distance by:

$$E_{\mathrm{switch}}^{\mathrm{exc}} = 8\pi Ah \times e^{-\frac{\Delta x}{l_{\mathrm{ex}}}}. \tag{8.12}$$

As discussed in section 3.5, this exponential behavior of the exchange energy is a consequence of the presence of a singularity in the finite-element simulations.

Finally, we also consider the effect of the sample thickness on the exchange threshold. The simulations were performed for Fe with a fixed discretization distance between nodes of 3 nm. Fig. 8.9 shows that the switching threshold remains around $0.46 \times 8\pi Ah$ independent of the sample thickness, as expected. Only a small deviation is visible for the 10 nm-thick sample. Since the discretization size is the same for all samples, this is attributed to the fact that there are comparatively fewer discretization nodes along the thickness in this sample, which leads to a larger error in the computation of the exchange energy. The higher exchange energy density in this case is attributable to the fact that at low discretization densities, the mesh acts analogous to defects in the material, which can hinder the propagation of the Bloch point and consequently the switching process. Such "mesh friction" was investigated in Ref. [28].

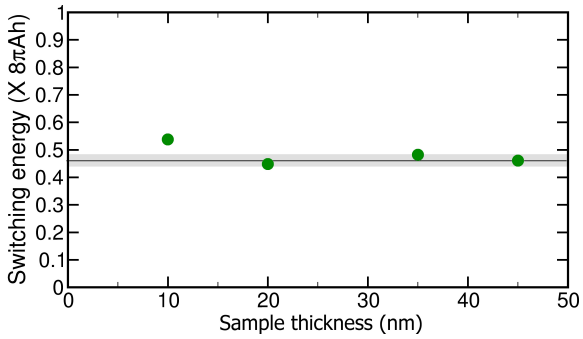


Figure 8.9: Exchange energy threshold in Fe samples of varying thicknesses. The thin blue line represents the average value of the threshold at 20 nm, 35 nm and 45 nm. The grey band represents the standard deviation of the average.

## 8.5 Summary: A local process driven by the exchange field

In this chapter, we demonstrated that the vortex core reversal is associated to a well-defined exchange energy barrier. This energy barrier corresponds to the energy required for the production of a new vortex-antivortex pair in the sample. In the simulations, the value of this energy strongly depends on the discretization; however, an extrapolation to zero cell size shows that the switching energy corresponds to

$$E_{\mathrm{exc}}^{\mathrm{threshold}} = 8\pi Ah. \tag{8.13}$$

This result implies that the material-specific exchange constant and the sample thickness are the only relevant parameters for the core reversal. We confirmed this dependence by varying the sample thickness as well as by investigating the thresholds in different materials. In addition, we showed that the thresholds are indeed independent of extrinsic as well as other intrinsic parameters of the vortex. In particular, we found that for both resonant and non-resonant electric excitations, variations in the current density and polarization do not affect the switching barrier. We equally established that the variation of intrinsic parameters such as the vortex radius or the damping do not affect the reversal thresholds.

Our analysis additionally sheds light on the difference between the resonant and non-resonant switching routes. Indeed, when the vortex is excited by short and strong pulses, the energy barrier is quickly overcome. The barrier can equally be overcome by slowly increasing the vortex energy through resonant excitation, as schematically illustrated in Fig. 8.10. In addition, the existence of a reversal threshold explains why multiple reversals occur for sufficiently strong switching pulses, as well why the observed switching process is "quantization" in energy.

These conclusions stand in contrast to the models suggested in Refs. [57, 59], which consider the vortex velocity as the determining parameter for the core reversal.

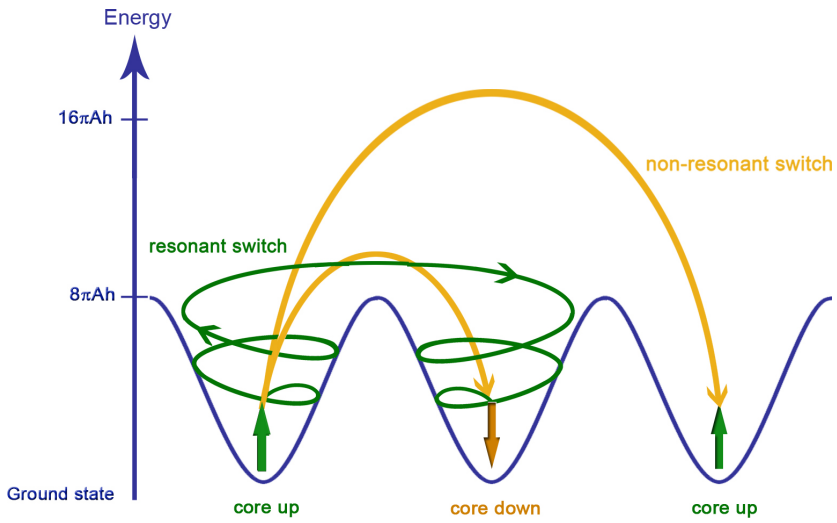


Figure 8.10: Schematic representation of the resonant and non-resonant core reversals based on the vortex energy.

In summary,

- The core switch occurs for a well-defined energy threshold of the exchange energy, confirming that the reversal is driven by the exchange field.
- This threshold corresponds to the energy necessary for the formation of a new vortex-antivortex pair.
- The vortex core reversal is therefore governed by the energy of the vortex, and not by its velocity.

# 9

# Stimulated vortex-antivortex pair production

In this chapter the consequences of the existence of a threshold energy related to the core reversal are explored. While we have established that this threshold corresponds to the energy necessary for the creation of a vortex-antivortex pair, the following questions however still remain open:

- Is energy a necessary and sufficient criterion for the core reversal?
- Based on the determined energy thresholds, can we find a new route to switch the core?

We answer these questions here, first by showing that a vortex-antivortex pair can be produced in a controlled manner within a vortex structure by a *static uniform* magnetic field focused on an area roughly corresponding to the radius of two cores. The pair production indeed occurs once the energy density locally reaches the thresholds determined in chapter 8. Moreover, we find that vortex-antivortex pairs can equally be produced in a controlled manner even in single-domain magnetic samples. Second, we demonstrate that if the pair is created within an existing vortex structure and has an opposite polarization with respect to the initial vortex core, the reversal mechanism is automatically triggered, without requiring the excitation of the gyrotropic motion of the vortex.

At this point, a detour into quantum mechanics can provide, by analogy, insight into the results presented in this chapter. The vortex pair production is indeed reminiscent of charged pair production from the vacuum in quantum electrodynamics via the Schwinger mechanism [210]. Schwinger predicted over half a century ago that in the presence of a static, uniform electric field the vacuum becomes unstable and can "spark" with spontaneous emission of charged particle pairs. In particular, stimulated vacuum pair production, illustrated in Fig. 9.1, is expected to occur in the presence of intense focused laser fields [211, 212, 213, 214]. For production to spontaneously occur above the tunneling threshold, the electric field strength has to exceed a critical value over an area of the size of the Compton wavelength of the produced particle. These requirements are strikingly similar to the ones we find for the production of a vortex-antivortex pair.

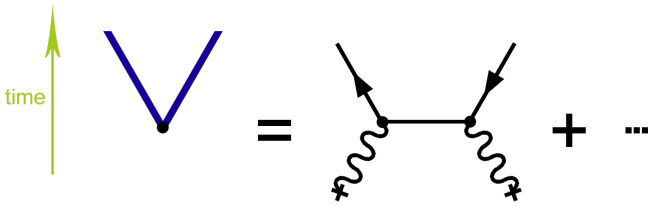


Figure 9.1: Feynman diagram for the main contribution to the vacuum electron-positron pair production. The wiggled lines starting on a cross represent the quantization of the electromagnetic field. (After Ref. [211])

## 9.1 Pair production in a sample enclosing a vortex

In the following, we demonstrate that a pair can be produced within a vortex structure using a strong, local static external field. The field is applied within a 20 $nm^3$ volume of a vortex in a cylindrical Permalloy sample identical to the one used in chapters 7 and 8 (radius 100 nm, thickness 20 nm and discretization size of 3 nm). The damping constant is $\alpha = 0.01$. The region over which the field is applied is comparable to the size of the dip, which develops during the reversal process and roughly corresponds to two core radii. Our simulations show that depending on the location at which the pair is created, different dynamics are possible.

### 9.1.1 Pair production at a distance from the vortex core

First, the external field is applied in a region 50 nm away from the vortex core. To maximize the Zeeman energy, the direction of the field is opposite to the direction of the in-plane curling magnetization, as illustrated in Fig. 9.2a. The induced precession results in the local increase of the out-of-plane component of the magnetization (Fig. 9.2b). For field strengths above 1.15 T, this leads to the production of a vortex-antivortex pair, shown in Fig. 9.2c. The polarization of the pair is independent of the initial vortex polarization. In the case shown here, it is the same as for the initial vortex. We note that the pair creation conserves the total winding number as described in chapter 2, section 2.2.3. In addition, the newly formed vortex has the same vorticity $\varphi_0 = 1$ as the initial one. Once the pair is nucleated, the initial vortex position remains largely unchanged. Meanwhile, the vortex and the antivortex describe a translational motion, or Kelvin motion, following the dynamics presented in section 4.3.1. This is shown in Fig. 9.2d. It was noted in Ref. [158] that the Kelvin motion is comparable to the steady translational motion of an electron-positron bound state in a transverse magnetic field which exactly balances the Coulomb force. The observed pair dynamics occurs when the pair is created slightly above the critical energy threshold required for pair production. The additional energy is converted into kinetic energy [160]. Indeed, locally, the Zeeman energy density contributed by the applied field is of $-\mu_0(\boldsymbol{M}_s \cdot \boldsymbol{H}_{ext}) = 9.2 \times 10^5$ J/$m^3$. This is

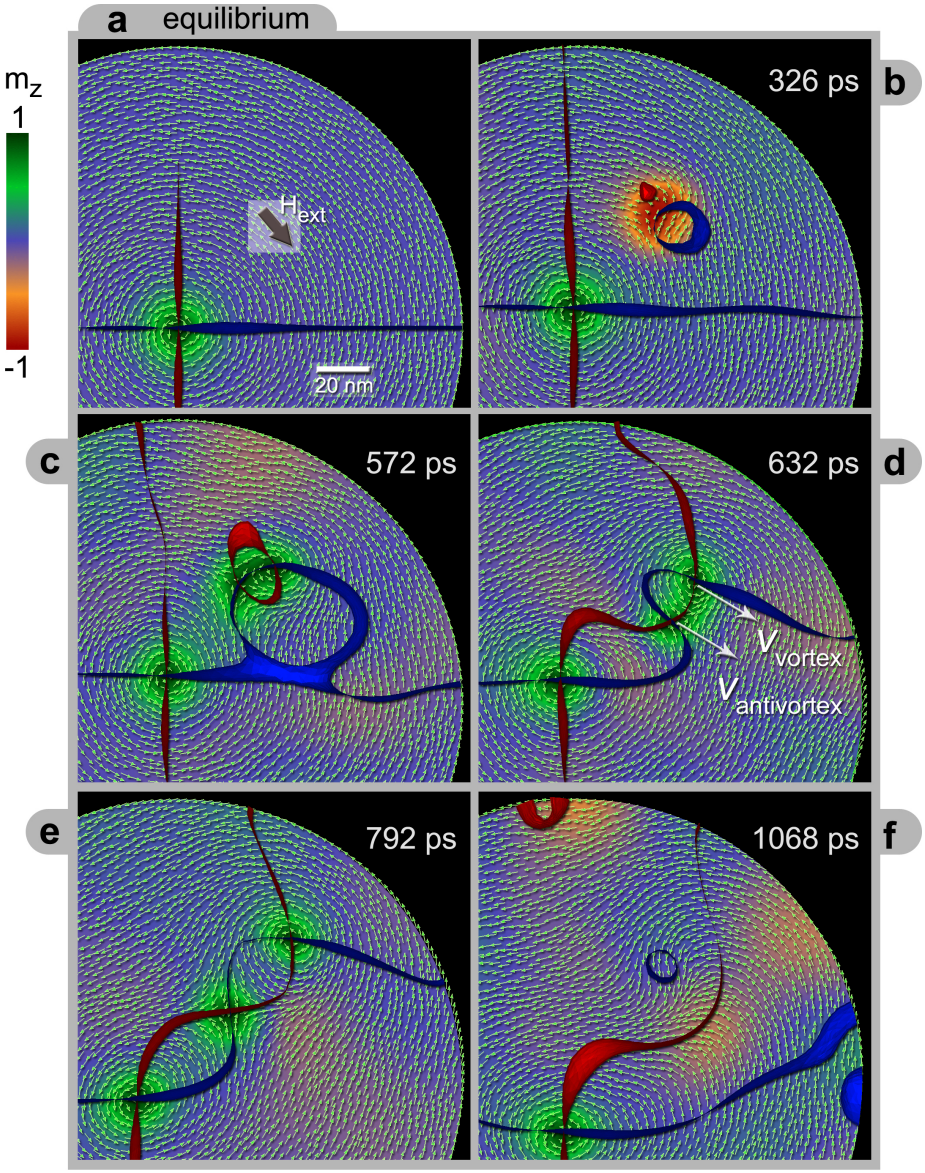


Figure 9.2: Vortex-antivortex pair production in a vortex structure. **a**, A 1.15 T static field is applied 50 nm away from the core over a 20 nm$^2$ region. The blue ribbon represents the $m_x = 0$ isosurface, while the $m_y = 0$ isosurface is represented by the red ribbon. The color scale indicates the *z* component of the magnetization. **b**, During the initial precession of the magnetization, the out-of-plane component increases in the region where the field is applied. **c**, This eventually results in the nucleation of a vortex-antivortex pair indicated by the aditional intersections of the isosurfaces. **d**, The new pair describes a linear motion, before 'falling' (**e**) into the attractive potential of the original vortex. **f**, The pair eventually smoothly dissolves.

above the analytic value for the energy required to produce a pair, which is of $8.2 \times 10^5$ J/m$^3$ according to equation (8.2) for a 20 nm$^3$ volume[1]. Fig. 9.3 shows the evolution of the exchange and total internal energy densities in the sample. The variation in exchange energy density is here of $\Delta e_{\rm thr}^{\rm exc} = 1.2 \times 10^4$ J/m$^3$, compared to $\Delta e_{\rm thr}^{\rm exc} = 0.6 \times 10^4$ J/m$^3$ found in section 8.1.2 for the reversal threshold.

This additional energy is however quickly dissipated, the velocity of the pair decreases and the interaction between the original vortex and the antivortex results in the displacement of the original vortex away from its equilibrium position. The structure eventually behaves like a coupled vortex-antivortex-vortex system (cross-tie), as shown in Fig. 9.2e. The antivortex moves back and forth between the two vortices, in search of an equilibrium position. After about one nanosecond the produced pair smoothly unwinds (Fig. 9.2e), in agreement with the dynamics described in section 4.3. Following the dissolution of the pair, the magnetization locally reaches an equilibrium in the external field and no further pairs are produced.

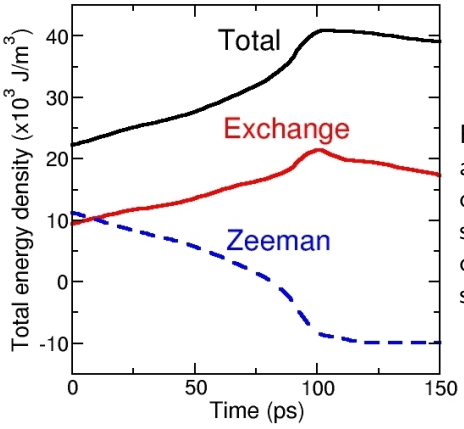


Figure 9.3: Time evolution of the averaged partial energy densities during the core reversal induced by a 1.15 T local static field. The total internal energy includes the exchange, demagnetizing and surface anisotropy contributions.

### 9.1.2 Pair production in the vicinity of the vortex core

Because the core reversal mechanism requires the production of a new vortex-antivortex pair in the vicinity of the core, we now apply the same 1.15 T field only some 20 nm away from the core, as illustrated in Fig. 9.4a. In contrast to the previous case, the magnetization does not precess locally, but immediately turns out of the plane in the direction opposite to the core orientation. This behavior is attributed to the strong static demagnetizing field of the nearby core, which remains immobile. Fig. 9.4b shows that a dip in the magnetization evolves within only approximately 50 ps. The vortex and the dip subsequently

[1]For the discretization distance of 3 nm used here, the numeric threshold is in fact of only $4.9 \times 10^5$ J/m$^3$.

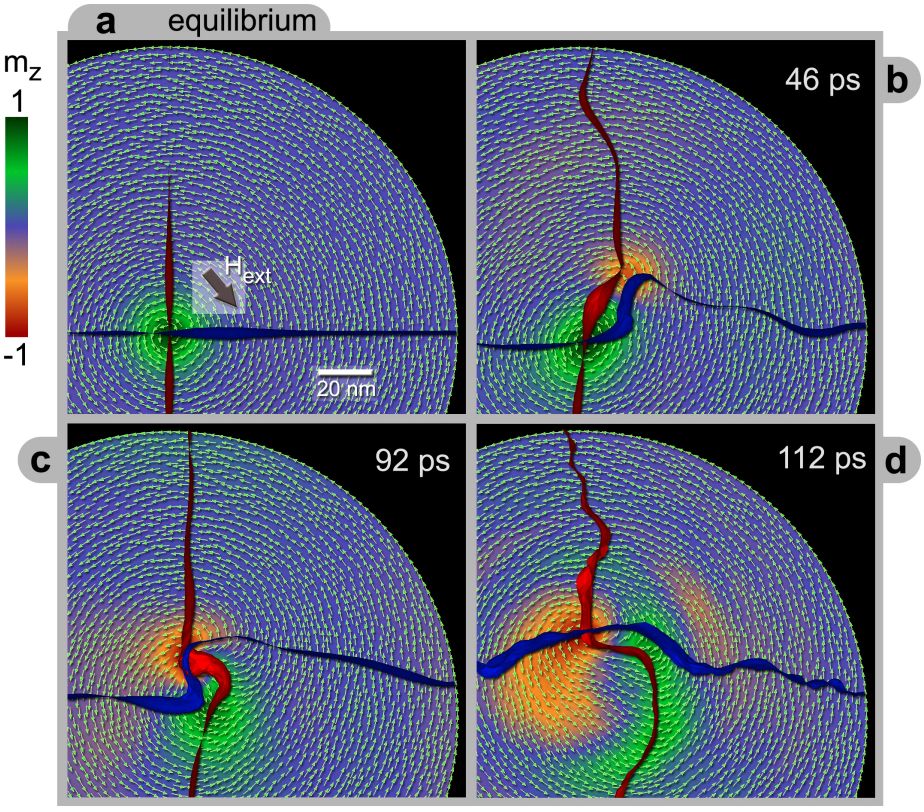


Figure 9.4: Vortex-antivortex pair production in a vortex structure. **a**, A static local 1.15 T field is applied some 20 nm away from the core. **b**, In this case, the demagnetizing field of the core determines the direction of the out-of-plane component of the magnetization in the region where the field is applied. **c**, This rapidly results in the production of a pair, followed by the annihilation process. **d**, The new core is eventually left behind, close to its original position, which allows for a fast relaxation.

rotate about each other. This displacement of the core is likely due to the existence of a weak torque exerted by the external field applied in its vicinity. After about 90 ps, (Fig. 9.4c), the pair creation and annihilation processes unfold as described in section 5.2, leaving behind the new vortex with opposite polarization shown in Fig. 9.4d. The local creation of a vortex-antivortex pair therefore defines a new route for switching the core using a *static* field. As we found in chapter 5, the switching process itself unfolds over about 40 ps. However, the *total switching time* from the moment the field is applied is now shorter. Moreover, since the gyrotropic motion of the vortex is not excited, it is not necessary anymore to adjust the field parameters such as its amplitude or duration as was the case in chapter 5, section 5.3. At stronger static fields, the pair is produced within even shorter times: for example at 1.5 T, the annihilation process occurs only 55 ps after the application of the field.

## 9.2 Pair production in a single-domain structure

Having established the possibility of creating vortex-antivortex pairs within a vortex structure, we now turn to a single-domain structure. To this effect, we consider a 200 nm-long rectangular Permalloy prism-shaped sample, 100 nm wide and 20 nm thick as shown in Fig 9.5a. The structure is discretized into 6,250 tetrahedra, yielding an average cell size of about 4 $nm^3$. We again consider a typical damping $\alpha = 0.01$. At the center of the sample, a static external field is applied in the plane of the sample over an area of 20 $\times$ 20 $nm^2$, throughout the thickness (Fig. 9.5b) in the direction opposite to the magnetization. This field is applied at 1° with respect to the $x$ axis in order to break the symmetry of the configuration. The subsequent precession of the magnetization and the increase of its out-of-plane component are shown in Fig. 9.5c,d. We find that an external field of 1.2 T is required for the pair production to occur. In this case however, the out-of-plane region of the magnetization evolves into two distinct vortex-antivortex pairs. The polarization of these pairs is identical, as seen in Fig. 9.5e,f. Their position is highlighted by the $m_x = 0$ (dark green) and $m_y = 0$ (yellow) isosurfaces. The pairs eventually unwind and the magnetic structure reaches an equilibrium configuration in the local field. In Fig. 9.5g,h the region where the magnetization is locally aligned with the field, is enclosed by the $m_x = 0$ isosurface.

We note that the energy brought by the field into the system is of about 60% of the energy of two pairs, which corresponds to the numeric value of the pair creation threshold expected for the discretization length used here. However, while pairs can be created, they do not stabilize in the sample. Using stronger fields of *e.g.* 1.3 T, we find that one of the pairs can stabilize and remains pinned by the field.

While energy is at the origin of the pair formation like in the previously studied cases, why are *two* pairs created from the single domain state? The answer lies in the symmetry of the ground state. Indeed, in addition to conserving the total winding number, the formation of two pairs equally conserves the

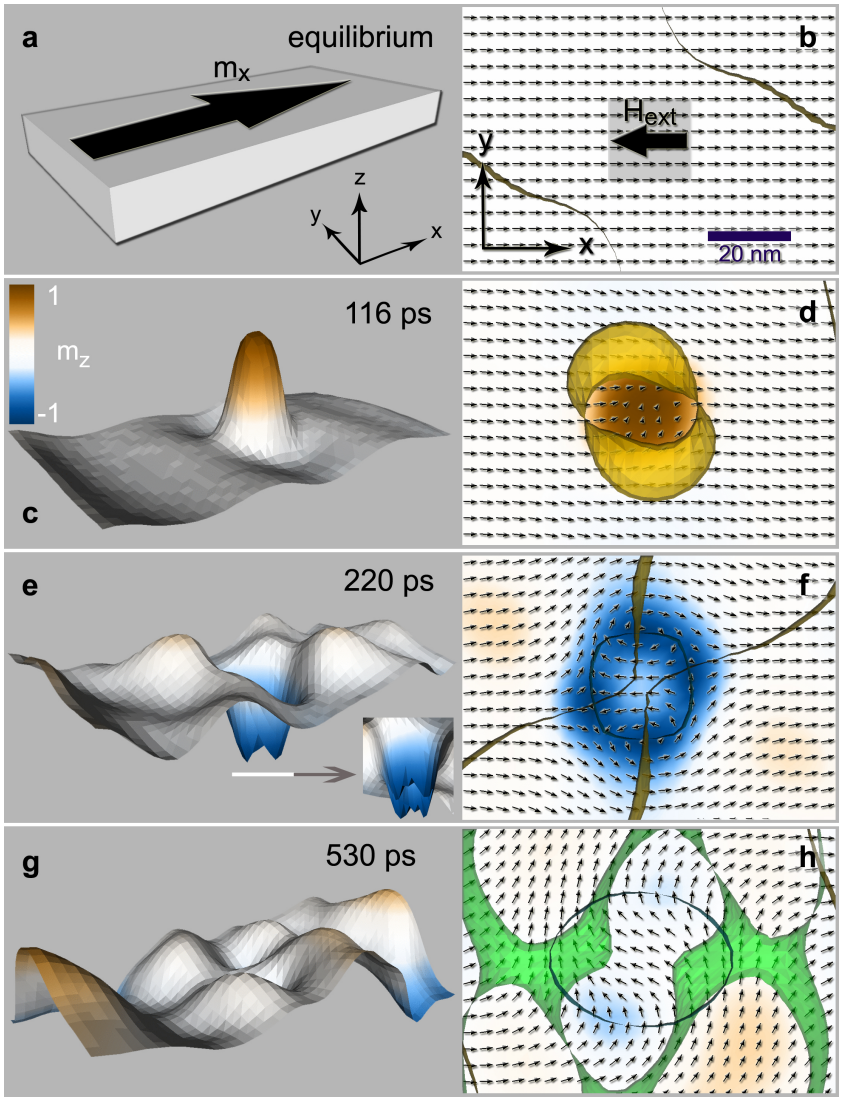


Figure 9.5: Vortex-antivortex pair production in a single-domain structure. The left column shows the evolution of the out-of-plane component of the magnetization. The right column shows the in-plane magnetization in the region of the field. The color map represents the $z$ component of the magnetization. The yellow and dark green ribbons represent the $m_y = 0$ and $m_x = 0$ isosurfaces, respectively. **a**, Schematic representation of the magnetization in the sample. **b**, Central area of the sample where a static field of 1.2 T (shaded area, 20 nm $\times$ 20 nm) is applied. **c**-**f**, Production of two pairs in the sample. The zoom in **e** shows their $z$-component from a different angle. **g**-**h**, The pair has unwinded. The light green isosurfaces represent the regions where $m_z = 0$, showing the nodal surfaces of the resulting standing spin waves [35].

inversion symmetry of the original single-domain state. We note that symmetric configurations often do not represent the lowest energy state, which can only be obtained by breaking the inversion symmetry. This is the case of the vortex, allowing the formation of a single pair. Furthermore, inversion symmetry is also embedded within the Landau-Lifshitz-Gilbert equation [215] and is therefore conserved during dynamic processes, unless it is broken for example by means of an external field [216].

Next, to verify if a strong local torque can equally trigger the pair creation[2] we apply the same 1.2 T field perpendicular to the direction of the local magnetization, *i.e.* in the $y$ and $z$ directions in Fig. 9.5. The simulations show that the magnetization rapidly precesses about the applied field, resulting in a region with a pronounced out-of-plane component after only 12 ps. However, in spite of the presence of a dip, no pair develops. The magnetization eventually relaxes in the field and spin waves are produced. These results confirm that the pair creation is uniquely driven by the *local energy*.

If we do not require the energy increase to be local, but rather apply a strong field in the plane of the entire sample, the magnetization dynamics is very inhomogeneous. While it is known that the magnetization reversal in single-domain particles can be complex and inhomogeneous [24], involving the nucleation of vortices at the sample boundaries, Fig. 9.6 shows that for fields of the order of 4 T, the single-domain state breaks down, like the vacuum, into numerous pairs.

## 9.3 Current-induced pair production

So far, we have discussed pair production induced by a magnetic field. While focusing magnetic fields of strengths comparable to the ones required for the pair production is currently achieved in hard-drive write heads, this remains a difficult task to achieve experimentally. It would therefore be more practical if the pair production could be induced by a local strong, spin-polarized current, such as in a point contact geometry [217, 218]. We therefore performed simulations for such a geometry, considering only the STT effect and neglecting the influence of the Oersted field. We found that a spin-polarized current alone, even as high as $6\times10^{13}$ A/m$^2$, does not lead to pair production. It rather results in the local steady state precession of the magnetization accompanied by the production of spin waves. This is not surprising in view of our earlier observation that a torque alone acting on the magnetization does not lead to pair creation.

We note that if the point contact in our simulations is only a few nanometers away from the core (similar to the case described for the local field in section 9.1.2) the core indeed switches for currents above $5\times10^{13}$A/m$^2$. However, this reversal process is rather due to the very strong excitation of the magnetization within the entire sample (spin waves) rather than to pair creation.

[2] An early interpretation of the core reversal mechanism based on torques was indeed suggested in Ref. [164].

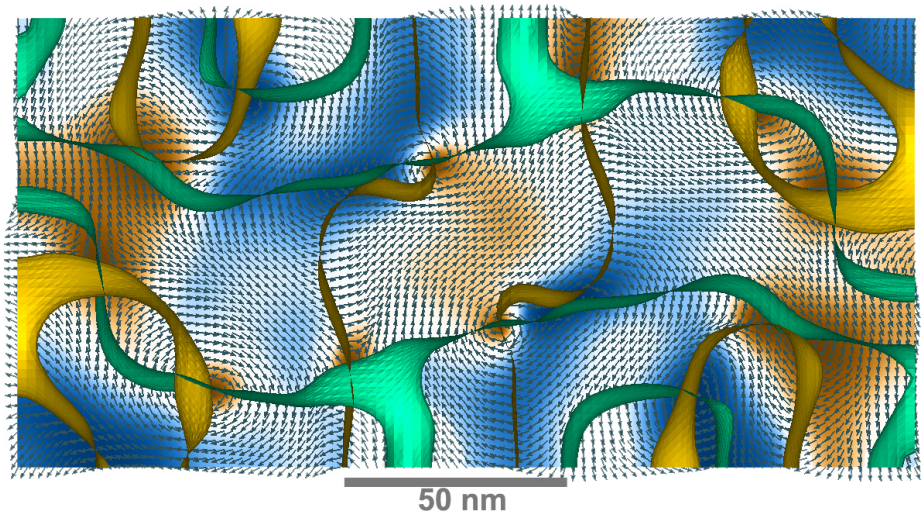


Figure 9.6: Breakdown of a single-domain structure into vortex-antivortex pairs 650 ps after the application of a static uniform 4 T field. The produced vortices and antivortices are located at the intersections of the orange ($m_y = 0$) and green ($m_x = 0$) isosurfaces. These are created in paris, unless they nucleate at the boundaries. The colormap represents the $z$-component of the magnetization, like in Fig. 9.5. The structure displays inversion symmetry.

Recently, low frequency modes found in point contact measurements via magnetoresistance measurements [219, 220], have been attributed to the creation and oscillation of a vortex-antivortex pair about the contact [221, 222]. The micromagnetic simulations performed in Refs. [222, 223], together with theoretical calculations [221] indicate however that it is crucial to consider the action of the Oersted field in order to achieve agreement with the experimentally measured frequencies. Further studies are therefore required to assess the effect of the Oersted field on the pair production mechanism.

## 9.4 Summary

In this chapter we demonstrated that vortex-antivortrex pairs can be produced in a local static magnetic field. The pairs creation occurs once a well-defined local energy is reached, corresponding to the exchange energy of the core of a vortex and an antivortex – in analogy to charged pair production in quantum field theory. While pair creation conserves the topological charge of the sample (winding number), the number of pairs created is determined by the symmetry of the system. In magnetic configurations that preserve inversion symmetry, at least two pairs are produced. When this symmetry is broken, such as in a vortex ground state, a single pair can be produced.

In addition, our investigation of the pair production dynamics within a vortex structure established that two distinct cases occur depending on the distance of the pair from the core. When it is produced far from the core, a transient cross-tie structure can develop, whose dynamics is determined by the attractive vortex-antivortex interaction described in section 4.1.3. In contrast, when the pair is produced only a few nanometers from the core, its polarization is always opposite to the orientation of the original core, triggering an annihilation process leading to the reversal of the original vortex core. In contrast to the process presented in chapter 5, reversing the core through the direct creation of a pair leads to the reversal of a *static* core, showing that he gyrotropic motion of the vortex is not necessary for the core switch to occur. These results therefore unambiguously establish that energy is indeed the fundamental quantity controlling the core reversal. In addition, because only a static field is required, no pulse shaping or tuning is required like in section 5.3. Instead, the required static field strength only depends on the energy necessary to create the pair.

While this new switching route requires focusing a strong magnetic field, there is experimental evidence suggesting that it should equally occur in a point contact geometry under the influence of the Oersted field of a spin-polarized current.

In summary:

- Vortex-antivortex pairs can be locally produced in ferromagnetic samples by means of a focused static magnetic field. The pair creation is triggered by the local increase in exchange energy above the production threshold.
- The number of pairs which are created depends on the presence or absence of inversion symmetry of the original magnetic configuration.
- The localized production of a pair in a vortex can trigger the reversal of the core polarization, effectively removing the dependence of the reversal process on the field pulse strength and duration. This new switching route suggests a method for measuring the reversal of the vortex core, which does not require the excitation of the vortex.

# 10 Conclusion

In this thesis, we conducted detailed investigations on the ultrafast dynamics of magnetic vortices using micromagnetic simulations based on the finite-element method. Our simulations led to the description of a novel process in micromagnetism: the ultrafast reversal of the vortex core. Five aspects of this reversal were studied:

1. the micromagnetic mechanism leading to the reversal;
2. the ultrafast dynamics of magnetic antivortices, which occur as a part of the reversal process;
3. the electric reversal of the vortex core;
4. the origin of the core reversal;
5. the production of vortex-antivortex pairs in a strong static field.

### Ultrafast reversal of the vortex core

First, we investigated the response of a magnetic vortex to ultrashort field pulses, with a duration ranging between a few picoseconds and a few hundreds of picoseconds. We found that the dynamic response is driven by the out-of-plane magnetization in the region of the core. Indeed, the field pulses can trigger a dramatic series of events leading to the destruction of the core and to the formation of a new one, finally resulting in the reversal of the core orientation. Microscopically, this reversal is mediated by the production of a short-lived vortex-antivortex pair. The pair formation is followed by an annihilation process during which the initial vortex and the newly-formed antivortex are dissolved, resulting in the sudden production of spin waves. The dynamics of this process is a direct consequence of the topological properties of vortices and antivortices, in particular of Skyrmion number conservation.

This complex series of processes represents a fundamentally new magnetic switching mechanism. Because it is driven by the exchange field, we established that the core reversal unfolds over a duration of only about 40 ps, which makes it the *fastest field-induced reversal* known to date. In addition, the core reversal

can be triggered by field pulses as short as 5 ps. The ultimate field-induced switching limit had previously been found to be of about 160 ps [31], in the context of the precessional switching of the magnetization. The difference in switching times stems from the fact that the precessional switching relies on the demagnetizing field, which is typically about one hundred times weaker than the exchange field.

Owing to their perfect bistability, vortex cores have been suggested as promising candidates for binary data storage. The ultrafast reversal mechanism we described opens the possibility of a technological application of vortices.

### Ultrafast antivortex dynamics

Since the vortex core reversal involves the production of an antivortex, the topological counterpart of the vortex, such a reversal process could also characterize the ultrafast dynamics of the antivortex itself. While this would be expected from a topological point of view, the antivortex possesses a very different in-plane magnetization distribution. Notably, this distribution gives rise to volume charges and consequently to a strong stray field, which can influence the dynamics. Moreover, the presence of charges makes the antivortex metastable, such that it always is enclosed by vortices at static equilibrium. Our simulations showed that even in an isolated antivortex, the structure is surrounded by *virtual* vortices.

By exciting an isolated antivortex with ultrashort field pulses, we found that these pulses can trigger a series of processes, which are complementary to those found in the vortex, despite their different in-plane structure. In this case, a new pair is emitted by the antivortex, resulting in the production of a transient *anti* cross-tie wall. On such short time scales magnetic structures can indeed be produced, which are not found in stable configurations. The pair production is followed by an annihilation process, leaving behind a new antivortex with opposite polarization. We showed that the spin waves produced by the reversal process can effectively propagate into a waveguide extending the antivortex structure. These spin waves can be used to drive novel circuits, in which their phase can be manipulated to perform logical operations.

Our study also sheds light on recent experiments involving cross-tie walls, in which a multiplication of the number of cross-ties was observed in response to short field pulses [180]. This must therefore proceed through the creation of new vortex-antivortex pairs originating from the vortex as well as from the antivortex. The new pairs can stabilize in sufficiently large samples.

### Current-induced vortex core reversal

Following our study of the field-induced vortex core reversal, we investigated the vortex dynamics induced by spin-polarized electric currents. We found that the core reversal can equally be achieved electrically. Moreover, the switching can occur via two distinct routes. First, the vortex can be excited resonantly, driven by an AC current tuned to the resonant frequency of the vortex. For

sufficiently high amplitudes of the driving current, the core reversal occurs after a few nanoseconds. Second, we showed that the core can be reversed by means of non-resonant excitations, namely single, short electrical pulses. This method triggers the reversal process within only hundreds of picoseconds and requires higher current densities. Interestingly, we found that the core reversal proceeds via the same pair creation-annihilation mechanism in both cases. Thus, the switching process unfolds in both cases within about 40 ps – while the total time required to trigger the switch, counted from the moment the current is switched on, differs by an order of magnitude.

While our study was fundamental in nature, it bears direct consequences for the practical implementation of vortices in memory devices. The current-induced reversal, in particular that induced by means of single electric pulses, indeed allow precise control of the core orientation. Based on this possibility, architectures for magnetoresistive random-access memories in which the orientation of the vortex core is exploited (VRAM) have been proposed [204, 205].

### Origin of the vortex core reversal

The finding that the switching mechanism is independent of the core reversal route has motivated our search for the fundamental quantity determining the core reversal. To this effect, we systematically investigated the evolution of the vortex energy and found that the reversal occurs once the exchange energy exceeds a well-defined threshold. This threshold corresponds to the energy necessary for the creation of a vortex-antivortex pair. Once the new pair is formed, the annihilation occurs without the need to overcome an additional energy barrier.

Our study stands in contrast to the present interpretation of the origin of the core reversal in which the vortex velocity is considered to control the reversal. This interpretation based on velocity implies the existence of a critical velocity for the reversal, in analogy to the Walker velocity for domain walls. However, the velocity interpretation does not account for the observed pair production dynamics. We also note that while the vortex velocity and energy are certainly complementary quantities, no functional relationship has yet been derived linking them.

### Controlled vortex-antivortex pair production

To explore the consequences of our interpretation based on the vortex energy, we locally increased the energy to the identified threshold value over a small region of a vortex sample. This was achieved by applying a static external field in the direction opposite to the local magnetization. The size of the region corresponded to the area of two vortex cores. Using fields higher than the saturation magnetization, we proved that the local increase in energy sparks the creation of vortex-antivortex pairs. We furthermore found that vortex-antivortex pair formation is a general property of ferromagnetic materials and that it can also be triggered in single-domain samples. Moreover, the number of pairs created

depends on the symmetry of the magnetic configuration. Indeed, for initial configurations exhibiting inversion symmetry, an even number of pairs are created, conserving the symmetry. However, if inversion symmetry is initially broken, a single pair can be created.

Since the inversion symmetry is broken by the in-plane circulation of the magnetization in a vortex structure, the application of a strong static localized magnetic field results in the creation of a single pair. If this pair is produced in the vicinity of the vortex core, we found that the switching mechanism is automatically triggered. This effectively results in the dynamic reversal of an immobile core, proving that the vortex velocity is not decisive in the reversal process. It is rather the *creation of a new vortex-antivortex pair* which controls the reversal.

On the basis of our energy interpretation, we have predicted a new method for triggering the core reversal using local static magnetic fields. This method results in a faster total switching time, since it does not require the direct excitation of the vortex. Moreover, unlike the case of the resonant or single-pulse driven reversals, the field strength is independent of the sample geometry – it only depends on the exchange constant of the material.

In conclusion, we provided detailed predictions for the ultrafast dynamics of magnetic vortices. Some of these predictions have already been confirmed experimentally, such as the possibility of reversing the core using non-resonant excitations. Other predictions like the ultrafast nature of the reversal process or the local creation of vortex-antivortex pairs by means of a static magnetic field still await confirmation. These results highlight the essential role played by micromagnetic simulations in predicting new phenomena and in motivating experimental investigations.

# Bibliography


[1] G. Binasch, P. Grünberg, F. Saurenbach, and W. Zinn, *Enhanced magnetoresistance in layered magnetic structures with antiferromagnetic interlayer exchange*, Phys. Rev. B **39**, 4828 (1989).

[2] M. N. Baibich, J. M. Broto, A. Fert, F. N. Van Dau, F. Petroff, P. Etienne, G. Creuzet, A. Friederich, and J. Chazelas, *Giant Magnetoresistance of (001)Fe(001)/(001)Cr Magnetic Superlattices*, Phys. Rev. Lett. **61**, 2472 (1988).

[3] S. S. P. Parkin, *Dramatic enhancement of interlayer exchange coupling and giant magnetoresistance in $Ni_{81}Fe_{19}/Cu$ multilayers by addition of thin Co interface layers*, Appl. Phys. Lett. **61**, 1358 (1992).

[4] D. E. Heim, R. E. Fontana, C. Tsang, V. S. Speriosu, B. A. Gurney, and M. L. Williams, *Design and Operation of Spin-Valve Sensors*, IEEE Trans. Magn. **30**, 316321 (1994).

[5] H. H. Hopster and H. P. Oepen, *Magnetic Microscopy of Nanostructures*, Springer, Berlin (2004).

[6] G. van der Laan, B. T. Thole, G. A. Sawatzky, J. B. Goedkoop, J. C. Fuggle, J.-M. Esteva, R. Karnatak, J. P. Remeika, and H. A. Dabkowska, *Experimental proof of magnetic x-ray dichroism*, Phys. Rev. B **34**, 6529 (1986).

[7] G. Schütz, W. Wagner, W. Wilhelm, P. Kienle, R. Zeller, R. Frahm, and G. Materlik, *Absorption of circularly polarized x rays in iron*, Phys. Rev. Lett. **58**, 737 (1987).

[8] A. Hubert and R. Schäfer, *Magnetic Domains - The Analysis of Magnetic Microstructures*, Springer, Berlin, New York, Heidelberg (1998).

[9] Y. Martin and H. K. Wickramasinghe, *Magnetic imaging by 'force microscopy' with 1000 Å resolution*, Appl. Phys. Lett. **50**, 1455 (1987).

[10] P. Grütter, H. Mamin, and D. Rugar, *Magnetic force microscopy (MFM)*, in: *Scanning Tunneling Microscopy II,* H. Günterodt and R. Wiesendanger (editors), 151, Springer, Berlin, Heidelberg, New York (1992).

[11] K. Koike and K. Hayakawa, *Scanning Electron Microscope Observation of Magnetic Domains Using Spin-Polarized Secondary Electrons*, Jpn. J. Appl. Phys. **23**, L187 (1984).

[12] J. Unguris, G. G. Hembree, R. J. Celotta, and D. T. Pierce, *High-resolution magnetic microstructure imaging using secondary-electron spin polarization analysis in a scanning electron-microscope*, J. Microsc.-Oxf. **139**, RP1 (1985).

[13] M. Bode, M. Getzlaff, and R. Wiesendanger, *Spin-Polarized Vacuum Tunneling into the Exchange-Split Surface State of Gd(0001)*, Phys. Rev. Lett. **81**, 4256 (1998).

[14] M. Bode, *Spin-polarized scanning tunnelling microscopy*, Rep. Prog. Phys. **66**, 523 (2003).

[15] E. Feldtkeller and H. Thomas, *Struktur und Energie von Blochlinien in Dünnen Ferromagnetischen Schichten*, Phys. Kondens. Materie **8**, 8 (1965).

[16] T. Shinjo, T. Okuno, R. Hassdorf, K. Shigeto, and T. Ono, *Magnetic vortex core observation in circular dots of permalloy*, Science **289**, 930 (2000).

[17] A. Wachowiak, J. Wiebe, M. Bode, O. Pietzsch, M. Morgenstern, and R. Wiesendanger, *Direct observation of internal spin structure of magnetic vortex cores*, Science **298**, 577–580 (2002).

[18] E. Beaurepaire, J.-C. Merle, A. Daunois, and J.-Y. Bigot, *Ultrafast Spin Dynamics in Ferromagnetic Nickel*, Phys. Rev. Lett. **76**, 4250 (1996).

[19] A. A. Thiele, *Steady-State Motion of Magnetic Domains*, Phys. Rev. Lett. **30**, 230 (1973).

[20] D. L. Huber, *Dynamics of spin vortices in two-dimensional planar magnets*, Phys. Rev. B **26**, 231 (1982).

[21] B. E. Argyle, E. Terrenzio, and J. C. Slonczewski, *Magnetic Vortex Dynamics Using the Optical Cotton-Mouton Effect*, Phys. Rev. Lett. **53**, 190 (1984).

[22] J. P. Park, P. Eames, D. M. Engebretson, J. Berezovsky, and P. A. Crowell, *Imaging of spin dynamics in closure domain and vortex structures*, Phys. Rev. B **67**, 020403(R) (2003).

[23] S. B. Choe, Y. Acremann, A. Scholl, A. Bauer, A. Doran, J. Stöhr, and H. A. Padmore, *Vortex-core driven magnetization dynamics*, Science **304**, 420 (2004).

[24] R. H. Koch, J. G. Deak, D. W. Abraham, P. L. Trouilloud, R. A. Altman, Y. Lu, W. J. Gallagher, R. E. Scheuerlein, K. P. Roche, and S. S. P. Parkin, *Magnetization Reversal in Micron-Sized Magnetic Thin Films*, Phys. Rev. Lett. **81**, 4512 (1998).

[25] A. S. Arrott, *Magnetic random access memories, Brown's paradox and hysterons*, J. Magn. Magn. Mater. **258**, 25 (2003).

[26] M. Huber, J. Zweck, and D. Weiss, *Experimental observation of switching in ferromagnetic nanoscale double disks*, Phys. Rev. B **77**(5), 054407 (2008).

[27] B. Van Waeyenberge, A. Puzic, H. Stoll, K. W. Chou, T. Tyliszczak, R. Hertel, M. Fähnle, H. Brückl, K. Rott, G. Reiss, I. Neudecker, D. Weiss, C. H. Back, and G. Schütz, *Magnetic vortex core reversal by excitation with short bursts of an alternating field*, Nature **444**, 461 (2006).

[28] A. Thiaville, J. M. García, R. Dittrich, J. Miltat, and T. Schrefl, *Micromagnetic study of Bloch-point-mediated vortex core reversal*, Phys. Rev. B **67**, 094410 (2003).

[29] N. Kikuchi, S. Okamoto, O. Kitakami, Y. Shimada, S. G. Kim, Y. Otani, and K. Fukamichi, *Vertical bistable switching of spin vortex in a circular magnetic dot*, J. Appl. Phys. **90**(12), 6548–6549 (2001).

[30] T. Gerrits, H. A. M. van den Berg, J. Hohlfeld, L. Bar, and T. Rasing, *Ultrafast precessional magnetization reversal by picosecond magnetic field pulse shaping*, Nature **418**, 509 (2002).

[31] H. W. Schumacher, C. Chappert, R. C. Sousa, P. P. Freitas, and J. Miltat, *Quasiballistic Magnetization Reversal*, Phys. Rev. Lett. **90**, 017204 (2003).

[32] L. D. Landau and E. Lifshitz, *On the theory of the dispersion of magnetic permeability in ferromagnetic bodies*, Phys. Z. Sowjetunion **8**, 153 (1935).

[33] W. F. Brown, Jr., *Micromagnetics*, Interscience Publishers, John Wiley & Sons, New York, London (1963).

[34] R. Hertel, O. Fruchart, S. Cherifi, P. Jubert, S. Heun, A. Locatelli, and J. Kirschner, *Three-dimensional magnetic-flux-closure patterns in mesoscopic Fe islands*, Phys. Rev. B **72**, 214409 (2005).

[35] M. Yan, R. Hertel, and C. M. Schneider, *Calculations of three-dimensional magnetic normal modes in mesoscopic permalloy prisms with vortex structure*, Phys. Rev. B **76**, 094407 (2007).

[36] K. W. Urban, *Studying Atomic Structures by Aberration-Corrected Transmission Electron Microscopy*, Science **321**, 506 (2008).

[37] A. Vansteenkiste, K. W. Chou, M. Weigand, M. Curcic, V. Sackmann, T. Stoll, H.and Tyliszczak, G. Woltersdorf, G. Back, C. H.and Schüz, and B. Van Waeyenberge, *X-ray imaging of the dynamic magnetic vortex core deformation*, Nat. Phys. **5**, 332 (2009).

[38] G. Reiss, F. Schneider, J. Vancea, and H. Hoffmann, *Scanning tunneling microscopy on rough surfaces: Deconvolution of constant current images*, Appl. Phys. Lett. **57**, 867 (1990).

[39] J. S. Villarrubia, *Algorithms for Scanned Probe Microscope Image Simulation, Surface Reconstruction, and Tip Estimation*, J. Res. Natl. Inst. Stand. Technol. **102**, 425 (1997).

[40] R. Hertel. *Statische und dynamische Magnetisierung in Nanostrukturen.* Habilitationsschrift, Universität Halle-Wittenberg (2005).

[41] J. K. Ha, R. Hertel, and J. Kirschner, *Micromagnetic study of magnetic configurations in submicron permalloy disks*, Phys. Rev. B **67**, 224432 (2003).

[42] S. Cherifi, R. Hertel, J. Kirschner, H. Wang, R. Belkhou, A. Locatelli, S. Heun, A. Pavlovska, and E. Bauer, *Virgin domain structures in mesoscopic Co patterns: Comparison between simulation and experiment*, J. Appl. Phys. **98**, 043901 (2005).

[43] R. Hertel and H. Kronmüller, *Adaptive Finite Element Mesh Refinement Techniques in Three-Dimensional Micromagnetic Modeling*, IEEE Trans. Magn. **34**, 3922 (1998).

[44] V. Novosad, F. Y. Fradin, P. E. Roy, K. S. Buchanan, K. Y. Guslienko, and S. Bader, *Magnetic vortex resonance in patterned ferromagnetic dots*, Phys. Rev. B **72**, 024455 (2005).

[45] S. Kasai, Y. Nakatani, K. Kobayashi, H. Kohno, and T. Ono, *Current-Driven Resonant Excitation of Magnetic Vortices*, Phys. Rev. Lett. **97**, 107204 (2006).

[46] R. Hertel and C. M. Schneider, *Exchange explosions: Magnetization Dynamics During Vortex-Antivortex Annihilation*, Phys. Rev. Lett. **97**, 177202 (2006).

[47] R. Hertel, S. Gliga, M. Fähnle, and C. M. Schneider, *Ultrafast nanomagnetic toggle switching of vortex cores*, Phys. Rev. Lett. **98**, 117201 (2007).

[48] S. Gliga, R. Hertel, and C. M. Schneider, *Flipping magnetic vortex cores on the picosecond timescale*, Physica B **403**, 334 (2008).

[49] S. Gliga, M. Yan, R. Hertel, and C. M. Schneider, *Ultrafast dynamics of a magnetic antivortex: Micromagnetic simulations*, Phys. Rev. B **77**, 060404(R) (2008).

[50] S. Gliga, R. Hertel, and C. M. Schneider, *Switching a magnetic antivortex core with ultrashort field pulses*, J. Appl. Phys. **103**, 07B115 (2008).

[51] J. C. Slonczewski, *Current-driven excitation of magnetic multilayers*, J. Magn. Magn. Mater. **159**, L1 (1996).

[52] L. Berger, *Emission of spin waves by a magnetic multilayer traversed by a current*, Phys. Rev. B **54**, 9353 (1996).

[53] M. Kläui, C. A. F. Vaz, J. A. C. Bland, W. Wernsdorfer, G. Faini, E. Cambril, and L. J. Heyderman, *Domain wall motion induced by spin polarized currents in ferromagnetic ring structures*, Appl. Phys. Lett. **83**, 105 (2003).

[54] A. Yamaguchi, T. Ono, S. Nasu, K. Miyake, K. Mibu, and T. Shinjo, *Real-Space Observation of Current-Driven Domain Wall Motion in Submicron Magnetic Wires*, Phys. Rev. Lett. **92**, 077205 (2004).

[55] Z. Li and S. Zhang, *Domain-Wall Dynamics and Spin-Wave Excitations with Spin-Transfer Torques*, Phys. Rev. Lett. **92**, 207203 (2004).

[56] A. Thiaville, Y. Nakatani, J. Miltat, and Y. Suzuki, *Micromagnetic understanding of current-driven domain wall motion in patterned nanowires*, Europhys. Lett. **69**, 990 (2005).

[57] K. Yamada, S. Kasai, Y. Nakatani, K. Kobayashi, H. Kohno, A. Thiaville, and T. Ono, *Electrical switching of the vortex core in a magnetic disk*, Nature Mater. **6**, 355 (2007).

[58] Y. Liu, S. Gliga, R. Hertel, and C. M. Schneider, *Current–induced magnetic vortex core switching in a Permalloy nanodisk*, Appl. Phys. Lett. **91**, 112501 (2007).

[59] K.-S. Lee, S.-K. Kim, Y.-S. Yu, Y.-S. Choi, K. Y. Guslienko, H. Jung, and P. Fischer, *Universal Criterion and Phase Diagram for Switching a Magnetic Vortex Core in Soft Magnetic Nanodots*, Phys. Rev. Lett. **101**, 267206 (2008).

[60] P. Weiss, *L'hypothèse du champ moléculaire et la propriété ferromagnétique*, J. de Phys. Rad. **6**, 661 (1907).

[61] P. Weiss and G. Foex, *Le Magnétisme*, Armand Colin, Paris (1926).

[62] F. Bitter, *On inhomogeneities in the magnetization of ferromagnetic materials*, Phys. Rev. **38**, 1903 (1931).

[63] F. Bitter, *Experiments on the nature of ferromagnetism*, Phys. Rev. **41**, 507 (1932).

[64] F. Bloch, *Zur Theorie der Austausch problems und der Remanenzerscheinung der Feromagnetika*, Z. Phys. **74**, 295 (1932).

[65] W. F. Brown, *Magnetostatic Principles in Ferromagnetism*, North-Holland Publishing Co., Amsterdam (1962).

[66] E. Feldtkeller, *Mikromagnetisch stetige und unstetige Magnetisirungsverteilungen*, Z. Angew. Phys. **19**, 530 (1965).

[67] T. L. Gilbert, *A Lagrangian formulation of gyromagnetic equation of the magnetization field*, Phys. Rev. **100**, 1243 (1955).

[68] T. L. Gilbert, *A phenomenological theory of damping in ferromagnetic materials*, IEEE Trans. Magn. **40**, 3443 (2004).

[69] A. I. Liechtenstein, M. I. Katsnelson, V. P. Antropov, and V. A. Gubanov, *Local spin density functional approach to the theory of exchange interactions in ferromagnetic metals and alloys*, J. Magn. Magn. Mater. **67**, 65 (1987).

[70] M. Lubecka, L. J. Maksymowicz, and R. Zuberek, *Exchange-interaction constant of polycrystalline $CdCr_2Se_4$ thin films doped with In*, Phys. Rev. B **42**, 3926 (1990).

[71] D. J. Griffiths, *Introduction to Electrodynamics*, Prentice-Hall, New Jersey, 3rd. edition (1999).

[72] A. Aharoni, *Introduction to the Theory of Ferromagnetism*, Oxford Science Publications, Oxford Clarendon Press, Oxford, 2nd. edition (2000).

[73] W. F. Brown, *Criterion for Uniform Micromagnetization*, Phys. Rev. **105**, 1479 (1957).

[74] A. Aharoni, *Demagnetizing factors for rectangular ferromagnetic prisms*, J. Appl. Phys. **83**, 3432 (1998).

[75] L. Néel, *L'anisotropie superficielle des substances ferromagnétiques*, C. R. Acad. Sci. Paris **237**, 1468 (1953).

[76] D. Suess, T. Schrefl, and J. Fidler, *Reversal modes, thermal stability and exchange length in perpendicular recording media*, IEEE Trans. Magn. **37**, 1664 (2001).

[77] H. Kronmüller and M. Fähnle, *Micromagnetism and the Microstructure of Ferromagnetic Solids*, Cambridge University Press, Cambridge (2003).

[78] B. A. Lilley, *Energies and widths of domain boundaries in ferromagnetics*, Phil. Mag. **41**(7), 792 (1950).

[79] L. Néel, *Énergie des parois de Bloch dans les couches minces*, C. R. Acad. Sci. Paris **241**, 553–536 (1955).

[80] R. D. McMichael and M. J. Donahue, *Head to Head Domain Wall Structures in Thin Magnetic Strips*, IEEE Trans. Mag. **33**, 4167 (1997).

[81] J. E. E. Huber, D. O. Smith, and J. B. Goodenough, *Domain-Wall Structure in Permalloy Films*, J. Appl. Phys. **29**, 294 (1958).

[82] S. Middelhoek, *Domain Walls in Thin Ni–Fe Films*, J. Appl. Phys. **34**, 1054 (1963).

[83] R. P. Cowburn, D. K. Koltsov, A. O. Adeyeye, M. E. Welland, and D. M. Tricker, *Single-Domain Circular Nanomagnets*, Phys. Rev. Lett. **83**, 1042 (1999).

[84] J. Raabe, R. Pulwey, R. Sattler, T. Schweinböck, J. Zweck, and D. Weiss, *Magnetization pattern of ferromagnetic nanodisks*, J. Appl. Phys. **88**, 4437 (2000).

[85] M. Bode, O. Pietzsch, A. Kubetzka, W. Wulfhekel, D. McGrouther, S. McVitie, and J. N. Chapman, *Comment on 'Three-Dimensional, Spin-Resolved Structure of Magnetic Vortex and Antivortex States in Patterned Co Films Using Scanning Ion Microscopy with Polarization Analysis'*, Phys. Rev. Lett. **100**, 029703 (2008).

[86] N. A. Usov and S. E. Peschany, *Magnetization curling in a fine cylindrical particle*, J. Magn. Magn. Mater. **118**, L290 (1993).

[87] M. Mankos, J. M. Cowley, and M. R. Scheinfein, *Quantitative Micromagnetics at High Spatial Resolution Using Far-out-of-Focus STEM Electron Holography*, Phys. Status Solidi B **154**, 469 (1996).

[88] X. Liu, J. N. Chapman, S. McVitie, and C. D. W. Wilkinson, *Reversal mechanisms and metastable states in magnetic nanoelements*, J. Appl. Phys. **96**, 5173 (2004).

[89] M. Ammar, M. LoBue, E. Snoeck, M. Hÿtch, Y. Champion, R. Barrué, and F. Mazaleyrat, *A quantitative analysis of magnetic vortices in Permalloy nanoparticles characterized by electron holography*, J. Magn. Magn. Mater. **320**, e716 (2008).

[90] J. Stöhr and H. C. Siegmann, *Magnetism – From Fundamentals to Nanoscale Dynamics*, Springer-Verlag Berlin, Heidelberg (2006).

[91] A. S. Arrott, *Introduction to Micromagnetics*, in: *Ultrathin Magnetic Structures IV,* B. Heinrich and J. A. C. Bland (editors), 101, Springer, Berlin, Heidelberg (2005).

[92] E. V. Shuryak, *The QCD Vacuum, Hadrons and Superdense Matter*, World Scientific Publishing Company, Singapore (2004).

[93] G.-W. Chern, H. Youk, and O. Tchernyshyov, *Topological defects in flat nanomagnets: The magnetostatic limit*, J. Appl. Phys. **99**, 08Q505 (2006).

[94] K. Shigeto, T. Okuno, K. Mibu, and T. Shinjo, T.Ono, *Magnetic force microscopy observation of antivortex core with perpendicular magnetization in patterned thin film of permalloy*, Appl. Phys. Lett. **80**(22), 4190–4192 (2002).

[95] S. Hikami and T. Tsuneto, *Phase Transition of Quasi-Two Dimensional Planar System*, Prog. Theor. Phys. **63**, 387 (1980).

[96] B. Krüger, A. Drews, M. Bolte, U. Merkt, D. Pfannkuche, and G. Meier, *Vortices and antivortices as harmonic oscillators*, J. Appl. Phys. **103**, 07A501 (2008).

[97] A. A. Belavin and A. M. Polyakov, *Metastable states of two-dimensional isotropic ferromagnets*, JETP Letters **22**, 503 (1975).

[98] T. Senthil, A. Vishwanath, L. Balents, S. Sachdev, and M. P. A. Fisher, *Deconfined Quantum Critical Points*, Science **303**, 1490 (2004).

[99] W. Döring, *Point Singularities in Micromagnetism*, J. Appl. Phys. **39**, 1006 (1968).

[100] A. P. Malozemoff and J. C. Slonczewski, *Magnetic Domain Walls in Bubble Materials*, Academic Press, New York (1979).

[101] A. Landé, *Anomalous Zeeman effect*, Z. Phys **5**, 231 (1921).

[102] J. G. Wright, *Ferromagnetism in epitaxial F.C.C. iron films*, Phil. Mag. **24**, 217 (1971).

[103] B. Heinrich, *Spin Relaxation in Magnetic Metallic Layers and Multilayers*, in: *Ultrathin Magnetic Structures III,* B. Heinrich and J. A. C. Bland (editors), 143, Springer, Berlin, Heidelberg (2005).

[104] R. Kikuchi, *On the Minimum of Magnetization Reversal Time*, J. Appl. Phys. **27**, 1352 (1956).

[105] M. Kläui, P.-O. Jubert, R. Allenspach, A. Bischof, J. A. C. Bland, G. Faini, U. Rüdiger, C. A. F. Vaz, L. Vila, and C. Vouille, *Direct Observation of Domain-Wall Configurations Transformed by Spin Currents*, Phys. Rev. Lett. **95**, 026601 (2005).

[106] P.-O. Jubert, M. Kläui, A. Bischof, U. Rüdiger, and R. Allenspach, *Velocity of vortex walls moved by current*, J. Appl. Phys. **99**, 08G523 (2006).

[107] M. Hayashi, L. Thomas, Y. B. Bazaliy, C. Rettner, R. Moriya, X. Jiang, and S. S. P. Parkin, *Influence of Current on Field-Driven Domain Wall Motion in Permalloy Nanowires from Time Resolved Measurements of Anisotropic Magnetoresistance*, Phys. Rev. Lett. **96**, 197207 (2006).

[108] G. Tatara and H. Kohno, *Theory of Current-Driven Domain Wall Motion: Spin Transfer versus Momentum Transfer*, Phys. Rev. Lett. **92**, 086601 (2004).

[109] S. Zhang and Z. Li, *Roles of Nonequilibrium Conduction Electrons on the Magnetization Dynamics of Ferromagnets*, Phys. Rev. Lett. **93**, 127204 (2004).

[110] J. Xiao, A. Zangwill, and M. D. Stiles, *Spin-transfer torque for continuously variable magnetization*, Phys. Rev. B **73**, 054428 (2006).

[111] G. S. D. Beach, C. Knutson, C. Nistor, M. Tsoi, and J. L. Erskine, *Nonlinear Domain-Wall Velocity Enhancement by Spin-Polarized Electric Current*, Phys. Rev. Lett. **97**, 057203 (2006).

[112] M. D. Stiles, W. M. Saslow, M. J. Donahue, and A. Zangwill, *Adiabatic domain wall motion and Landau-Lifshitz damping*, Phys. Rev. B **75**, 214423 (2007).

[113] B. Krüger, D. Pfannkuche, M. Bolte, G. Meier, and U. Merkt, *Current-driven domain-wall dynamics in curved ferromagnetic nanowires*, Phys. Rev. B **75**, 054421 (2007).

[114] J. Fish and T. Belytschko, *A First Course in Finite Elements*, John Wiley & Sons, Chichester (2007).

[115] C. J. Garcia-Cervera, Z. Gimbutas, and E. Weinan, *Accurate numerical methods for micromagnetic simulations with general geometries*, J. Comp. Phys. **184**, 37–52 (2003).

[116] C. Dietrich, R. Hertel, M. Huber, D. Weiss, R. Schäfer, and J. Zweck, *Influence of perpendicular magnetic fields on the domain structure of permalloy microstructures grown on thin membranes*, Phys. Rev. B **77**, 174427 (2008).

[117] B. Delaunay, *Sur la sphère vide*, Bull. Acad. Sci. USSR, Classe Sci. Mat. Nat. **7**, 793 (1934).

[118] O. C. Zienkiewicz, R. L. Taylor, and J. Z. Zhu, *The Finite Element Method. Its Basis and Fundamentals*, Elsevier Butterworth Heinemann, Oxford, Burlington (2005).

[119] G. Voronoi, *Nouvelles applications des paramètres continus à la théorie des formes quadratiques. Premier Mémoire. Sur quelques propriétés des formes quadratiques positives parfaites*, J. Reine Angew. Math. **133**, 97 (1907).

[120] H. Si, *TetGen, a quality tetrahedral mesh generator and three-dimensional Delaunay triangulator*, WIAS Technical Report 9, Weierstrass Institute for Applied Analysis and Stochastics, (2004).

[121] C. Geuzaine and J.-F. Remacle, *Gmsh: A 3-D finite element mesh generator with built-in pre- and post-processing facilities*, Int. J. Num. Meth. Engng. **79**, 1309 (2009).

[122] T. Schrefl, J. Fidler, K. J. Kirk, and J. N. Chapman, *A Higher Order FEM-BEM Method for the Calculation of Domain Processes in Magnetic Nano-Elements*, IEEE Trans. Magn. **33**, 4182 (1997).

[123] W. Chen, D. R. Fredkin, and T. R. Koehler, *A new finite element method in micromagnetics*, IEEE Trans. Magn. **29**, 2124 (1993).

[124] G. T. Rado and J. R. Wertmann, *Spin-wave resonance in a ferromagnetic metal*, J. Phys. Chem. Sol. **11**(3-4), 315 (1959).

[125] D. R. Fredkin and T. R. Koehler, *Hybrid method for computing demagnetizing fields*, IEEE Trans. Magn. **26**, 415 (1990).

[126] T. R. Koehler and D. R. Fredkin, *Finite element methods for micromagnetics*, IEEE Trans. Magn. **28**, 1239 (1992).

[127] D. A. Lindholm, *Three-Dimensional Magnetostatic Fields from Point-Matched Integral Equations with Linearly Varying Scalar Ssources*, IEEE Trans. Magn. **20**, 2025 (1984).

[128] R. Hertel, *Oersted fields and current density profiles in spin-torque driven magnetization dynamics – Finite element modelling of realistic geometries*, arXiv:0804.4010 (2008).

[129] S. Kurz, O. Rain, and S. Rjasanow, *The adaptive cross-approximation technique for the 3D boundary-element method*, IEEE Trans. Magn. **38**, 421 (2002).

[130] T. Schrefl, G. Hrkac, S. Bance, D. Suess, O. Ertl, and J. Fidler, *Numerical Methods in Micromagnetics (Finite Element Method)*, in: *Handbook of Magnetism and Advanced Magnetic Materials, Vol. 2,* H. Kronmüller and S. Parkin (editors), 765, John Wiley & Sons, New York, London (2007).

[131] S. D. Cohen and A. C. Hindmarsh, *CVODE, a Stiff/Nonstiff ODE Solver in C*, Computers in Physics **10**, 138 (1996).

[132] C. H. Back, R. Allenspach, W. Weber, S. S. P. Parkin, D. Weller, E. L. Garwin, and H. C. Siegmann, *Minimum Field Strength in Precessional Magnetization Reversal*, Science **285**, 864 (1999).

[133] J. P. Park, P. Eames, D. M. Engebretson, J. Berezovsky, and P. A. Crowell, *Spatially Resolved Dynamics of Localized Spin-Wave Modes in Ferromagnetic Wires*, Phys. Rev. Lett. **89**, 277201 (2002).

[134] L. Giovannini, F. Montoncello, F. Nizzoli, G. Gubbiotti, G. Carlotti, T. Okuno, T. Shinjo, and M. Grimsditch, *Spin excitations of nanometric cylindrical dots in vortex and saturated magnetic states*, Phys. Rev. B **70**, 172404 (2004).

[135] J. Raabe, C. Quitmann, C. H. Back, F. Nolting, S. Johnson, and C. Buehler, *Quantitative analysis of magnetic excitations in Landau flux-closure structures using synchrotron-radiation microscopy*, Phys. Rev. Lett. **94**(21), 217204 (2005).

[136] K. S. Buchanan, P. E. Roy, M. Grimsditch, F. Y. Fradin, K. Y. Guslienko, S. D. Bader, and V. Novosad, *Soliton-pair dynamics in patterned ferromagnetic ellipses*, Nat. Phys. **1**, 172 (2005).

[137] K. W. Chou, A. Puzic, H. Stoll, D. Dolgos, G. Schütz, B. V. Waeyenberge, A. Vansteenkiste, T. Tyliszczak, G. Woltersdorf, and C. H. Back, *Direct observation of the vortex core magnetization and its dynamics*, Appl. Phys. Lett. **90**, 202505 (2007).

[138] D. L. Huber, *Equation of motion of a spin vortex in a two-dimensional planar magnet*, J. Appl. Phys. **53**, 1899 (1982).

[139] F. G. Mertens and A. R. Bishop, *Dynamics of Vortices in Two-Dimensional Magnets*, in: *Nonlinear Science at the Dawn of the 21st Century,* P. L. Christiansen, M. P. Sorensen, and A. Scott (editors), 137, Springer, Berlin (2000).

[140] G. M. Wysin, *Magnetic vortex mass in two-dimensional easy-plane magnets*, Phys. Rev. B **54**, 15156 (1996).

[141] K. Y. Guslienko, B. A. Ivanov, V. Novosad, Y. Otani, H. Shima, and K. Fukamichi, *Eigenfrequencies of vortex state excitations in magnetic submicron-size disks*, Appl. Phys. Lett. **91**, 8037 (2002).

[142] K. Y. Guslienko, V. Novosad, Y. Otani, and K. Fukamichi, *Field evolution of magnetic vortex state in ferromagnetic disks*, Appl. Phys. Lett. **78**, 3848 (2001).

[143] K. L. Metlov and K. Y. Guslienko, *Stability of magnetic vortex in soft magnetic nano-sized circular cylinder*, J. Magn. Magn. Mater. **242-245**, 1015 (2002).

[144] K. Y. Guslienko, X. F. Han, D. J. Keavney, R. Divan, and S. D. Bader, *Magnetic Vortex Core Dynamics in Cylindrical Ferromagnetic Dots*, Phys. Rev. Lett. **96**, 067205 (2006).

[145] A. A. Thiele, *Applications of the gyrocoupling vector and dissipation dyadic in the dynamics of magnetic domains*, J. Appl. Phys. **45**, 377 (1974).

[146] K. Y. Guslienko, *Low-frequency vortex dynamic susceptibility and relaxation in mesoscopic ferromagnetic dots*, Appl. Phys. Lett. **89**, 022510 (2006).

[147] K.-S. Lee and S.-K. Kim, *Gyrotropic linear and nonlinear motions of a magnetic vortex in soft magnetic nanodots*, Appl. Phys. Lett. **91**, 132511 (2007).

[148] V. L. Pokrovskii and G. V. Uimin, *Dynamics of vortex pairs in a two-dimensional magnetic material*, JETP Lett. **41**, 128 (1985).

[149] K. Y. Guslienko, private communication (2008).

[150] Z. Liu, F. Giesen, X. Zhu, R. D. Sydora, and M. R. Freeman, *Spin Wave Dynamics and the Determination of Intrinsic Damping in Locally Excited Permalloy Thin Films*, Phys. Rev. Lett. **98**, 087201 (2007).

[151] V. Novosad, M. Grimsditch, K. Y. Guslienko, P. Vavassori, Y. Otani, and S. D. Bader, *Spin excitations of magnetic vortices in ferromagnetic nanodots*, Phys. Rev. B **66**, 052407 (2002).

[152] R. Hertel and J. Kirschner, *Resonant modes of vortex structures in soft-magnetic nanodiscs*, J. Magn. Magn. Mater. **272-276**, 655 (2004).

[153] Y. Acremann, C. H. Back, M. Buess, O. Portmann, A. Vaterlaus, D. Pescia, and H. Melchior, *Imaging Precessional Motion of the Magnetization Vector*, Science **290**, 492–495 (2000).

[154] M. Buess, R. Höllinger, T. Haug, K. Perzlmaier, U. Krey, D. Pescia, M. R. Scheinfein, D. Weiss, and C. H. Back, *Fourier Transform Imaging of Spin Vortex Eigenmodes*, Phys. Rev. Lett. **93**, 077207 Aug (2004).

[155] M. Buess, T. P. J. Knowles, R. Hollinger, T. Haug, U. Krey, D. Weiss, D. Pescia, M. R. Scheinfein, and C. H. Back, *Excitations with negative dispersion in a spin vortex*, Phys. Rev. B **71**, 104415 (2005).

[156] K. Guslienko, K.-S. Lee, and S.-K. Kim, *Dynamic Origin of Vortex Core Switching in Soft Magnetic Nanodots*, Phys. Rev. Lett. **100**, 027203 (2008).

[157] W. Döring, *Über die Trägheit der Wände zwischen Weißchen Bezirken*, Z. Naturforsch. **3a**, 373 (1948).

[158] N. Papanicolaou and P. N. Spathis, *Semitopological solitons in planar ferromagnets*, Nonlinearity **12**, 285 (1999).

[159] S. Komineas, *Rotating Vortex Dipoles in Ferromagnets*, Phys. Rev. Lett. **99**, 117202 (2007).

[160] S. Komineas and N. Papanicolaou, *Transmutation of momentum into position in magnetic vortices*, New J. Phys. **10**, 043021 (2008).

[161] K.-S. Lee, B.-W. Kang, Y.-S. Yu, and S.-K. Kim, *Vortex–antivortex pair driven magnetization dynamics studied by micromagnetic simulations*, Appl. Phys. Lett. **85**, 1568–1570 (2005).

[162] K. Y. Guslienko, *Magnetic Vortex State Stability, Reversal and Dynamics in Restricted Geometries*, Journal of Nanoscience and Nanotechnology **8**, 2745 (2008).

[163] K.-S. Lee, S. Choi, and S.-K. Kim, *Radiation of spin waves from magnetic vortex cores by their dynamic motion and annihilation process*, Appl. Phys. Lett. **87**, 192502 (2005).

[164] S. Choi, K.-S. Lee, K. Y. Guslienko, and S.-K. Kim, *Strong Radiation of Spin Waves by Core Reversal of a Magnetic Vortex and Their Wave Behaviors in Magnetic Nanowire Waveguides*, Phys. Rev. Lett. **98**, 087205 (2007).

[165] O. A. Tretiakov and O. Tchernyshyov, *Vortices in thin ferromagnetic films and the skyrmion number*, Phys. Rev. B **75**, 012408 (2007).

[166] H.-B. Braun, *Nucleation in ferromagnetic nanowires—magnetostatics and topology*, J. Appl. Phys. **85**, 6172–6174 (1999).

[167] A. N. Bogdanov and U. K. Rößler, *Chiral Symetry Breaking in Magnetic Thin Films and Multilayers*, Phys. Rev. Lett. **87**, 037203 (2001).

[168] U. K. Rößler, A. N. Bogdanov, and C. Pfleiderer, *Spontaneous skyrmion ground states in magnetic metals*, Nature **442**, 797 (2006).

[169] M. Gleiser and J. Thorarinson, *Phase transition in U(1) configuration space: Oscillons as remnants of vortex-antivortex annihilation*, Phys. Rev. D **76**, 041701 (2007).

[170] T. Okuno, K. Shigeto, T. Ono, K. Mibu, and T. Shinjo, *MFM study of magnetic vortex cores in circular permalloy dots: behavior in external field*, J. Magn. Magn. Mater. **240**, 1 (2002).

[171] R. Höllinger, A. Killinger, and U. Krey, *Statics and fast dynamics of nanomagnets with vortex structure*, J. Magn. Magn. Mater. **261**, 168 (2003).

[172] M. Weigand, B. V. Waeyenberge, A. Vansteenkiste, M. Curcic, V. Sackmann, H. Stoll, T. Tyliszczak, K. Kaznatcheev, D. Bertwistle, G. Woltersdorf, C. H. Back, and G. Schütz, *Vortex Core Switching by Coherent Excitation with Single In-Plane Magnetic Field Pulses*, Phys. Rev. Lett. **102**, 077201 (2009).

[173] T. Eimüller, P. Fischer, M. Köhler, M. Scholz, P. Guttmann, G. Denbeaux, S. Glück, G. Bayreuther, G. Schmahl, D. Attwood, and G. Schütz, *Transmission X-ray microscopy using X-ray magnetic circular dichroism*, Appl. Phys. A-Mater. **73**, 697 (2001).

[174] H. Stoll, A. Puzic, B. van Waeyenberge, P. Fischer, J. Raabe, M. Buess, T. Haug, R. Höllinger, C. Back, D. Weiss, and G. Denbeaux, *High-resolution imaging of fast magnetization dynamics in magnetic nanostructures*, Appl. Phys. Lett. **84**, 3328 (2004).

[175] J. O. Rantschler, P. J. Chen, A. S. Arrott, R. D. McMichael, W. F. Egelhoff, and B. B. Maranville, *Surface anisotropy orf permalloy in NM/NiFe/NM multilayers*, J. Appl. Phys. **97**, 10J113 (2005).

[176] N. D. Rizzo, T. J. Silva, and A. B. Kos, *Relaxation Times for Magnetization Reversal in a High Coercivity Magnetic Thin Film*, Phys. Rev. Lett. **83**, 4876 (1999).

[177] Q. F. Xiao, J. Rudge, E. Girgis, J. Kolthammer, B. C. Choi, Y. K. Hong, and G. W. Donohoe, *Dynamics of magnetic vortex core switching in Fe nanodisks by applying in-plane magnetic field pulse*, J. Appl. Phys. **102**, 103904 (2007).

[178] A. Neudert, J. McCord, R. Schäfer, and L. Schültz, *Subnanosecond vortex transformation in ferromagnetic thin film elements observed by stroboscopic wide-field Kerr microscopy*, J. Appl. Phys. **97**, 10E701 (2005).

[179] A. Neudert, J. McCord, R. Schafer, and L. Schültz, *Domain-wall transformation by high–frequency magnetic fields*, Phys. Rev. B **75**, 172404 (2007).

[180] A. Neudert, J. McCord, R. Schäfer, R. Kaltofen, I. Mönch, H. Vinzelberg, and L. Schultz, *Bloch–line generation in cross–tie walls by fast magnetic–field pulses*, J. Appl. Phys. **99**, 08F302 (2006).

[181] K. Kuepper, M. Buess, J. Raabe, C. Quitmann, and J. Fassbender, *Dynamic Vortex-Antivortex Interaction in a Single Cross-Tie Wall*, Phys. Rev. Lett. **99**, 167202 (2007).

[182] H. Wang and C. E. Campbell, *Spin dynamics of a magnetic antivortex: Micromagnetic simulations*, Phys. Rev. B **76**, 220407(R) (2007).

[183] R. Hertel, W. Wulfhekel, and J. Kirschner, *Domain-wall Induced Phase Shifts in Spin Waves*, Phys. Rev. Lett. **93**, 257202 (2004).

[184] W. E. Lorensen and H. E. Cline, *Marching Cubes: A High Resolution 3D surface Construction Algorithm*, Comp. Graph. **21**, 163 (1987).

[185] H. Müller and M. Wehle, *Visualization of Implicit Surfaces Using Adaptive Tetrahedrizations*, in: *Scientific Visualization,* H. Hagen, G. M. Nielson, and F. H. Post (editors), 243. IEEE Computer Society (1997).

[186] M. Kläui, C. A. F. Vaz, W. Wernsdorfer, E. Bauer, S. Cherifi, S. Heun, A. Locatelli, G. Faini, E. Cambril, L. J. Heyderman, and J. A. C. Bland, *Domain wall behaviour at constrictions in ferromagnetic ring structures*, Physica B **343**, 343 (2004).

[187] P. E. Roy, J. H. Lee, T. Trypiniotis, D. Anderson, G. A. C. Jones, D. Tse, and C. H. W. Barnes, *Antivortex domain walls observed in permalloy rings via magnetic force microscopy*, Phys. Rev. B **79**, 060407 (2009).

[188] A. Drews, B. Krüger, M. Bolte, and G. Meier, *Current- and field-driven magnetic antivortices*, Phys. Rev. B **77**, 094413 (2008).

[189] M. Buess, J. Raabe, K. Perzlmaier, C. H. Back, and C. Quitmann, *Interaction of magnetostatic excitations with 90° domain walls in micrometer-sized permalloy squares*, Phys. Rev. B **74**, 100404(R) (2006).

[190] L. J. Heyderman, H. H. Solak, F. Nolting, and C. Quitmann, *Fabrication of nanoscale antidot arrays and magnetic observations using x-ray photoemission electron microscopy*, J. Appl. Phys. **95**, 6651–6653 (2004).

[191] J. Shi, *Magnetic Switching in High-Density MRAM*, in: *Ultrathin Magnetic Structures IV,* B. Heinrich and J. A. C. Bland (editors), 177, Springer, Berlin, Heidelberg (2005).

[192] L. Savtchenko, B. N. Engel, N. D. Rizzo, M. F. Deherrera, and J. A. Janesky. *Method of writing to scalable magnetoresistance random access memory element*, US Patent 6545906B1 (2003).

[193] J. Shibata, Y. Nakatani, G. Tatara, H. Kohno, and Y. Otani, *Current-induced magnetic vortex motion by spin-transfer torque*, Phys. Rev. B **73**, 020403(R) (2006).

[194] T. Ishida, T. Kimura, and Y. Otani, *Current–induced vortex displacement and annihilation in a single permalloy disk*, Phys. Rev. B **74**, 014424 (2006).

[195] L. Berger, *Possible existence of a Josephson effect in ferromagnets*, Phys. Rev. B **33**, 1572 (1986).

[196] J. Shibata, Y. Nakatani, G. Tatara, H. Kohno, and Y. Otani, *Magnetic vortex dynamics induced by spin-transfer torque*, J. Magn. Magn. Mater. **310**, 2041 (2007).

[197] Y. Gaididei, D. D. Sheka, and F. G. Mertens, *Controllable switching of vortex chirality in magnetic nanodisks by a field pulse*, Appl. Phys. Lett. **92**, 012503 (2008).

[198] B. C. Choi, J. Rudge, E. Girgis, J. Kolthammer, Y. K. Hong, and A. Lyle, *Spin-current pulse induced switching of vortex chirality in permalloy/Cu/Co nanopillars*, Appl. Phys. Lett. **91**, 022501 (2007).

[199] M. Bolte, G. Meier, B. Krüger, A. Drews, R. Eiselt, L. Bocklage, S. Bohlens, T. Tyliszczak, A. Vansteenkiste, B. V. Waeyenberge, K. W. Chou, A. Puzic, and H. Stoll, *Time-Resolved X-Ray Microscopy of Spin-Torque-Induced Magnetic Vortex Gyration*, Phys. Rev. Lett. **100**, 176601 (2008).

[200] S. Kasai, P. Fischer, M.-Y. Im, K. Yamada, Y. Nakatani, K. Kobayashi, H. Kohno, and T. Ono, *Probing the Spin Polarization of Current by Soft X-Ray Imaging of Current-Induced Magnetic Vortex Dynamics*, Phys. Rev. Lett. **101**, 237203 (2008).

[201] K. Yamada, S. Kasai, Y. Nakatani, K. Kobayashi, and T. Ono, *Switching magnetic vortex core by a single nanosecond current pulse*, Appl. Phys. Lett. **93**, 152502 (2008).

[202] D. D. Sheka, Y. Gaididei, and F. G. Mertens, *Current induced switching of vortex polarity in magnetic nanodisks*, Appl. Phys. Lett. **91**, 082509 (2007).

[203] S.-K. Kim, Y.-S. Choi, K.-S. Lee, K. Y. Guslienko, and D.-E. Jeong, *Electric-current-driven vortex-core reversal in soft magnetic nanodots*, Appl. Phys. Lett. **91**, 082506 (2007).

[204] S.-K. Kim, K.-S. Lee, Y.-S. Yu, and Y.-S. Choi, *Reliable low-power control of ultrafast vortex-core switching with the selectivity in an array of vortex states by in-plane circular-rotational magnetic fields and spin-polarized currents*, Appl. Phys. Lett. **92**, 022509 (2008).

[205] S. Bohlens, B. Krüger, A. Drews, M. Bolte, G. Meier, and D. Pfannkuche, *Current controlled random-access memory based on magnetic vortex handedness*, Appl. Phys. Lett. **93**, 142508 (2008).

[206] N. L. Schryer and L. R. Walker, *The motion of 180° domain walls in uniform dc magnetic fields*, J. Appl. Phys. **45**, 5406 (1974).

[207] J. C. Slonczewski, *Theory of domain-wall motion in magnetic films and platelets*, J. Appl. Phys. **44**, 1759 (1973).

[208] A. Zee, *Quantum Field Theory in a Nutshell*, Princeton University Press (2003).

[209] T. S. Machado, T. G. Rappoport, and L. C. Sampaio, *Static and dynamic properties of vortices in anisotropic magnetic disks*, Appl. Phys. Lett. **93**, 112507 (2008).

[210] J. Schwinger, *On Gauge Invariance and Vacuum Polarization*, Phys. Rev. **82**, 664 (1951).

[211] P. M. Derlet, H. S. Perlman, and G. J. Troup, *Stimulated Vacuum Pair Production in a Focused Laser Field*, Aust. J. Phys. **50**, 803 (1997).

[212] E. Brezin and C. Itzykson, *Pair Production in Vacuum by an Alternating Field*, Phys. Rev. D **2**, 1191 (1970).

[213] K. Dietz and M. Pröbsting, *The structure of the QED vacuum and electron - positron pair production in super-intense, pulsed laser fields*, J. Phys. B: At. Mol. Opt. Phys. **31**, L409 (1998).

[214] A. Ringwald, *Pair production from vacuum at the focus of an X-ray free electron laser*, Phys. Lett. B **510**, 107 (2001).

[215] P. Barpanda, T. Kasama, R. E. Dunin-Borkowski, M. R. Scheinfein, and A. S. Arrott, *Evolution and propagation of magnetic vortices in chains of Permalloy nanospheres*, J. Appl. Phys. **99**, 08G103 (2006).

[216] A. S. Arrott and R. Hertel, *Formation and transformation of vortex structures in soft ferromagnetic ellipsoids*, J. Appl. Phys. **103**, 07E739 (2008).

[217] J. C. Slonczewski, *Excitation of spin waves by an electric current*, J. Magn. Magn. Mater. **195**, 261 (1999).

[218] W. H. Rippard, M. R. Pufall, S. Kaka, S. E. Russek, and T. J. Silva, *Direct-Current Induced Dynamics in $Co_{90}Fe_{10}/Ni_{80}Fe_{20}$ Point Contacts*, Phys. Rev. Lett. **92**, 027201 (2004).

[219] F. B. Mancoff, N. D. Rizzo, B. N. Engel, and S. Tehrani, *Area dependence of high-frequency spin-transfer resonance in giant magnetoresistance contacts up to 300 nm diameter*, Appl. Phys. Lett. **88**, 112507 (2006).

[220] M. R. Pufall, W. H. Rippard, M. L. Schneider, and S. E. Russek, *Low-field current-hysteretic oscillations in spin-transfer nanocontacts*, Phys. Rev. B **75**, 140404 (2007).

[221] M. A. Hoefer and T. J. Silva, *Spin momentum transfer and Oersted field induce a vortex nano-oscillator in thin ferromagnetic film devices*, arXiv:cond-mat/0609030v2 (2007).

[222] D. V. Berkov and N. L. Gorn, *Non-linear magnetization dynamics in nanodevices induced by a spin-polarized current: micromagnetic simulation*, J. Phys. D **41**, 164013 (2008).

[223] G. Finocchio, O. Ozatay, L. Torres, R. A. Buhrman, D. C. Ralph, and B. Azzerboni, *Spin-torque-induced rotational dynamics of a magnetic vortex dipole*, Phys. Rev. B **78**, 174408 (2008).

# Publications

## Papers

[10] A. Kákay, R. Hertel, **S. Gliga**, R. Lehndorff, D.E. Bürgler, and C. M. Schneider
"Oersted-field induced blue-shift effect in spin-torque-driven Fe nanomagnet oscillators"
In preparation

[9] Ming Yan, Attila Kákay, **Sebastian Gliga**, Riccardo Hertel
"Beating the Walker limit with massless domain walls in cylindrical nanowires"
Accepted for publication in Physical Review Letters (2009)

[8] R. Lehndorff, D. E. Bürgler, **S. Gliga**, R. Hertel, P. Grünberg, Z. Celinski and C. M. Schneider
"Magnetization dynamics in spin torque nano-oscillators: Vortex state versus uniform state"
Physical Review B 80, 054412 (2009)

[7] Yaowen Liu, Zhiwei Hou, **Sebastian Gliga**, and Riccardo Hertel
"Influence of the dynamic dipolar interaction on the current-induced core switch in vortex pairs"
Physical Review B 79, 104435 (2009)

[6] **S. Gliga**, R. Hertel, and C. M. Schneider
"Switching a magnetic antivortex core with ultrashort field pulses"
Journal of Applied Physics 103, 07B115 (2008)

[5] **Sebastian Gliga**, Ming Yan, Riccardo Hertel, and Claus M. Schneider
"Ultrafast dynamics of a magnetic antivortex: Micromagnetic simulations"
Physical Review B 77, 060404(R) (2008)

- Selected for the March 2008 issue of the Virtual Journal of Ultrafast Science

[4] **S. Gliga**, R. Hertel, C.M. Schneider
"Flipping magnetic vortex cores on the picosecond time scale"
Physica B 403, 334 (2008)

[3] Y. Liu, **S. Gliga**, R. Hertel, and C. M. Schneider
"Current-induced magnetic vortex core switching in a Permalloy nanodisk"
Applied Physics Letters 91, 112501 (2007)

- Featured on the Applied Physics Letters cover, 10 September 2007 issue
- Among the top 10 most downloaded Applied Physics Letters articles, September 2007

- Selected for the September 24 2007 issue of Virtual Journal of Nanoscale Science and Technology

[2] G. Sarau, **S. Gliga**, R. Hertel, and C. M. Schneider
"Magnetization Reversal of Micron-Scale Cobalt Structures With a Nanoconstriction"
IEEE Transactions on Magnetics 43, 2854 (2007)

[1] R. Hertel, S. Gliga, M. Fähnle, and C. M. Schneider
"Ultrafast Nanomagnetic Toggle Switching of Vortex Cores"
Physical Review Letters 98, 117201 (2007)

- Featured in Nature Nanotechnology 2, 206 (2007) (News and Views) and in Physik Journal 6 (1), 17 (2007)
- Selected for the April 2007 issue of Virtual Journal of Ultrafast Science
- Selected for the March 26, 2007 issue of Virtual Journal of Nanoscale Science and Technology
- Press release of the Research Center Jülich:

  `http://www.fz-juelich.de/portal/index.php?index=163&jahr=2007&cmd=show&mid=460`

## Conferences

[11] "Micromagnetic study of field-induced vortex-antivortex pair creation in ferromagnetic thin-film elements" (invited talk)
**S. Gliga**, R. Hertel
3rd International Symposium on Vortex Dynamics, Hamburg, Germany; November 29-December 2, 2009

[10] "Energy thresholds in current-induced vortex core switching processes" (poster)
**S. Gliga**, R. Hertel
Advances in Magnetic Nanostructures, Vail, USA; October 4-9, 2009

[9] "Stimulated vortex-antivortex pair creation in ferromagnetic thin film elements" (talk)
**S. Gliga**, A. Kákay, R. Hertel, C. M. Schneider
73rd Annual Meeting of the DPG (German Physical society) and DPG Spring Meeting of the Condensed Matter Division, Dresden, Germany; March 22 – 27, 2009

[8] "Energy thresholds in current-induced vortex core switching" (talk: Best presentation award)

**S. Gliga**, A. Kákay, Y. Liu, R. Hertel, C. M. Schneider
Joint European Magnetic Symposia 2008, Dublin, Ireland; September 14 – 19, 2008

[7] "Energy thresholds in current-induced vortex core switching" (poster)
**S. Gliga**, Y. Liu, R. Hertel, C. M. Schneider
Workshop on high temporal and spatial resolution studies of magnetic nanostructures Augustw, Poland; June 27 – July 2, 2008

[6] "Resonant and non-resonant current-induced vortex core switching" (talk)
**S. Gliga**, Y. Liu, R. Hertel, C. M. Schneider
72nd Annual Meeting of the DPG (German Physical society) and DPG Spring Meeting of the Condensed Matter Division, Berlin, Germany; February 25 – 29, 2008

[5] "Ultrafast dynamics of a magnetic antivortex" (poster)
**S. Gliga**, R. Hertel, C. M. Schneider
Dreikönigstreffen Magnetismus '08 – New Concepts in Spin Dynamics, Bad Honnef, Germany; January 7 - 9, 2008

[4] "Resonant and non-resonant current-induced vortex core switching" (talk)
**S. Gliga**, Y. Liu, R. Hertel, C. M. Schneider
The 52nd Magnetism and Magnetic Materials Conference, Tampa, USA; November 5 – 9, 2007

[3] "Ultrafast dynamics of a magnetic antivortex" (poster)
**S. Gliga**, R. Hertel, C. M. Schneider
The 52nd Magnetism and Magnetic Materials Conference, Tampa, USA; November 5 – 9, 2007

[2] "Flipping magnetic vortex cores on the picosecond time scale" (talk)
**S. Gliga**, R. Hertel, C. M. Schneider
6th International Symposium on Hysteresis Modeling and Micromagnetics: HMM-2007, Naples, Italy; June 4 – 6, 2007

[1] "Switching magnetic vortices on the picosecond timescale" (talk)
**S. Gliga**, R. Hertel, C. M. Schneider
71st Annual Meeting of the Deutsche Physikalische Gesellschaft (German Physical society) and DPG Spring meeting of the Condensed Matter Division, Regensburg, Germany; March 26 – 30, 2007

## Seminars (invited)

[5] "Micromagnetic investigations of current and field-induced vortex core dynamics"

University of Colorado at Colorado Springs, Colorado Springs, USA; October 9, 2009

[4] "Micromagnetic investigations of current and field-induced vortex core dynamics"
Radboud University, Nijmegen, The Netherlands; December 19, 2008

[3] "Micromagnetic investigations of current and field-induced vortex core dynamics"
Centre for Nanoscale Materials, Argonne National Laboratory, Argonne, USA; November 16, 2008

[2] "Micromagnetic investigations of current and field-induced vortex core dynamics"
Centre for the Physics of Materials Seminar, McGill University, Montréal, Canada; September 4, 2008

[1] "Flipping magnetic vortices on the picosecond time scale"
Centre for the Physics of Materials Seminar, McGill University, Montréal, Canada; December 15, 2006

# Acknowledgements

This PhD thesis was performed at the Institute of Solid State Research (IFF) at the Forschungszentrum Jülich. From the moment I arrived in Jülich, I felt welcome at the IFF, and in particular in the institute of Electronic Properties. It is now a pleasure to thank all those who have contributed to this exciting journey.

First and foremost, I wish to express my deep gratitude to Dr. Riccardo Hertel, who has introduced me to micromagnetism and has guided me throughout these years. Thank you Riccardo for your constant support, motivation and kindness. You always made time for me to discuss vortex dynamics and many other topics. During these years, your unabated interest in my work has been a source of motivation. It has been a privilege to perform my PhD under your supervision.

I sincerely thank Prof. Dr. Claus M. Schneider for giving me the opportunity to perform this thesis in his institute. I gratefully acknowledge his confidence in me from the moment we first met and his constant support over the years. He has always made me feel at home at the IFF-9.

I wish to thank Dr. Attila Kákay for being such an outstanding physicist and an incomparable friend. He has always taken the time to explain to me in depth the concepts, which I sometimes struggled with. Attila: I owe you so much.

I am grateful to Dr. Ming Yan for the many discussions we had and for his insight into the dynamics of spin waves.

I heartily thank Prof. Dr. Anthony Arrott who has been a great source of knowledge and inspiration for me every time he visited Jülich. I always remember the discussions we had riding our bikes back home in the evenings.

I warmly thank Prof. Dr. Yaowen Liu for the very nice collaboration which has extended beyond his stay in Jülich as a Humboldt Fellow. I am indebted to him for some of the ideas which have been developed in this thesis.

My gratitude goes to Prof. Dr. Peter Grünberg for having welcomed me in his house at a difficult moment of my stay in Jülich and for being a source of inspiration.

I also wish to thank Prof. Dr. Michael Farle and Prof. Dr. Hans Peter Oepen for refereeing this thesis. It is an honor for me.

I am thankful to Dr. Phivos Mavropoulos for taking the time to help me with analytic aspects of vortex dynamics and for his incomparable sense of humor.

**Acknowledgements**

I am grateful to Jutta Gollnick who has often guided me through the research center's administrative labyrinth. Thank you Jutta for showing me that there was life in Jülich and for all the nice moments spent together.

I thank Dipl. Ing. Franz-Joseph Köhne for his advice and for helping me navigate some of the problems of everyday life in Jülich.

To all the colleagues and friends I met in Jülich and who have accompanied me on this journey – Wonki Choi, DooSeok Jeong, Sandipan Mohanty, Robert Weng, Andrea Borga, Rohit Soni – and all the members of the "Fantastic Jülich" group: thank you for the great times.

Finally, this thesis was only possible thanks to my mother and father Ligia and Basile who always gave me their unconditional love and support and had unwavering faith in me, to my girlfriend Weronika who gave me such love, strength and motivation and to my younger brothers Theodore, Alexander and Andrew. To you I dedicate this thesis.

Sebastian Gliga

Jülich, June 30, 2009

1. **Einsatz von multispektralen Satellitenbilddaten in der Wasserhaushalts- und Stoffstrommodellierung – dargestellt am Beispiel des Rureinzugsgebietes**
   von C. Montzka (2008), XX, 238 Seiten
   ISBN: 978-3-89336-508-1

2. **Ozone Production in the Atmosphere Simulation Chamber SAPHIR**
   by C. A. Richter (2008), XIV, 147 pages
   ISBN: 978-3-89336-513-5

3. **Entwicklung neuer Schutz- und Kontaktierungsschichten für Hochtemperatur-Brennstoffzellen**
   von T. Kiefer (2008), 138 Seiten
   ISBN: 978-3-89336-514-2

4. **Optimierung der Reflektivität keramischer Wärmedämmschichten aus Yttrium-teilstabilisiertem Zirkoniumdioxid für den Einsatz auf metallischen Komponenten in Gasturbinen**
   von A. Stuke (2008), X, 201 Seiten
   ISBN: 978-3-89336-515-9

5. **Lichtstreuende Oberflächen, Schichten und Schichtsysteme zur Verbesserung der Lichteinkopplung in Silizium-Dünnschichtsolarzellen**
   von M. Berginski (2008), XV, 171 Seiten
   ISBN: 978-3-89336-516-6

6. **Politikszenarien für den Klimaschutz IV – Szenarien bis 2030**
   hrsg.von P. Markewitz, F. Chr. Matthes (2008), 376 Seiten
   ISBN 978-3-89336-518-0

7. **Untersuchungen zum Verschmutzungsverhalten rheinischer Braunkohlen in Kohledampferzeugern**
   von A. Schlüter (2008), 164 Seiten
   ISBN 978-3-89336-524-1

8. **Inorganic Microporous Membranes for Gas Separation in Fossil Fuel Power Plants**
   by G. van der Donk (2008), VI, 120 pages
   ISBN: 978-3-89336-525-8

9. **Sinterung von Zirkoniumdioxid-Elektrolyten im Mehrlagenverbund der oxidkeramischen Brennstoffzelle (SOFC)**
   von R. Mücke (2008), VI, 165 Seiten
   ISBN: 978-3-89336-529-6

10. **Safety Considerations on Liquid Hydrogen**
    by K. Verfondern (2008), VIII, 167 pages
    ISBN: 978-3-89336-530-2

11. **Kerosinreformierung für Luftfahrtanwendungen**
    von R. C. Samsun (2008), VII, 218 Seiten
    ISBN: 978-3-89336-531-9

12. **Der 4. Deutsche Wasserstoff Congress 2008 – Tagungsband**
    hrsg. von D. Stolten, B. Emonts, Th. Grube (2008), 269 Seiten
    ISBN: 978-3-89336-533-3

13. **Organic matter in Late Devonian sediments as an indicator for environmental changes**
    by M. Kloppisch (2008), XII, 188 pages
    ISBN: 978-3-89336-534-0

14. **Entschwefelung von Mitteldestillaten für die Anwendung in mobilen Brennstoffzellen-Systemen**
    von J. Latz (2008), XII, 215 Seiten
    ISBN: 978-3-89336-535-7

15. **RED-IMPACT**
    **Impact of Partitioning, Transmutation and Waste Reduction Technologies on the Final Nuclear Waste Disposal**
    **SYNTHESIS REPORT**
    ed. by W. von Lensa, R. Nabbi, M. Rossbach (2008), 178 pages
    ISBN 978-3-89336-538-8

16. **Ferritic Steel Interconnectors and their Interactions with Ni Base Anodes in Solid Oxide Fuel Cells (SOFC)**
    by J. H. Froitzheim (2008), 169 pages
    ISBN: 978-3-89336-540-1

17. **Integrated Modelling of Nutrients in Selected River Basins of Turkey**
    Results of a bilateral German-Turkish Research Project
    project coord. M. Karpuzcu, F. Wendland (2008), XVI, 183 pages
    ISBN: 978-3-89336-541-8

18. **Isotopengeochemische Studien zur klimatischen Ausprägung der Jüngeren Dryas in terrestrischen Archiven Eurasiens**
    von J. Parplies (2008), XI, 155 Seiten, Anh.
    ISBN: 978-3-89336-542-5

19. **Untersuchungen zur Klimavariabilität auf dem Tibetischen Plateau - Ein Beitrag auf der Basis stabiler Kohlenstoff- und Sauerstoffisotope in Jahrringen von Bäumen waldgrenznaher Standorte**
    von J. Griessinger (2008), XIII, 172 Seiten
    ISBN: 978-3-89336-544-9

20. **Neutron-Irradiation + Helium Hardening & Embrittlement Modeling of 9%Cr-Steels in an Engineering Perspective (HELENA)**
by R. Chaouadi (2008), VIII, 139 pages
ISBN: 978-3-89336-545-6

21. **in Bearbeitung**

22. **Verbundvorhaben APAWAGS (AOEV und Wassergenerierung) – Teilprojekt: Brennstoffreformierung – Schlussbericht**
von R. Peters, R. C. Samsun, J. Pasel, Z. Porš, D. Stolten (2008), VI, 106 Seiten
ISBN: 978-3-89336-547-0

23. **FREEVAL**
Evaluation of a Fire Radiative Power Product derived from Meteosat 8/9 and Identification of Operational User Needs
Final Report
project coord. M. Schultz, M. Wooster (2008), 139 pages
ISBN: 978-3-89336-549-4

24. **Untersuchungen zum Alkaliverhalten unter Oxycoal-Bedingungen**
von C. Weber (2008), VII, 143, XII Seiten
ISBN: 978-3-89336-551-7

25. **Grundlegende Untersuchungen zur Freisetzung von Spurstoffen, Heißgaschemie, Korrosionsbeständigkeit keramischer Werkstoffe und Alkalirückhaltung in der Druckkohlenstaubfeuerung**
von M. Müller (2008), 207 Seiten
ISBN: 978-3-89336-552-4

26. **Analytik von ozoninduzierten phenolischen Sekundärmetaboliten in *Nicotiana tabacum* L. cv Bel W3 mittels LC-MS**
von I. Koch (2008), III, V, 153 Seiten
ISBN 978-3-89336-553-1

27. **IEF-3 Report 2009. Grundlagenforschung für die Anwendung**
(2009), ca. 230 Seiten
ISBN: 978-3-89336-554-8

28. **Influence of Composition and Processing in the Oxidation Behavior of MCrAlY-Coatings for TBC Applications**
by J. Toscano (2009), 168 pages
ISBN: 978-3-89336-556-2

29. **Modellgestützte Analyse signifikanter Phosphorbelastungen in hessischen Oberflächengewässern aus diffusen und punktuellen Quellen**
von B. Tetzlaff (2009), 149 Seiten
ISBN: 978-3-89336-557-9

30. **Nickelreaktivlot / Oxidkeramik – Fügungen als elektrisch isolierende Dichtungskonzepte für Hochtemperatur-Brennstoffzellen-Stacks**
von S. Zügner (2009), 136 Seiten
ISBN: 978-3-89336-558-6

31. **Langzeitbeobachtung der Dosisbelastung der Bevölkerung in radioaktiv kontaminierten Gebieten Weißrusslands – Korma-Studie**
von H. Dederichs, J. Pillath, B. Heuel-Fabianek, P. Hill, R. Lennartz (2009), Getr. Pag.
ISBN: 978-3-89336-532-3

32. **Herstellung von Hochtemperatur-Brennstoffzellen über physikalische Gasphasenabscheidung**
von N. Jordán Escalona (2009), 148 Seiten
ISBN: 978-3-89336-532-3

33. **Real-time Digital Control of Plasma Position and Shape on the TEXTOR Tokamak**
by M. Mitri (2009), IV, 128 pages
ISBN: 978-3-89336-567-8

34. **Freisetzung und Einbindung von Alkalimetallverbindungen in kohlebefeuerten Kombikraftwerken**
von M. Müller (2009), 155 Seiten
ISBN: 978-3-89336-568-5

35. **Kosten von Brennstoffzellensystemen auf Massenbasis in Abhängigkeit von der Absatzmenge**
von J. Werhahn (2009), 242 Seiten
ISBN: 978-3-89336-569-2

36. **Einfluss von Reoxidationszyklen auf die Betriebsfestigkeit von anodengestützten Festoxid-Brennstoffzellen**
von M. Ettler (2009), 138 Seiten
ISBN: 978-3-89336-570-8

37. **Großflächige Plasmaabscheidung von mikrokristallinem Silizium für mikromorphe Dünnschichtsolarmodule**
von T. Kilper (2009), XVII, 154 Seiten
ISBN: 978-3-89336-572-2

38. **Generalized detailed balance theory of solar cells**
by T. Kirchartz (2009), IV, 198 pages
ISBN: 978-3-89336-573-9

39. **The Influence of the Dynamic Ergodic Divertor on the Radial Electric Field at the Tokamak TEXTOR**
von J. W. Coenen (2009), xii, 122, XXVI pages
ISBN: 978-3-89336-574-6

40. **Sicherheitstechnik im Wandel Nuklearer Systeme**
von K. Nünighoff (2009), viii, 215 Seiten
ISBN: 978-3-89336-578-4

41. **Pulvermetallurgie hochporöser NiTi-Legierungen für Implanat- und Dämpfungsanwendungen**
von M. Köhl (2009), XVII, 199 Seiten
ISBN: 978-3-89336-580-7

42. **Einfluss der Bondcoatzusammensetzung und Herstellungsparameter auf die Lebensdauer von Wärmedämmschichten bei zyklischer Temperaturbelastung**
von M. Subanovic (2009), 188, VI Seiten
ISBN: 978-3-89336-582-1

43. **Oxygen Permeation and Thermo-Chemical Stability of Oxygen Permeation Membrane Materials for the Oxyfuel Process**
by A. J. Ellett (2009), 176 pages
ISBN: 978-3-89336-581-4

44. **Korrosion von polykristallinem Aluminiumoxid (PCA) durch Metalljodidschmelzen sowie deren Benetzungseigenschaften**
von S. C. Fischer (2009), 148 Seiten
ISBN: 978-3-89336-584-5

45. **IEF-3 Report 2009. Basic Research for Applications**
(2009), 217 Seiten
ISBN: 978-3-89336-585-2

46. **Verbundvorhaben ELBASYS (Elektrische Basissysteme in einem CFK-Rumpf) - Teilprojekt: Brennstoffzellenabgase zur Tankinertisierung - Schlussbericht**
von R. Peters, J. Latz, J. Pasel, R. C. Samsun, D. Stolten
(2009), xi, 202 Seiten
ISBN: 978-3-89336-587-6

47. **Aging of $^{14}$C-labeled Atrazine Residues in Soil: Location, Characterization and Biological Accessibility**
by N. D. Jablonowski (2009), IX, 104 pages
ISBN: 978-3-89336-588-3

48. **Entwicklung eines energetischen Sanierungsmodells für den europäischen Wohngebäudesektor unter dem Aspekt der Erstellung von Szenarien für Energie- und $CO_2$ - Einsparpotenziale bis 2030**
von P. Hansen (2009), XXII, 281 Seiten
ISBN: 978-3-89336-590-6

49. **Reduktion der Chromfreisetzung aus metallischen Interkonnektoren für Hochtemperaturbrennstofzellen durch Schutzschichtsysteme**
von R. Trebbels (2009), iii, 135 Seiten
ISBN: 978-3-89336-591-3

50. **Bruchmechanische Untersuchung von Metall / Keramik-Verbundsystemen für die Anwendung in der Hochtemperaturbrennstoffzelle**
von B. Kuhn (2009), 118 Seiten
ISBN: 978-3-89336-592-0

51. **Wasserstoff-Emissionen und ihre Auswirkungen auf den arktischen Ozonverlust**
**Risikoanalyse einer globalen Wasserstoffwirtschaft**
von T. Feck (2009), 180 Seiten
ISBN: 978-3-89336-593-7

52. **Development of a new Online Method for Compound Specific Measurements of Organic Aerosols**
by T. Hohaus (2009), 156 pages
ISBN: 978-3-89336-596-8

53. **Entwicklung einer FPGA basierten Ansteuerungselektronik für Justageeinheiten im Michelson Interferometer**
von H. Nöldgen (2009), 121 Seiten
ISBN: 978-3-89336-599-9

54. **Observation – and model – based study of the extratropical UT/LS**
by A. Kunz (2010), xii, 120, xii pages
ISBN: 978-3-89336-603-3

55. **Herstellung polykristalliner Szintillatoren für die Positronen-Emissions-Tomographie (PET)**
von S. K. Karim (2010), VIII, 154 Seiten
ISBN: 978-3-89336-610-1

56. **Kombination eines Gebäudekondensators mit H2-Rekombinatorelementen in Leichwasserreaktoren**
von S. Kelm (2010), vii, 119 Seiten
ISBN: 978-3-89336-611-8

57. **Plant Leaf Motion Estimation Using A 5D Affine Optical Flow Model**
by T. Schuchert (2010), X, 143 pages
ISBN: 978-3-89336-613-2

58. **Tracer-tracer relations as a tool for research on polar ozone loss**
by R. Müller (2010), 116 pages
ISBN: 978-3-89336-614-9

59. **Sorption of polycyclic aromatic hydrocarbon (PAH) to Yangtze River sediments and their components**
by J. Zhang (2010), X, 109 pages
ISBN: 978-3-89336-616-3

60. **Weltweite Innovationen bei der Entwicklung von CCS-Technologien und Möglichkeiten der Nutzung und des Recyclings von $CO_2$**
Studie im Auftrag des BMWi
von W. Kuckshinrichs et al. (2010), X, 139 Seiten
ISBN: 978-3-89336-617-0

61. **Herstellung und Charakterisierung von sauerstoffionenleitenden Dünnschichtmembranstrukturen**
von M. Betz (2010), XII, 112 Seiten
ISBN: 978-3-89336-618-7

62. **Politikszenarien für den Klimaschutz V – auf dem Weg zum Strukturwandel, Treibhausgas-Emissionsszenarien bis zum Jahr 2030**
hrsg. von P. Hansen, F. Chr. Matthes (2010), 276 Seiten
ISBN: 978-3-89336-619-4

63. **Charakterisierung Biogener Sekundärer Organischer Aerosole mit Statistischen Methoden**
von C. Spindler (2010), iv, 163 Seiten
ISBN: 978-3-89336-622-4

64. **Stabile Algorithmen für die Magnetotomographie an Brennstoffzellen**
von M. Wannert (2010), ix, 119 Seiten
ISBN: 978-3-89336-623-1

65. **Sauerstofftransport und Degradationsverhalten von Hochtemperatur-membranen für CO2-freie Kraftwerke**
von D. Schlehuber (2010), VII, 139 Seiten
ISBN: 978-3-89336-630-9

66. **Entwicklung und Herstellung von foliengegossenen, anodengestützten Festoxidbrennstoffzellen**
von W. Schafbauer (2010), VI, 164 Seiten
ISBN: 978-3-89336-631-6

67. **Disposal strategy of proton irradiated mercury from high power spallation sources**
by S. Chiriki (2010), xiv, 124 pages
ISBN: 978-3-89336-632-3

68. **Oxides with polyatomic anions considered as new electrolyte materials for solid oxide fuel cells (SOFCs)**
by O. H. Bin Hassan (2010), vii, 121 pages
ISBN: 978-3-89336-633-0

69. **Von der Komponente zum Stack: Entwicklung und Auslegung von HT-PEFC-Stacks der 5 kW-Klasse**
von A. Bendzulla (2010), IX, 203 Seiten
ISBN: 978-3-89336-634-7

70. **Satellitengestützte Schwerewellenmessungen in der Atmosphäre und Perspektiven einer zukünftigen ESA Mission (PREMIER)**
von S. Höfer (2010), 81 Seiten
ISBN: 978-3-89336-637-8

71. **Untersuchungen der Verhältnisse stabiler Kohlenstoffisotope in atmosphärisch relevanten VOC in Simulations- und Feldexperimenten**
von H. Spahn (2010), IV, 210 Seiten
ISBN: 978-3-89336-638-5

72. **Entwicklung und Charakterisierung eines metallischen Substrats für nanostrukturierte keramische Gastrennmembranen**
von K. Brands (2010), vii, 137 Seiten
ISBN: 978-3-89336-640-8

73. **Hybridisierung und Regelung eines mobilen Direktmethanol-Brennstoff-zellen-Systems**
von J. Chr. Wilhelm (2010), 220 Seiten
ISBN: 978-3-89336-642-2

74. **Charakterisierung perowskitischer Hochtemperaturmembranen zur Sauerstoffbereitstellung für fossil gefeuerte Kraftwerksprozesse**
von S.A. Möbius (2010) III, 208 Seiten
ISBN: 978-3-89336-643-9

75. **Characterization of natural porous media by NMR and MRI techniques: High and low magnetic field studies for estimation of hydraulic properties**
by L.-R. Stingaciu (2010), 96 pages
ISBN: 978-3-89336-645-3

76. **Hydrological Characterization of a Forest Soil Using Electrical Resistivity Tomography**
by Chr. Oberdörster (2010), XXI, 151 pages
ISBN: 978-3-89336-647-7

77. **Ableitung von atomarem Sauerstoff und Wasserstoff aus Satellitendaten und deren Abhängigkeit vom solaren Zyklus**
von C. Lehmann (2010), 127 Seiten
ISBN: 978-3-89336-649-1

78. **in Bearbeitung**

79. **Ultrafast voltex core dynamics investigated by finite-element micromagnetic simulations**
by S. Gliga (2010), vi, 144 pages
ISBN: 978-3-89336-660-6

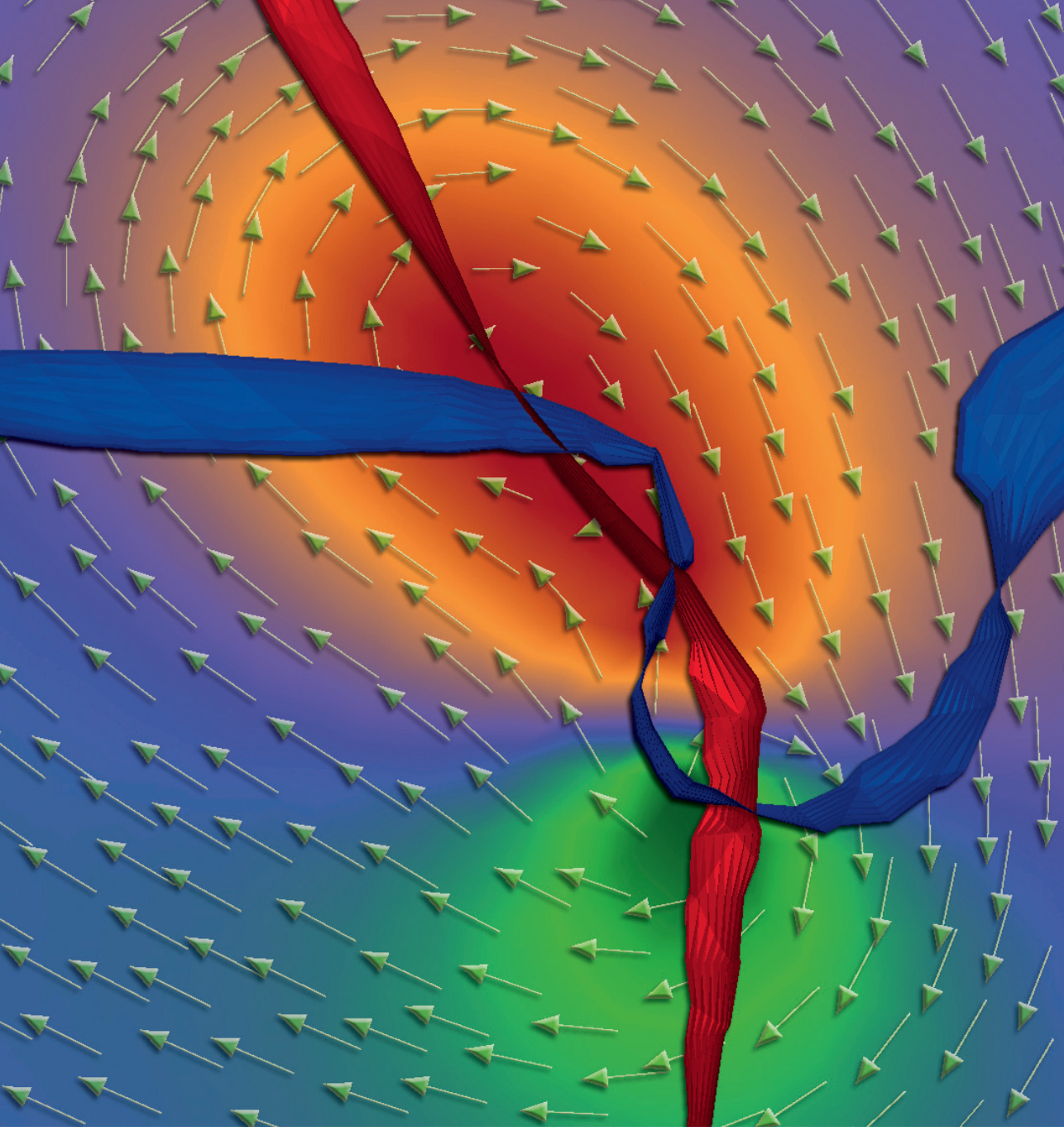

Energie & Umwelt / Energy & Environment
Band / Volume 79
ISBN 978-3-89336-660-6

JÜLICH
FORSCHUNGSZENTRUM